

Czech Technical University in Prague
Faculty of Nuclear Sciences and Physical Engineering

Diffraction in the ATLAS Experiment

Doctoral thesis

Prague, 2012

Ing. Pavel Růžička

Author: Ing. Pavel Růžička
Department: Department of Physics
Supervisors: prom. fyz. Václav Vrba, CSc.
e-mail address: vrba@fzu.cz
key words: particle diffraction, two-photon exchange, exclusive production, rapidity gaps, QCD, forward physics, Monte Carlo, hadronisation

Abstract:

This thesis is devoted to diffraction physics at Large Hadron Collider (LHC). The experimental part of the work studies rapidity gap production in the first data sample of integrated luminosity of $7.1 \pm 0.2 \mu\text{b}^{-1}$ recorded by the ATLAS experiment at $\sqrt{s} = 7 \text{ TeV}$. The rapidity gaps, defined as regions in rapidity devoid of particle activity, were reconstructed based on both energy deposits in ATLAS calorimeter system and tracks reconstructed in Inner Detector.

Floating rapidity gaps measured as the largest pseudorapidity gap within the detector acceptance, $\eta = \pm 4.9$, were used for determination of diffractive fractions in the total inelastic cross sections. Moreover, inclusive forward rapidity gap spectrum $\Delta\eta^F$ was measured. Forward rapidity, $\Delta\eta^F$, is defined as the largest pseudorapidity gap in event which spans from the limit of the detector acceptance to the first detected particle. The forward rapidity gap distribution was estimated for different cuts on final particle momenta 200, 400, 600, and 800 MeV. The obtained distributions were used to constrain Monte Carlo models. Especially, measurement of large $\Delta\eta^F$ production reduce theoretical uncertainties in diffractive models while events with small $\Delta\eta^F$ allow to test hadronisation and underlying event models.

In addition, models for hard diffraction and exclusive processes were implemented into HERWIG++ Monte Carlo generator as a part of this work. These processes can be measured using proton taggers or rapidity gap method at LHC. Their measurement improve our understanding of diffractive production of large masses but it can be also used for precise measurement of new phenomena.

Contents

1	Introduction	1
2	Standard Model of Particle Physics	4
3	Quantum Chromodynamics	6
3.1	Asymptotic Freedom and Confinement	7
3.2	Parton Distribution Functions and Evolution Equations	8
4	Diffraction	13
4.1	Regge Theory	14
4.2	Soft Diffraction Phenomenology	18
4.3	Hard Diffraction Phenomenology	21
4.4	Central Exclusive Production in QCD	25
4.5	Photon Initiated Processes	27
5	Large Hadron Collider and ATLAS Experiment	29
5.1	Large Hadron Collider	29
5.2	ATLAS Detector	31
5.2.1	Inner Detector	33
5.2.2	Calorimeter	34
5.2.3	Minimum Bias Trigger Scintillator	37
5.2.4	LUCID	37
5.2.5	Zero Degree Calorimeter	39
5.3	ATLAS Trigger	39
6	Monte Carlo Event Generators	40
6.1	Monte Carlo Integration	41
6.2	Event Generation	43
6.3	Parton Showers	44
6.4	Hadronisation Models	46

6.4.1	Independent Fragmentation	46
6.4.2	String Hadronisation	47
6.4.3	Cluster Hadronisation	49
6.5	Underlying Events and Minimum Bias Simulation	50
6.6	Modeling of Inclusive Diffraction in MC Generators	53
7	Forward Processes in Herwig++	56
7.1	Photon Initiated Processes	57
7.2	Hard Diffractive Processes	58
7.3	QCD Exclusive Processes	61
7.3.1	Durham Model in Herwig++	61
7.3.2	SM Higgs Production	66
7.3.3	Di-Jet Production	67
7.3.4	Di-Photon Production	68
7.4	Summary	69
8	Experimental Definition of Rapidity Gaps	71
8.1	Rapidity Gaps in the Calorimeter	72
8.1.1	MC Simulation of Cell Noise	73
8.1.2	Calorimeter Noise Separation	75
8.2	Lowest Energy Detection Limit	77
8.3	Adding Inner Detector Information	80
8.4	Summary of the Gap Finding Algorithms	82
9	Description of Minimum Bias Data in MC Generators	84
9.1	Cluster and Track Distributions	84
9.2	Forward Energy Flow	85
9.3	Summary	86
10	Diffractive Fractions in Total Inelastic Cross Section	90
10.1	Event Selection	91
10.2	Estimation of Beam Induced Background	92
10.3	Reorganization of MC Templates	93
10.4	Fit Procedure	95
10.5	Fit Results	98
10.6	Summary	99
11	Forward Rapidity Gap Production	101
11.1	Data Selection and Detector Distribution	102

11.2	Corrections for Experimental Effects	102
11.3	Systematic Uncertainties	107
11.3.1	Energy Scale Uncertainty	107
11.3.2	Additional Material Uncertainty	107
11.3.3	MBTS Efficiency	108
11.3.4	Tracking Uncertainty	108
11.3.5	MC Unfolding Uncertainty	108
11.3.6	Diffraction Mix Uncertainty	108
11.3.7	Central Diffraction Uncertainty	109
11.3.8	Luminosity Uncertainty	109
11.3.9	Summary of Systematic Uncertainties	110
11.4	Differential Cross Section for Forward Rapidity Gaps	110
11.4.1	Differential Cross Section for $p_T^{\text{cut}} = 200 \text{ MeV}$	110
11.4.2	Estimation of Pomeron Intercept	113
11.4.3	Higher Transverse Momentum Cuts	115
11.4.4	Inelastic Distribution in Herwig++	115
11.5	Summary	117
12	Summary	119

Chapter 1

Introduction

Typical inelastic proton-proton collision with center-of-mass energy of 7 TeV at Large Hadron Collider (LHC) produces around six charged particles with transverse momentum $p_T > 100$ MeV per pseudorapidity unit in the central region [1]. Corresponding average distance between two neighbouring particles is 0.15 units of pseudorapidity. However, significant fraction of inelastic events exhibits much larger gaps between particles. These regions in rapidity devoid of particle activity are referred as rapidity gaps and the related quasi-elastic events are termed as diffractive. Diffractive processes occur in approximately 30% of the collisions at LHC at $\sqrt{s} = 7$ TeV. Their large rapidity gap production is attributed to exchange of states with vacuum quantum numbers. Creation of small rapidity gaps is possible also in non-diffractive events due to fluctuations in hadronisation. However, it is exponentially suppressed with increasing gap size.

The average interaction has small momentum transfer (small mass final state) and perturbative Quantum Chromodynamics is not applicable. Instead, phenomenological models are employed. The models contain large theoretical uncertainties and experimental data are required for their constrain. Owing to large contribution into the inelastic cross section, an improvement in understanding of diffractive processes is desirable in its own right. Moreover, diffractive dissociation is closely related to the elastic scattering and the total cross section. It is important for description of cosmic ray particles interacting with the atmosphere [2]. In addition, precise measurements at LHC require good modeling of additional proton-proton interactions (pile-up) as well as underlying events description where diffractive dissociation has to be taken into account. Diffraction is also responsible for the significant contribution to uncertainty in the luminosity monitoring.

This thesis studies production of the rapidity gaps at LHC at $\sqrt{s} = 7$ TeV. Diffractive models are constrained by measurement of large rapidity gaps while measurement of small gaps test hadronisation and underlying event description in current Monte Carlo (MC) generators. Furthermore, contribution of diffractive components into the total inelastic cross section is estimated using different rapidity gap patterns of the corresponding processes.

Surprisingly large fraction of events is accompanied by large rapidity gaps even in hard production with high momentum transfer (high mass final state). Experiments at lepton-hadron colliders observed their contribution to be around 5-10%. Models describing these processes at electron-proton experiments are quite well constrained. However, the transition of these models to description of hadron-hadron interactions requires introduction of a new uncertainty related to additional soft parton scatterings which can spoil the rapidity gap. Thus the hard diffractive contribution measured at the Tevatron was smaller around 1%. The processes containing large rapidity gaps are even more interesting if the particular final state such as di-jet, W^+W^- , or Higgs boson is produced exclusively i.e. it is accompanied only by two intact beam protons. These processes are induced either by a strong interaction (exchange of colour singlet gluon pairs) or by an electroweak interaction (two photon collider). Such clear environment provides possibility for precise measurements of new states even at the hadron-hadron collisions. Some of the processes which are especially interesting for measurement at LHC have been implemented to a new MC generator HERWIG++ as a part of this work. The collection of the forward physics models into HERWIG++ was motivated by the fact that these processes are spread among many MC generators where some of them starts to be obsolete or they are not further tuned to data.

The first half of the thesis provides a basic theoretical and experimental apparatus needed for the work. Brief overview of the Standard Model and Quantum Chromodynamics is given in Chapters 2 and 3. The next chapter reviews the current theoretical and experimental status of diffractive and exclusive processes. In the following chapter, experimental apparatus of LHC and ATLAS detector is described. It concentrates on those parts of the detector which were used for the rapidity gap measurements. Chapter 6 is devoted to basic MC event generation techniques. The methods for the MC integration were necessary tools for implementation of the forward physics processes into HERWIG++. They are introduced in the first two sections. The remaining part of the chapter gives quick overview of perturbative and non-perturbative particle production and underlying event models. These topics have close connection to the rapidity gap production.

The result part of this work starts in Chapter 7 by providing detailed description of models implemented in HERWIG++. Particularly, hard diffraction, central exclusive production in QCD, and two photon initiated processes are reviewed and compared with different MC generators in individual sections.

In the remaining chapters, the experimental results of rapidity gap production are discussed. At first, the algorithm for rapidity gap reconstruction using the ATLAS calorimeter system in combination of Inner Detector is introduced.

The algorithm is used for estimation of diffractive fractions in the total inelastic cross section in Chapter 10. In addition to the previous ATLAS measurement using Minimum Bias Trigger Scintillator [3], the novel algorithm can separate different diffractive topologies and reduce MC

model systematic uncertainty due to larger pseudorapidity coverage provided by the ATLAS calorimeter system and Inner Detector.

Measurement of the differential inelastic cross section as a function of rapidity gap size is presented in Chapter 11. The measurement is done for different cuts on the transverse momenta of final particles and results are compared with various MC models in order to give constraints on some of their parameters.

Chapter 2

Standard Model of Particle Physics

The Standard Model (SM) is currently the most successful theory in description of phenomena in Particle Physics. It is Quantum Field Theory based on non-Abelian gauge symmetry $SU(2)_L \times U(1)_Y \times SU(3)_C$, where subscript L denotes coupling of left-handed fields, Y is hypercharge and C is color charge.

Such symmetry requires 12 bosons fields carrying integer spin 1 which mediate electromagnetic, weak, and strong interaction between the fermions matter fields. Fermions, with half integer spin 1/2, are divided into three families where each family consists of two leptons and two quarks. Charged leptons e , μ and τ , having all the same electric charge, are accompanied by corresponding electrically neutral neutrino ν_e , ν_μ , ν_τ which are considered to be massless in SM and interact only via weak interaction. The quark fields have non-zero quantum number colour and thus can interact, apart from electromagnetic and weak interaction, also via strong interaction. Each family includes one quark with positive fractional electric charge $2/3$ (u, c, t) and one quark with negative fractional charge $-1/3$ (d, s, b). The fermion fields and their properties in SM are summarized Table 2.1.

A boson which is responsible for electromagnetic interaction is photon, γ , and couples to the matter fields which carry the electric charge. The weak interaction is transmitted by two charged bosons W^\pm and one neutral boson Z^0 which was one of the great prediction of the Standard Model. The bosons mediating weak interaction couples to weak hypercharge which is different for left-handed and right-handed components of the fermion fields. This enables to describe the well known parity violation effects in SM. The weak interaction is a short range force and thus the mediating bosons have to be heavy. A mechanism allowing particles to acquire mass is Higgs mechanism in which the symmetry of electroweak sector $SU(2)_L \times U(1)_Y$ is spontaneously broken to $U(1)_Q$, where subscript Q denotes electric charge. This gives a rise to new scalar particle called Higgs boson, H , which is the only missing part of the SM that needs to be experimentally confirmed. A detailed description of the electroweak sector in the SM can be found in [4].

The strong interaction between quarks, existing in three colour states, is mediated by eight gluons. The force increases with growing distance between quarks and therefore quarks are confined in form of hadronic states during normal condition. However, at very small distances the confined quarks behave as almost free particles. This property is known as asymptotic freedom. The theory of strong interaction is called Quantum Chromodynamics and since it has close connection with high energy diffraction it is discussed in more detail in the following chapter.

	First family	Second family	Third family	Electric charge (e)	Weak hypercharge	Carry colour?
leptons	electron (e)	muon (μ)	tau (τ)	-1	$Y_L = -1/2$ $Y_R = 1$	no
	electron-neutrino (ν_e)	muon-neutrino (ν_μ)	tau-neutrino (ν_τ)	0	$Y_L = -1/2$ $Y_R = 0$	no
quarks	up (u)	charm (c)	top (t)	2/3	$Y_L = -1/6,$ $Y_R = 2/3$	yes
	down (d)	strange (s)	bottom (b)	-1/3	$Y_L = 1/6,$ $Y_R = -1/3$	yes

Table 2.1: Summary of elementary fermion fields in SM and their properties. The Y_R and Y_L denote weak hypercharge for right-handed and left-handed components of fermion fields respectively.

Chapter 3

Quantum Chromodynamics

Quantum Chromodynamics (QCD) is a theory of strong interactions described by the Lagrangian which is invariant under a local gauge transformation $SU(3)$ i.e. it is invariant under a local space-time transformation acting on the quark colour triplet $\Phi(x)$

$$\Phi'(x) = S(x)\Phi(x), \quad (3.1)$$

where $S(x)$ is a unitary matrix with $\det S(x) = 1$. Since the vector space of such matrices forms representation of Lie group $S(x)$ can be written in an exponential form

$$S(x) = \exp(i\omega^a(x)T^a), \quad (3.2)$$

where T^a are generators of the $SU(3)$ (usual choice are Gell-Mann matrices) and satisfy commutation relations of the corresponding Lie algebra

$$[T^a, T^b] = if^{abc}T^c, \quad (3.3)$$

where symbol f^{abc} is a fully antisymmetric tensor called structure constant of $SU(3)$ [5]. The symmetry of the Lagrangian implies existence of 8 gauged boson massless fields, A^A , with spin 1 called gluons mediating strong interaction between quarks, q_a . The QCD Lagrangian reads

$$\mathcal{L} = -\frac{1}{4}F_{\alpha\beta}^A F^{A\alpha\beta} + \sum_{\text{flavours}} \bar{q}_a(i\not{D} - m)_{a,b}q_b, \quad (3.4)$$

where A runs over 8 colour degrees of freedom, a, b runs over 3 quark colours and m is mass of the quark field. The first gauged term of the Lagrangian contains a contraction of two field strength tensors

$$F_{\alpha\beta}^A = \partial_\alpha A_\beta^A - \partial_\beta A_\alpha^A - gf^{ABC}A_\alpha^B A_\beta^C. \quad (3.5)$$

The presence of the third non-Abelian term is responsible for self-interactions of three and four gluons. These interactions are not available in QED and they make a crucial difference in behavior of higher order perturbative contributions between QED and QCD as will be seen in

the following section. The second term in the Lagrangian (3.4) contains covariant derivatives invented in analogy with the minimal substitution in QED in order to ensure the local gauge invariance of the QCD Lagrangian

$$(\mathcal{D}_\alpha)_{a,b} = \partial_\alpha \delta_{a,b} - ig(A_\alpha^A T^A)_{a,b}. \quad (3.6)$$

Since gluons are massless, the same problem as in QED arise when one gets to definition of a gluon propagator. The definition is only possible if a particular gauge is chosen. One example of gauge fixing terms is the covariant gauge [6] with parameter λ

$$\mathcal{L}_{\text{gf}} = -\frac{1}{2\lambda}(\partial_\alpha A^\alpha)^2 \quad (3.7)$$

which needs to be added to the Lagrangian (3.4). This covariant fixing term must be further supplemented by Lagrangian with Faddeev-Popov ghosts scalar fields

$$\mathcal{L}_{\text{ghost}} = \partial_\alpha \eta^{A\dagger} (D_{AB}^\alpha \eta^B). \quad (3.8)$$

The ghost fields cancel unphysical degrees of freedom which would otherwise propagate to physically measurable quantities [6].

3.1 Asymptotic Freedom and Confinement

Leading order computations in perturbative QCD are straightforward. The real difference from Abelian QED appears when higher order contributions in $\alpha_S = \frac{g}{4\pi}$ are included. A computation of the higher orders requires an addition of virtual corrections. These corrections are evaluated using loop integrals which contain ultraviolet divergences (UV) similarly as in QED. This problem has been resolved by a procedure called renormalization. In the first step of this procedure, the UV divergent integrals are regularized by some sort of cut-off. Arbitrary scale μ is introduced in order to separate finite and divergent parts of the integral. The infinities are finally removed by redefinition of couplant, masses, quark and gluon wave functions, and ghost fields. A new renormalized Lagrangian is constructed from the bare Lagrangian (3.4) supplemented by a counterterm Lagrangian, canceling the divergences generated by the original Lagrangian.

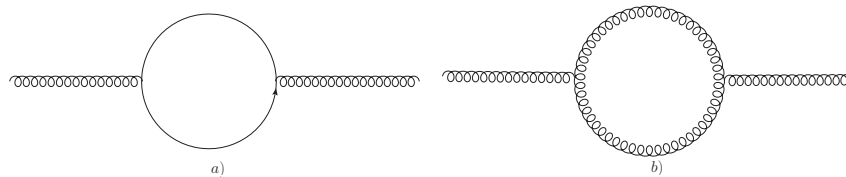


Figure 3.1: Feynman diagrams contributing to the QCD β function in one loop approximation. The diagram b) is responsible for asymptotic freedom in QCD.

The renormalization procedure features a large freedom of selecting finite parts of counterterms (called renormalization scheme) and of choosing the renormalization scale μ . However, physical quantities cannot depend on any of these arbitrary choices. This statement is contained in renormalization group equation which determines the running coupling and running masses [7]. The evolution equation for strong coupling constant in a mass independent scheme reads

$$\frac{\partial \alpha_S}{\partial \ln \mu} = \beta(\alpha_S(\mu)) = -b\alpha_S^2(1 + b'\alpha_S + \mathcal{O}(\alpha_S^2)), \quad (3.9)$$

where the right hand side of the equation is called β -function of QCD. Its first two coefficients are uniquely determined

$$b = \frac{(11C_A - 2n_f)}{12\pi} \quad (3.10)$$

$$b' = \frac{(17C_A^2 - 5C_An_f - 3C_Fn_f)}{2\pi(11C_A - 2n_f)}, \quad (3.11)$$

where C_A and C_F are colour factors of adjoint and fundamental representation respectively. They are defined as eigenvalues of Casimir operator in corresponding representation and take values in the specific case of $SU(3)$ $C_F = 4/3$ and $C_A = 3$. n_f is the number of active quark flavours i.e. those with mass smaller than the typical scale of a process. Higher order coefficients are arbitrary and depend on the renormalization scheme. The fact that b is positive and thus has opposite sign as in QED has crucial consequences. It implies that $\alpha_S(\mu/\Lambda_{\text{QCD}}) \rightarrow 0$ as $\mu \rightarrow \infty$, where Λ_{QCD} is fundamental scale parameter with dimension of energy. This can be explicitly seen from leading order solution of (3.9) which reads

$$\alpha_S(\mu/\Lambda_{\text{QCD}}) = \frac{1}{b \ln(\mu/\Lambda_{\text{QCD}})}. \quad (3.12)$$

The behavior of the coupling constant is called asymptotic freedom and it is a consequence of the non-Abelian term in (3.5) which introduces additional contributions from gluon self interaction in quark and gluon self energies. The graphs contributing to the QCD β function at one loop approximation can be seen in Figure 3.1.

On the other hand, the coupling constant is very large at small scales (at large distances) and grows to infinity as μ is approaching the parameter Λ_{QCD} . This says that perturbative QCD is not trustable in regime close to $\Lambda_{\text{QCD}} \approx 200$ MeV, a value corresponding approximately to an inverse size of the hadrons. Such growth of the coupling with decreasing scale is called confinement.

3.2 Parton Distribution Functions and Evolution Equations

Proton structure is traditionally probed at lepton-proton colliders in reactions

$$l(k) + \text{proton}(p) \rightarrow l'(k') + X; l, l' = e, \mu, \nu_e, \nu_\mu, \quad (3.13)$$

where k, k' are four-momenta of incoming and outgoing lepton, p is the proton four-momentum and X denotes any final state allowed by conservation laws. The reactions (3.13), depicted in Figure 3.2, are usually described by the following set of kinematical variables

$$s = (k + P)^2 \quad (3.14)$$

$$Q^2 = -q^2 = -(k - k')^2 \quad (3.15)$$

$$x = \frac{Q^2}{2pq} = \frac{Q^2}{W^2 + Q^2 - m_p^2} \quad (3.16)$$

$$y = \frac{pq}{pk} = \frac{W^2 + Q^2 - m_p^2}{s - m_p^2} \quad (3.17)$$

$$W^2 = (q + p)^2 = \frac{Q^2(1 - x)}{x} + m_p^2, \quad (3.18)$$

where m_p is proton mass. At low scales, where momentum transferred Q^2 is much smaller than proton mass, proton can be considered as a point like fermion with anomalous magnetic moment and the cross section can be computed in QED framework. However, when $Q^2 \gg m_p$ proton reveals to be object with internal structure composed of partons. Furthermore, at large Q^2 the probability of a proton to be broken and producing a hadronic system X rapidly increases. At such conditions the reactions (3.13) are called Deep Inelastic Scattering (DIS). The proton

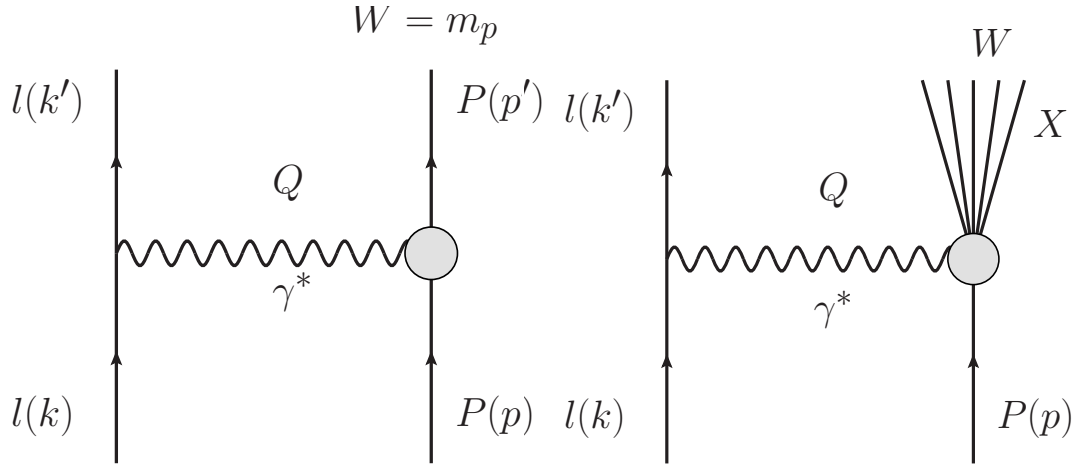


Figure 3.2: Feynman diagrams of elastic scattering (left) and inelastic scattering (right) of lepton on the proton.

partonic content is incorporated into the theory in form of parton distribution functions (PDF) $q_i(x, t)$, $g(x, t)$ describing the probability to find quark with flavour i or gluon with maximum virtuality t and carrying momentum fraction x of the proton. Because of the weak dependence of the PDF on the scale t it was originally believed that PDF are only function of variable x ¹.

However, the rise of the QCD came with explanation of the dependence on the scale t . In QCD, partons acquire virtuality by interactions with other partons inside the proton. This can

¹Momentum fraction x carried by parton is equal to Bjorken x defined by (3.16).

be seen from the cross section for emission of an extra gluon in $e^- + q \rightarrow e^- + q + g$ reaction having a form

$$\sigma^{(1)} \propto \alpha_S \left(P_{qq}^{(0)}(x) \ln \frac{M^2}{m_g^2} + f(x) \right), \quad (3.19)$$

where M denotes invariant mass of qg system and $P_{qq}^{(0)}(x)$ is quark splitting function giving the probability of quark splitting to gluon and a quark which carries momentum fraction x of the original quark. For further references, the exact form of the quark and gluon splitting functions in the first order of perturbation theory are given

$$P_{qq}^{(0)}(x) = P_{\bar{q}\bar{q}}^{(0)}(x) = C_F \left[\frac{1+x^2}{1-x} \right]_+, \quad (3.20)$$

$$P_{gq}^{(0)}(x) = P_{g\bar{q}}^{(0)}(x) = C_F \left[\frac{1+(1-x)^2}{x} \right], \quad (3.21)$$

$$P_{qg}^{(0)}(x) = P_{\bar{q}g}^{(0)}(x) = \frac{1}{2} [x^2 + (1-x)^2], \quad (3.22)$$

$$P_{gg}^{(0)}(x) = 2C_A \left[\frac{x}{(1-x)_+} + \frac{1-x}{x} + x(1-x) \right] + \delta(1-x) \frac{11C_A - 2n_f}{6}, \quad (3.23)$$

where '+' prescription' on the singular parts of the functions is defined as

$$\int_0^1 [f(x)]_+ g(x) dx \equiv \int_0^1 f(x) (g(x) - g(1)) dx. \quad (3.24)$$

The gluon mass m_g in (3.19) is introduced in order to regularize the infrared divergent integral of the form dM^2/M^2 . The function $f(x)$ is composed of terms $\ln 1/x$, $\ln x$. Therefore, $f(x)$ can be neglected in regimes where M^2 is large and x is not too small or too large. Then formula (3.19) can be generalized to n-partons emission in which the virtualities of emitting partons are strongly ordered

$$\sigma^{(n)} \propto \alpha_S^n \left[A_n \ln^n \frac{M^2}{m_g^2} + B_n \ln^{n-1} \frac{M^2}{m_g^2} + \mathcal{O} \left(\ln^{n-2} \frac{M^2}{m_g^2} \right) \right]. \quad (3.25)$$

The leading logarithms in series (3.25) can be effectively resummed by the so called evolution equations invented by Dokshitzer, Gribov, Lipatov, Altarelli, Parisi (DGLAP) which takes the form

$$\begin{aligned} \frac{\partial}{\partial \ln t} \begin{pmatrix} q_i(x, t) \\ g(x, t) \end{pmatrix} &= \frac{\alpha_S(t)}{2\pi} \sum_{q_j, \bar{q}_j} \int_x^1 \frac{dz}{z} \\ &\times \begin{pmatrix} P_{q_i q_j}(x/z, t) & P_{q_i g}(x/z, t) \\ P_{g q_j}(x/z, t) & P_{g g}(x/z, t) \end{pmatrix} \begin{pmatrix} q_j(z, t) \\ g(z, t) \end{pmatrix}. \end{aligned} \quad (3.26)$$

DGLAP equation describes an evolution of parton distribution functions $q_i(x, t)$, $g(x, t)$ with factorization scale t which has meaning of maximal virtuality of the parton entering into the hard process. The DGLAP evolution equations (3.26) needs to be supplemented by initial conditions

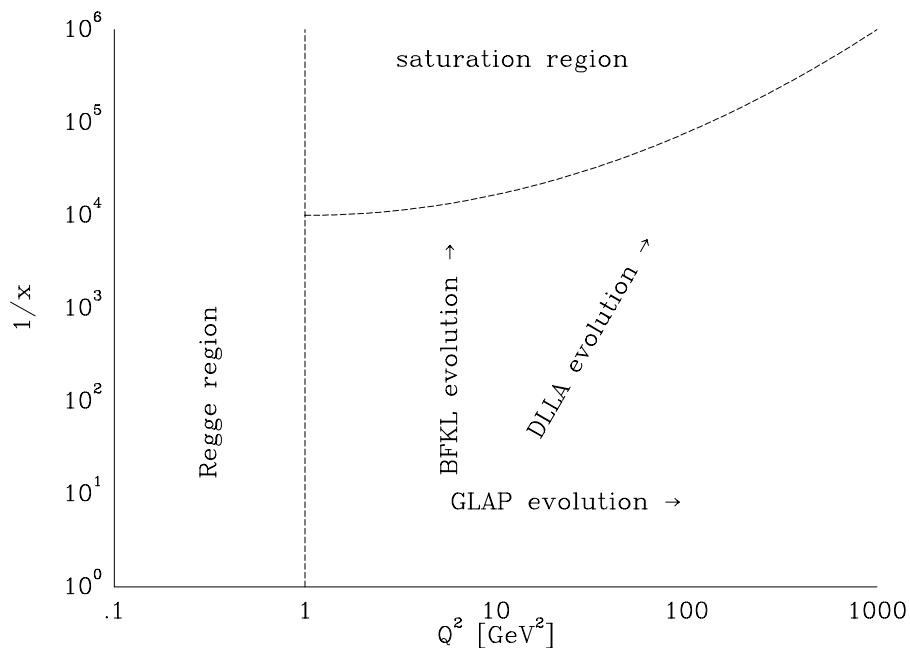


Figure 3.3: Validity of evolution equations in $1/x$ vs Q^2 plane. The plot is taken from ref. [6].

that cannot be determined from first principles and needs to be measured. This is done at lepton-hadron colliders but due to the PDFs universality they can be used also at hadron-hadron experiments. The total cross section is computed as a convolution of the PDFs with cross section of a hard process

$$\sigma = \sum_{i,j \in \text{flavour}} \int_0^1 dx_1 dx_2 f_i(x_1, t_1) f_j(x_2, t_2) \sigma^{\text{hard}}(s, x_1, x_2, t_1, t_2). \quad (3.27)$$

The usual choice of the factorization scale t is the momentum transfer in the hard process Q^2 (i.e. (3.15) for DIS processes) similarly as in case of the renormalization scale.

In the kinematic domain where x is small and Q^2 is large the double leading-log approximation can be used to resum the terms of the type $\alpha_s^n \ln^n Q^2 \ln^n 1/x$. This can be directly derived from DGLAP equation (3.26) using Mellin transformation and by keeping only the most singular $1/x$ terms in the splitting functions. The lowest order gluon distribution function is given by [7]

$$g(x, t) \sim \frac{1}{x} \exp \left[\frac{12}{\pi b} \ln \frac{\ln t/\Lambda_{\text{QCD}}^2}{\ln t_0/\Lambda_{\text{QCD}}^2} \ln \frac{1}{x} \right]^{\frac{1}{2}}, \quad (3.28)$$

where b is defined in (3.10). The solution (3.28) grows as x is decreasing. If the starting distribution is too steep at small- x then the above formula does not hold.

At small x and moderate $Q^2 > \Lambda_{\text{QCD}}^2$ where gluon contribution is dominant the leading logs

$\alpha_s^n \ln^n 1/x$ has to be resummed. This is done by the so called Balitsky, Fadin, Kuraev, Lipatov (BFKL) equation which describes the evolution of unintegrated gluon distribution function

$$xg(x, t) = \int^t \frac{dk_T^2}{k_T^2} G(k_T^2, t) \quad (3.29)$$

in x . At leading order the BFKL equation is given by

$$\frac{\partial G(x, k_T^2)}{\partial \ln(1/x)} = \frac{C_A \alpha_S}{\pi} k_T^2 \int_{k_0^2}^{\infty} \frac{dq_T^2}{q_T^2} \left[\frac{G(x, q_T^2) - G(x, k_T^2)}{|q_T^2 - k_T^2|} + \frac{G(x, k_T^2)}{\sqrt{4q_T^4 + k_T^4}} \right] \quad (3.30)$$

The regimes of validity for the mentioned evolution equation is schematically showed in Figure 3.3. There are currently attempts for combined description of both DGLAP and BFKL regions in one single equation. One of them is given by Ciafaloni, Catani, Fiorani, Marchesini (CCFM) equation which uses angular ordering to described both the x and Q^2 evolution with DGLAP and BFKL equation emerging as limiting cases [8, 9].

There is a rapid rise of gluon distribution function at very small- x predicted by both DGLAP and BFKL equations which eventually breaks down the parton model picture of scattering of independent partons. In this so called saturation regime it becomes possible that two partons overlap in space and the DGLAP and BFKL need to be modified for parton recombination [7]. This is still under study and more experimental data at very small- x regime are needed.

Chapter 4

Diffraction

Total hadron-hadron cross section can be divided into elastic processes where both protons are only rescattered without energy loss and inelastic processes in which protons are usually broken and extra particles are produced. The inelastic processes are usually further categorized into diffractive and non-diffractive contribution.

The diffractive events can be considered quasi-elastic. Their experimental signature are regions in rapidity devoid of particle production. These regions are called rapidity gaps. Three different topologies with the largest cross sections of diffractive processes, shown in Figure 4.1, are usually distinguished:

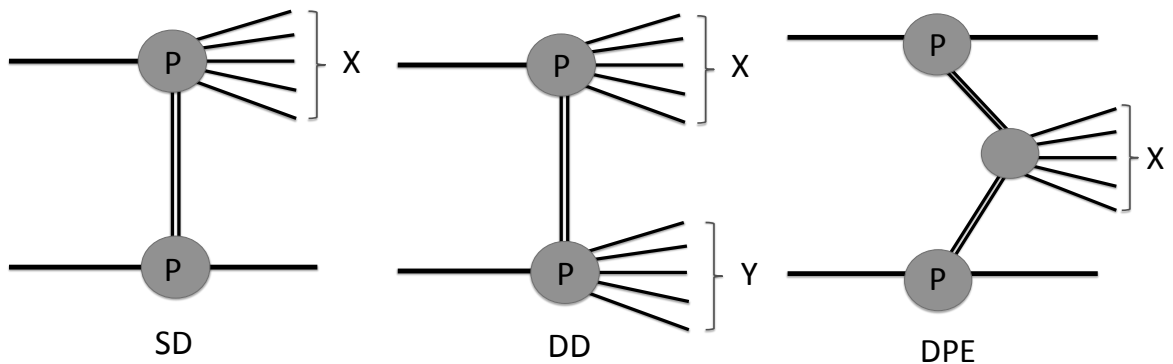


Figure 4.1: Schematic illustrations of the single (left), double (center) dissociation and double pomeron exchange processes (right).

- Single diffraction (SD, $pp \rightarrow pX$, Figure 4.1 left) includes processes in which one proton dissociates into system which carries quantum numbers of the proton and the second proton remains intact. The rapidity gap is produced in forward region separating the diffractive proton and the dissociated system.
- Double diffraction (DD, $pp \rightarrow XY$, Figure 4.1 center) in which both protons are broken. Each dissociated system carries the quantum numbers of the protons and they are separated

by a central rapidity gap.

- Central diffraction (CD, $pp \rightarrow pXp$, Figure 4.1 right) is class of processes in which both protons remain intact and system with quantum numbers of vacuum is produced in the central region. There are two rapidity gaps between the protons and the centrally produced hadronic system. These reactions are also often called double pomeron exchange (DPE)

The rapidity gaps and elastic scattering are explained in theory as an exchange of object which carries vacuum quantum numbers. For soft diffractive processes, that dominate the diffractive cross section, pQCD cannot be used. They are described by phenomenological models based on Regge theory.

Regge theory was developed in 1960s when the interest in quantum fields theories as theories for description of strong interaction declined. It is based on the analytical properties of scattering amplitudes which was a popular approach at those times and despite the fact that other S-matrix theories failed the Regge theory turned out to be extremely successful in the description of elastic scattering, diffraction and the total hadron-hadron cross section. As will be described in the next section, the Regge theory models hadronic interactions by an exchange of reggeons and pomerons carrying vacuum quantum numbers.

In cases when pQCD can be used, the pomeron can be incorporated in QCD although the description is more complicated than in simple Regge theory. Colour singlet object in QCD can be represented as an exchange of at least two gluons. If the pomeron has large virtuality it can be described as a BFKL gluon ladder [10]. This hard pomeron has different properties from Regge pomeron, and it will be briefly discussed in the next sections.

Rarely, diffractive processes can produce object with high transverse momentum as jets, high p_T leptons, etc. This kind of processes is usually called hard diffraction even though the pomeron is soft i.e. the virtuality Q^2 of pomeron is small. Pomeron is considered to have an internal structure and the cross section is described in terms of diffractive distribution functions in a similar way as in the case of non-diffractive PDFs.

Finally, there is an interesting class of central diffractive processes in which a central object is produced exclusively accompanied by scattered beam protons only. The similar topology can occur in processes initiated by two photon exchange which can be described in QED with high accuracy. These exclusive processes are very rare but they can play an important role in precise searches for new physics at LHC.

4.1 Regge Theory

Regge theory is based on the properties of the S-matrix which is a linear, relativistically invariant operator that evolves initial state $|i\rangle$ at time $-\infty$ to final state $|f\rangle$ at time $+\infty$

$$S|i\rangle = |f\rangle. \tag{4.1}$$

Subtracting the identity operator, which corresponds to the trivial case of nothing happening, the transition matrix T is defined as $S = \mathbb{1} + iT$. Transition matrix is related to scattering amplitude $A(i \rightarrow f)$ as follows

$$T = (2\pi)^4 \delta^4(p_i - p_f) A(i \rightarrow f), \quad (4.2)$$

where delta function enforces four-momentum conservation. Using the scattering amplitude $A(i \rightarrow f)$ differential cross section can be computed as

$$d\sigma = \frac{1}{\Phi} |A(i \rightarrow f)|^2 d\Pi_n, \quad (4.3)$$

where Φ is initial flux and $d\Pi_n$ is the Lorentz-invariant phase-space for n particles in final state.

An important property of the S-matrix is unitarity $S^\dagger S = S S^\dagger = \mathbb{1}$ which is a direct consequence of probability conservation. The unitarity of the S-matrix immediately leads to important theorem called optical theorem which relates total cross and elastic cross section of $1+2 \rightarrow 3+4$ reaction by relation

$$\sigma_{\text{tot}} = \frac{2}{\Phi} \text{Im} A_{\text{el}}(s, t=0) \simeq_{s \rightarrow \infty} \frac{1}{s} \text{Im} A_{\text{el}}(s, t=0), \quad (4.4)$$

where $s = (p_1 - p_2)^2$ is center-of-mass momentum square and $t = (p_1 - p_3)^2$ momentum transfer.

Another crucial features for the Regge theory are analytical properties of the S-matrix and crossing symmetry. The starting point for the construction of Regge theory is partial-wave expansion of the scattering amplitude in the s-channel

$$A(s, \cos \theta) = \sum_{l=0}^{\infty} (2l+1) A_l(s) P_l(\cos \theta) \quad (4.5)$$

$$A_l(s) = \frac{1}{2} \int_{-1}^1 d \cos \theta P_l(\cos \theta) A(s, t(\cos \theta, s)), \quad (4.6)$$

where θ is a polar scattering angle in center-of-mass frame in s channel and $P_l(\cos \theta)$ are Legendre polynomials.

The representation is well defined in the s-channel domain $s \leq 4m^2$ and $-1 \leq z \leq 1$ but it cannot be continued into t and u channels. This problem was solved by Regge who came with the idea to analytically continue the $A_l(s)$ into the complex values of angular momentum l . It can be shown [10] that the behavior of $A(s, t)$ is governed by pole contributions called Regge poles. At large t the dominant contribution is given by leading simple pole $l_i = \alpha_i(t)$ (for which $\text{Re } l_i$ is largest) and scattering amplitude has a form

$$A(s, t) \approx_{s \rightarrow \infty} -\beta(t) \frac{1 + \xi e^{-i\pi\alpha_i(t)}}{\sin \pi\alpha_i(t)} s^{\alpha_i(t)}, \quad (4.7)$$

where $\beta_i(t)$ is a residuum of $\alpha_i(t)$ and the quantum number called signature takes values $\xi = \pm 1$. The scattering amplitude has the same form for asymptotic behavior at large t with t replaced by s .

The poles in Regge theory are interpreted as resonances or bound states of increasing angular momentum l . The $\alpha(t)$, that interpolates such resonances, is called a Regge trajectory (or Reggeon). Regge trajectory is usually approximated by first two terms in Taylor series expanded around $t = 0$ as

$$\alpha(t) = \alpha(0) + \alpha' t, \quad (4.8)$$

where $\alpha(0)$ is called reggeon intercept and α' reggeon slope of the trajectory. This approximation is actually good for rather large values of t (several units of GeV^2). The leading mesonic trajectories were fitted in data and it gives the reggeon intercept to be $\alpha(0) = 0.5$ and reggeon slope of order 1 GeV^{-2} . In the case of baryonic trajectories the slope is very similar but the intercept is lower and for some of these trajectories even negative.

The general properties of the S-matrix suggests that the Regge pole residue in equation (4.7) should factorize into coupling at each vertex. Thus, in the case of simple reggeon exchange showed in Figure 4.2 the amplitude can be rewritten as

$$A(s, t) = g_{13} g_{24} \eta(t) s^{\alpha(t)} \quad (4.9)$$

where

$$\eta(t) = \frac{1 + \xi e^{-i\pi\alpha(t)}}{\sin \pi\alpha(t)} \quad (4.10)$$

and $g_{13}(t)$, $g_{24}(t)$ are coupling at the corresponding vertices.

Using optical theorem on relation (4.9) one immediately obtains prediction for the total cross section which in the case of a single pole contribution reads

$$\sigma^{\text{tot}} \simeq_{s \rightarrow \infty} \frac{1}{s} \text{Im} A(s, t = 0) \sim s^{\alpha(0)-1}. \quad (4.11)$$

Since the intercept for the Regge theories does not exceed 0.5 the total cross section should decrease with increasing energy. However, this is not observed by experiments and the total cross section is rather flat around energy $\sqrt{s} \sim (10-20) \text{ GeV}$. In order to keep such behavior of the total cross section a new Regge trajectory with intercept equal to 1 and quantum numbers of a vacuum was introduced. In fact the data shows that pomeron intercept slightly deviates from unity, as will be shown later, and it is convenient to denote this deviation by ϵ . This trajectory is called pomeron after I. Ya. Pomeronchuk and does not correspond to any known particle or resonance. The dependency of the total cross section on the center-of-mass energy \sqrt{s} can be described using simple Regge-inspired parameterization introduced by Donnachie and Landshoff

(1992) [11]

$$\sigma^{\text{tot}} = X s^{0.0808} + Y s^{-0.4525}, \quad (4.12)$$

where X and Y are reaction independent free parameters. The first term in (4.12) is interpreted as a pomeron exchange whereas the second term corresponds to the reggeon contribution. It can be seen from equation (4.11) that the pomeron and reggeon intercept yield values of $\alpha_{\text{P}}(0) = 1.0808$ and $\alpha_{\text{R}}(0) = 0.5475$.

The pomeron slope has been determined from a fit of the elastic cross section which takes a form according to Regge theory as

$$\frac{d\sigma^{\text{el}}}{dt} = F(t) s^{2\alpha(0)-2} e^{-2\alpha'|t|\ln s}, \quad (4.13)$$

where $F(t)$ is a function of t containing the residue function and the signature factor. The fit estimates the slope to be much flatter than the Reggeon slopes $\alpha'_{\text{P}} = 0.25 \text{ GeV}^{-2}$. The pomeron is the dominant trajectory in high energies in both elastic and diffractive process.

The dependence of the total cross section as a function of energy is usually parameterized by $\ln^\gamma s$, where the results of the fit gives $\gamma \approx 2$. The exponential behavior in equation (4.12) of the pomeron term violates the unitarity based on Froissart-Martin bound which states that the total cross section cannot grow faster with center-of-mass energy than $C \ln^2 s$. Thus the formula (4.12) represents effective behavior violating unitarity at relatively high energies. There are some phenomenological concepts which cure the exponential behavior of the total and elastic cross sections predicted by Regge theory by using the eikonal approach taking into account rescattering effects, see ref. [12, 13].

As it was previously mentioned the pomeron concept can be also introduced in QCD if the pomeron virtuality is large and the perturbative theory can be used. This hard BFKL pomeron is expressed in terms of so called reggeized gluon ladders exchanges [10]. However, properties of the BFKL pomeron differ from the Donnachie and Landshoff pomeron. The leading singularity in the BFKL scattering amplitude is a cut rather than a simple pole and moreover, the pomeron intercept is very large $\alpha_{\text{P}}(0) \approx 1.5$. Nevertheless, it seems that correct description of the minimum bias data requires combination of the phenomenological Regge inspired model and QCD BFKL description. This is presented for example in recent model of Khoze, Martin and Ryskin (KMR) [14] which combines hard BFKL pomeron description with a dedicated treatment of low mass diffraction motivated by original s-channel picture of Good and Walker [15], in which proton and excited proton eigenstates scatter elastically from the target with different absorption coefficients. Their model leads to a considerable enhancement of cross section for low mass production which is compatible with current LHC data.

4.2 Soft Diffraction Phenomenology

Soft diffractive phenomena cannot be described in pQCD due to small momentum transfer. Instead phenomenological description based on the Regge theory reviewed in the previous chapter is employed. The majority of the currently used theoretical models are based on a triple pomeron coupling approach. One of the main ingredient for its derivation is a consequence of the optical theorem called Mueller's generalized optical theorem. It extends optical theorem to relate inclusive cross section $1 + 2 \rightarrow 3 + X$ to discontinuities of three-body forward elastic amplitude $A_{12\bar{3}}(s, t, M^2)$ of reaction $1 + 2 + \bar{3} \rightarrow 1 + 2 + \bar{3}$. The mathematical form of the theorem is

$$(2\pi)^3 2E \frac{d^3\sigma}{d^3p} = \frac{1}{s} \text{Disc}_{M^2} A_{12\bar{3}}(s, t, M^2), \quad (4.14)$$

where $M^2 = (p_1 + p_2 - p_3)^2$ is square of the mass of the produced hadronic system X and Disc_{M^2} denotes discontinuity in the mass plane.

A scattering amplitude for the single inclusive reaction $1 + 2 \rightarrow 3 + X$ can be expressed using the Regge theory in the form

$$A(12 \rightarrow 3X) \sim \sum_i g_{13}^i(t) g_{2X}^i(t) \eta_i(t) \left(\frac{s}{M^2}\right)^{\alpha_i(t)}, \quad (4.15)$$

where M^2 is invariant mass of the hadronic system X , the sum runs over the contributing reggeons and the relation $\cos\theta_t \sim (s/M^2)$ as $s \rightarrow \infty$ was used. Using the Mueller's generalized optical theorem (4.14) one can derive the following formula

$$16\pi^2 s \frac{d^2\sigma^{\text{SD}}}{dM^2 dt} = \sum_{i,j,k} g_{13}^i(t) g_{13}^{j*}(t) \eta_i(t) \eta_j^*(t) \left(\frac{s}{M^2}\right)^{\alpha_i(t) + \alpha_j(t)} g_{22}^k(0) g_{ijk}(t) (M^2)^{\alpha_k(0)}, \quad (4.16)$$

where g_{ijk} is the triple reggeon coupling. The schematic derivation of the triple reggeon diagram (4.16) can be seen in Figure 4.3. In the case of SD reactions the outgoing hadron 3 carries the same quantum numbers as the initial hadron 1. Therefore the trajectories i and j have to be the pomeron trajectories. The last trajectory k can be either pomeron or reggeon but for large masses M^2 the pomeron trajectory dominates and thus the reggeon contribution is usually neglected. Furthermore, it is experimentally known that the triple pomeron coupling is nearly independent of t and thus the cross section (4.16) can be written in factorized form

$$s \frac{d^2\sigma^{\text{SD}}}{dM^2 dt} = \frac{1}{16\pi^2} |g_{\mathbb{P}}|^2 \left(\frac{s}{M^2}\right)^{2\alpha_{\mathbb{P}}(t)-1} \sigma_{\mathbb{P}}(M^2), \quad (4.17)$$

where $\sigma_{\mathbb{P}}(M^2)$ is pomeron cross section and the rest is called pomeron flux with pomeron-proton coupling $g_{\mathbb{P}}$. Diffractive processes are usually described in variable $\xi = M^2/s$. In the case of the single diffractive processes ξ corresponds to fractional momentum loss of the diffractive proton i.e $\xi = |\vec{p}_3|/|\vec{p}_1|$. The factorized cross section expressed in ξ reads

$$\frac{d^2\sigma^{\text{SD}}}{d\xi dt} = f_{\mathbb{P}}(\xi, t) \sigma_{\mathbb{P}}(M^2) \quad (4.18)$$

with pomeron cross section $\sigma_{\mathbb{P}}(M^2)$ and pomeron flux $f_{\mathbb{P}}(\xi, t)$ given by

$$f_{\mathbb{P}}(\xi, t) = \frac{1}{16\pi^2} |g_{\mathbb{P}}|^2 \xi^{1-2\alpha_{\mathbb{P}}(t)} \quad (4.19)$$

$$\sigma_{\mathbb{P}}(M^2) = g_{\mathbb{P}}(0) g_{\mathbb{P}\mathbb{P}\mathbb{P}}(0) (M^2)^{\alpha_{\mathbb{P}}(0)-1}. \quad (4.20)$$

Description of double diffractive dissociation in which both protons dissociate into systems X and Y having masses M_X and M_Y can be derived in similar way. The cross section can be written as a factorization of two SD and elastic scattering cross sections

$$\frac{d^3\sigma^{\text{DD}}(12 \rightarrow XY)}{dM_X^2 dM_Y^2 dt} = \frac{d^2\sigma^{\text{SD}}(12 \rightarrow X2)}{dM_X^2 dt} \frac{d^2\sigma^{\text{SD}}(12 \rightarrow Y1)}{dM_Y^2 dt} / \frac{d\sigma^{\text{el}}(12 \rightarrow 12)}{dt} \quad (4.21)$$

and using equations (4.13) and (4.20) one can obtain formula

$$16\pi^3 s \frac{d^3\sigma^{\text{DD}}(12 \rightarrow XY)}{dM_X^2 dM_Y^2 dt} = g_{\mathbb{P}}^2(0) g_{\mathbb{P}\mathbb{P}\mathbb{P}}^2(0) \left(\frac{s}{M_X^2 M_Y^2} \right)^{2\alpha_{\mathbb{P}}(t)-1} (M_X^2)^{\alpha_{\mathbb{P}}(0)-1} (M_Y^2)^{\alpha_{\mathbb{P}}(0)-1}. \quad (4.22)$$

In the following, the convention $M_Y < M_X$ is adopted.

In order to experimentally constrain diffractive models, it is important to realize that there is a strong correlation between size of rapidity gap Δy and variables ξ_X , ξ_Y . For SD event, the rapidity gap between the final state proton and the system X satisfies

$$\Delta y \simeq -\ln \xi_X. \quad (4.23)$$

In experiments, pseudorapidity of particle

$$\eta = -\ln \tan \left(\frac{\theta}{2} \right), \quad (4.24)$$

where θ is particle polar angle, is used as an approximation of particle rapidity y . Since the equality $y = \eta$ holds for particle with zero mass, the approximation is very accurate for high energetic particles where the mass of the particle can be neglected. Therefore using the pseudorapidity gap instead of rapidity gap in (4.23) does not increase the error of the relation. It follows from equations (4.23) and (4.18) that the differential cross section as a function of rapidity gap size, $\Delta\eta$, for single diffractive processes is approximately constant

$$\frac{d\sigma^{\text{SD}}}{d\Delta\eta} \simeq \text{constant}. \quad (4.25)$$

To conclude, the ξ dependence in diffractive models can be experimentally constrained either by direct measurement of momentum fraction loss in SD events or by measurement of rapidity gap distribution. The former method requires proton taggers allowing to detect the intact diffractive protons propagating very close to the beam inside the beam pipe. The later approach has been used in the analysis presented in Chapter 11.

As in the case of the total cross section the triple-Regge description of the SD cross section behaves as $\sigma^{\text{SD}} \sim s^{2\epsilon}$ which violates the unitarity for sufficiently large energies. Moreover, it

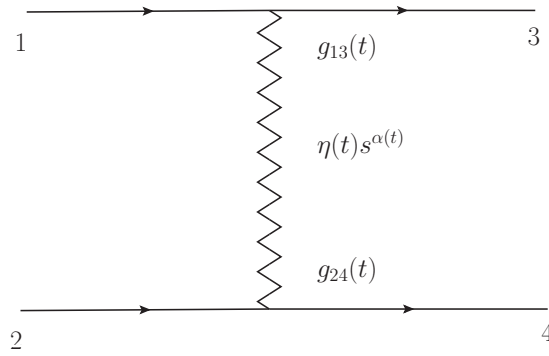


Figure 4.2: Simple reggeon exchange diagram.

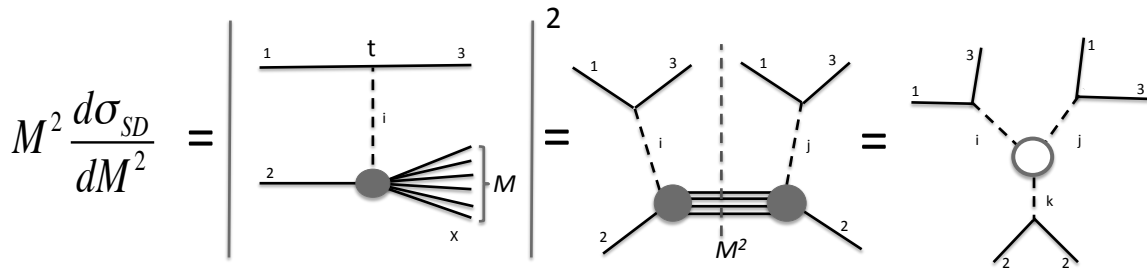


Figure 4.3: Schematic derivation of SD cross section using Mueller's generalized optical theorem which leads to triple reggeon coupling shown in the most right diagram.

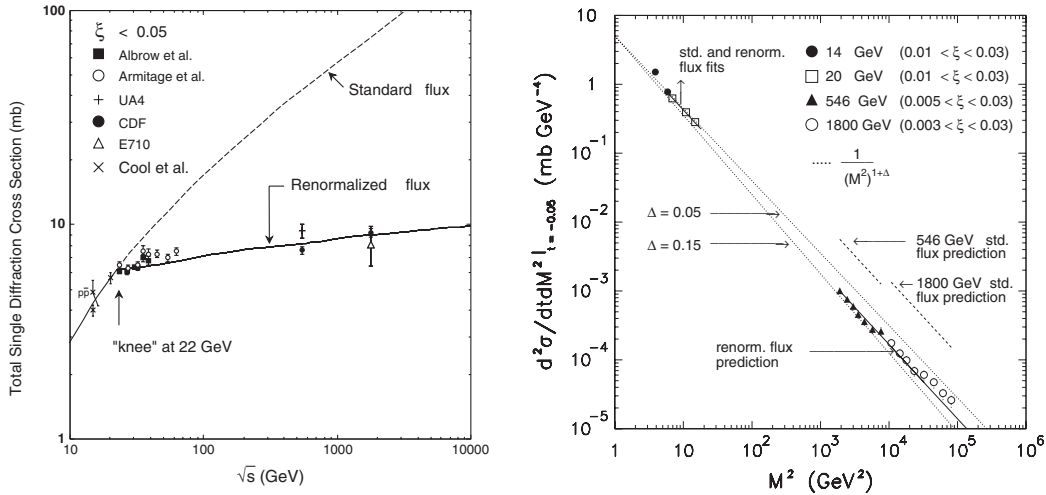


Figure 4.4: Deviation of standard Regge description from data. Left plot shows single diffractive $pp/\bar{p}p$ cross section for $\xi < 0.05$ as a function center-of-mass energy \sqrt{s} . Differential cross section $\partial^2\sigma^{SD}/\partial M^2\partial t$ in $\bar{p}p$ collisions at $t = -0.05 \text{ GeV}^2$ at different energies $\sqrt{s} = 14, 20, 546$ and 1800 GeV is presented. The renormalized flux invented by Goullianos agrees with data for both distributions. Plots are taken from ref. [16,17].

grows even faster than the total cross section. This theoretical threat is fulfilled and triple-Regge description starts to deviate from the data already at $\sqrt{s} = 22 \text{ GeV}$, see Figure 4.4. Goullianos proposed in ref. [16] unitarization procedure in which the pomeron flux is considered as a probability density simply describing the ξ and t distributions of the exchanged Pomeron in a diffractive process. Thus the flux is renormalized to have the integral over ξ and t equal to one. It can be seen in Figure 4.4 that such a phenomenological approach leads to surprisingly excellent description of data. Furthermore, it also follows a dependency of the single diffractive cross section as a function of invariant mass squared M^2 of the dissociated system.

4.3 Hard Diffraction Phenomenology

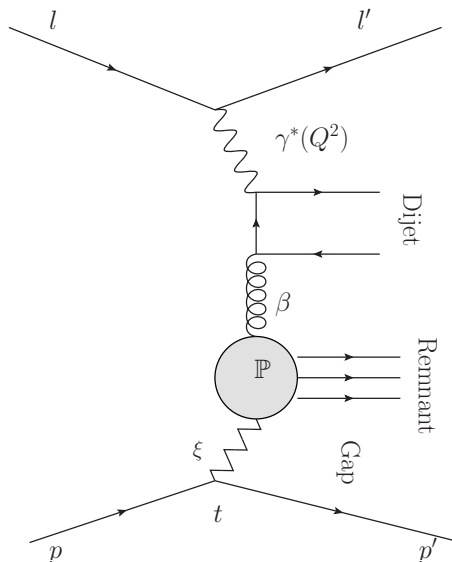


Figure 4.5: Leading order diagram for diffractive di-jet production in DIS.

The investigation of processes in which high p_T objects, such as jets, are produced is relatively a new field of research. The first diffractive jet production with large rapidity gaps was observed by the UA8 collaboration in 1988 [18]. In the following years the hard diffraction has been intensively studied at HERA but also at $p\bar{p}$ collisions at the Tevatron. The observation of a surprisingly large contribution of diffractive processes to DIS (5-10%) rise an interest of physics community about this phenomena. Diffractive DIS

$$l(k) + \text{proton}(p) \rightarrow l(k') + \text{proton}(p') + X \quad (4.26)$$

is characterized by the rapidity gap between the scattered proton with momentum p' and hadronic final state X what suggests an exchange of object with vacuum quantum numbers between the proton and virtual photon γ^* , see Figure 4.5. There is also a fraction of events in which the proton dissociates and produces a hadronic system Y with the same quantum numbers as proton.

The hadronic system Y is separated by rapidity gap from the hadronic system X . This process is called double diffraction in DIS.

Diffractive DIS is described by the same set of kinematical variables as inclusive DIS (3.14-3.18), but in order to describe three-momentum of the outgoing proton, \vec{p}' , the set of kinematical variables is supplemented by momentum transfer squared, t , and proton fractional momentum loss, ξ , defined as

$$t = -(p' - p)^2, \quad (4.27)$$

$$\xi = \frac{(p - p') \cdot q}{p \cdot q}. \quad (4.28)$$

The cross section for diffractive DIS can be written in analogy with inclusive DIS. It has been proven in pQCD that factorization theorem holds also in the case of diffractive processes in DIS [19]. Hence, the cross section can be written in terms of diffractive parton distribution function $f^D(x, Q^2, \xi, t)$

$$d\sigma^{\epsilon P \rightarrow eXY} = \sum_i f^D(x, Q^2, \xi, t) \otimes d\sigma^{ei}(x, Q^2), \quad (4.29)$$

where the sum runs over all parton flavours in proton and $d\sigma^{ei}(x, Q^2)$ is parton electron cross section. In analogy to DIS, the diffractive PDF expresses a probability to find a parton with the momentum fraction x and virtuality up to Q^2 inside hadron h .

The form of the diffractive PDF function $f^D(x, Q^2, \xi, t)$ can be determined from the predictions of the Regge theory. Generalizing the result from the previous chapter into γ^*p collision in DIS one finds that the diffractive PDF can be further factorized into a pomeron (reggeon) flux $f_{\mathbb{P}(\mathbb{R})/p}(\xi, t)$ and a pomeron (reggeon) distribution function $f_i^{\mathbb{P}(\mathbb{R})}(\beta, Q^2)$ (introduced by Ingelman and Schlein [20]) which in general has a form

$$f^D(x, Q^2, \xi, t) = f_{\mathbb{P}/p}(\xi, t) f_i^{\mathbb{P}}(\beta, Q^2) + \eta_{\mathbb{R}} f_{\mathbb{R}/p}(\xi, t) f_i^{\mathbb{R}}(\beta, Q^2), \quad (4.30)$$

where variable

$$\beta = \frac{Q^2}{2q \cdot (p - p')} \quad (4.31)$$

is interpreted as the momentum fraction of the struck parton inside the pomeron (reggeon) and satisfies the relation $x = \beta\xi$. It is worth mentioning that recent measurements of diffractive PDF at HERA [21] show that pomeron is composed mostly by gluons. The pomeron (reggeon) flux motivated by Regge theory is parameterized in the following

$$f_{\mathbb{P}(\mathbb{R})/p}(\xi, t) = A_{\mathbb{P}(\mathbb{R})} \frac{e^{B_{\mathbb{P}(\mathbb{R})}t}}{\xi^{2\alpha_{\mathbb{P}(\mathbb{R})}-1}}. \quad (4.32)$$

The pomeron (reggeon) trajectory is again approximated by first two terms of Taylor series $\alpha(t) = \alpha(0) + \alpha' t$. For large masses of the hadronic system X the pomeron contribution dominates

and reggeon term in (4.30) is usually neglected. The pomeron distribution function cannot be determined from the first principles. Its boundary conditions at Q_0^2 has to be fitted from data and its evolution in Q^2 is obtained from the solution of DGLAP equations (3.26).

Measurements at lepton-hadron collisions suggest that the behavior of the diffractive processes can be describe in the same way as inclusive DIS. There is however one major difference. The diffractive PDF are not universal in the sense that the factorization (4.30) breaks down at hadron-hadron colliders contrary to non-diffractive production.

The factorization breaking has been observed in all three diffractive topologies SD, DD, and DPE processes at the Tevatron. The usual method is measurement of ratio of diffractive to non-diffractive production rate $R = D/ND$ which is compared to the same ratio obtained at HERA. The measurements of SD and DD di-jet at energies $\sqrt{s} = 1800$ GeV and $\sqrt{s} = 630$ GeV production show suppression by factor 10 and 5 respectively. The suppression of the diffractive production at hadron-hadron colliders is a consequence of a presence of another, predominantly soft, parton interactions during the hadron collision. It should be pointed out that this suppression is similar to the one observed in soft diffractive processes with respect to the Regge predictions which was discussed in the previous chapter.

In 1993, Bjorken came with theoretical concept of gap survival probability $\langle S^2 \rangle$ [22] which is defined as the fraction of events in which additional interactions do not spoil the rapidity gap. The survival probability is defined in an eikonal picture which is an approximation technique of high energy forward scattering originally developed for potential scattering in Quantum Mechanics where particle energy dominates the interaction potential [10]. If the processes producing rapidity gaps can be calculated by

$$\sigma(s) = \int db^2 A(b, s) \sigma(b, s), \quad (4.33)$$

where $A(b, s)$ describes parton densities in transverse plane of colliding hadrons and $\sigma(b, s)$ is a cross section for given impact parameter b . The survival probability is then given by

$$\langle S^2 \rangle = \frac{\int db^2 A(b, s) \sigma(b, s) S^2(s, b)}{\sigma(s)}, \quad (4.34)$$

in which $S^2(s, b)$ is probability that two hadrons pass through each other at impact parameter b without any interaction. Since it is reasonable to expect that with increasing \sqrt{s} the interactions between the hadron remnants become stronger and thus there is a higher probability to destroy the gap, the concept of survival probability explains an observed decrease of ratio R_{ND}^D with growing center-of-mass energy \sqrt{s} .

The survival probability factor is currently the largest uncertainty for description of diffractive and exclusive processes at the LHC. The results depend on the model used for parameterization of $S^2(s, b)$ and parton densities $A(b, s)$. For SD production at $\sqrt{s} = 14$ TeV the predictions are about 6% [23]. Recent preliminary result, of the measurement of diffractive di-jets with

transverse momentum $p_T > 20$ GeV at $\sqrt{s} = 7$ TeV [24] done by the CMS collaboration, sets the upper limit on the rapidity gap survival probability around 21%.

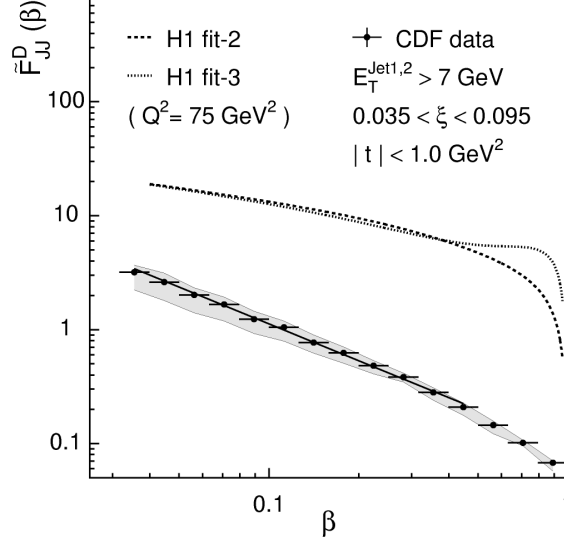


Figure 4.6: Diffractive structure function as a function of β measured by CDF collaboration [25]. Data are compared with expectation from the parton densities of the proton extracted from DIS measured by H1 collaboration [26].

In the case of SD di-jet production $p\bar{p} \rightarrow \bar{p}X$, CDF collaboration has been able to extract the diffractive structure function¹ of the anti-proton $F_{jj}^D(\beta)$ [25]. They measured SD to ND ratio as a function of Bjorken x , $R_{ND}^{SD}(x)$. In leading order of pQCD, the $R_{ND}^{SD}(x)$ is equal to the ratio of SD to ND structure function of \bar{p} . Hence, the diffractive structure function $F_{jj}^D(\beta)$ can be obtained by multiplying the $R_{ND}^{SD}(x)$ by the known inclusive structure function

$$F_{jj}(x) = x \left[g(x) + \frac{4}{9} \sum_f (g_f(x) + \bar{q}_f(x)) \right], \quad (4.35)$$

and by substituting $\beta = x/\xi$. Obtained distribution shows a large discrepancy in both shape and normalization of diffractive structure functions as can be seen in Figure 4.6.

It is interesting to study the factorization breaking in diffractive processes where multiple gaps are produced. In the DPE two rapidity gaps separate proton and anti-proton from the centrally produced system. CDF collaboration [27] measured a ratio of DPE to SD di-jet events $R_{SD}^{DPE}(x)$ as a function of Bjorken scaling variable x . If the factorization breaking is proportional

¹The structure of the differential cross section in (diffractive) DIS $d\sigma/dQ^2 dx$ ($d\sigma/dQ^2 dx d\xi dt$) is determined from the Lorentz invariance, unitarity, gauge invariance and parity conservation apart from the so called (diffractive) proton structure functions $F_i(x, Q^2)$ ($F_i(x, Q^2, \xi, t)$), where $i = 1, 2$ in γ^*p scattering, containing information about proton structure. The structure functions are proportional to (diffractive) parton distribution functions, see more in ref. [10].

to number of gaps, the equality

$$R_{\text{ND}}^{\text{SD}}(x) = R_{\text{SD}}^{\text{DPE}}(x) \quad (4.36)$$

should hold. However, the result of the measurement which can be seen in Figure 4.7 indicates that relation (4.36) is not satisfied. The double ratio $DR = R_{\text{ND}}^{\text{SD}}/R_{\text{SD}}^{\text{DPE}}$ is estimated to be 0.19 [27]. Thus if another soft parton is irradiated it spoils both gaps in DPE with an approximately the same probability as one gap in SD.

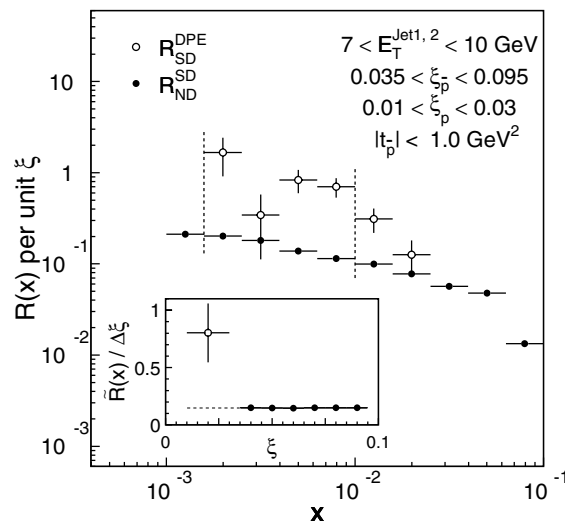


Figure 4.7: Ratios of DPE to ND and SD to ND di-jet event rates per unit ξ as a function of Bjorken x measured by CDF [27].

Apart from the diffractive di-jet production, Tevatron also investigated a production of W/Z [28] bosons which in combination with results on diffractive di-jets and b-quark production [29] is sensitive to gluon content of the pomeron.

4.4 Central Exclusive Production in QCD

Great attention has been recently paid to central exclusive production (CEP) $p\bar{p} \rightarrow p \oplus X \oplus \bar{p}$ in which exclusively produced object is accompanied only with the two intact beam protons which are separated by two large rapidity gaps denoted by \oplus . Such clean environment provides an opportunity for accurate measurements even at hadron colliders. An invariant mass of exclusively produced object X can be precisely measured from the deflection of collided protons.

The protons are usually slightly deflected that they remain in the beam pipe and propagate through the magnetic field, close to the beam. Hence, special instruments permitting the detectors to approach as close as possible to the beam such as, Roman pots or Hamburg beam pipes, are used for measurement of the proton position. The measured proton position then allows a

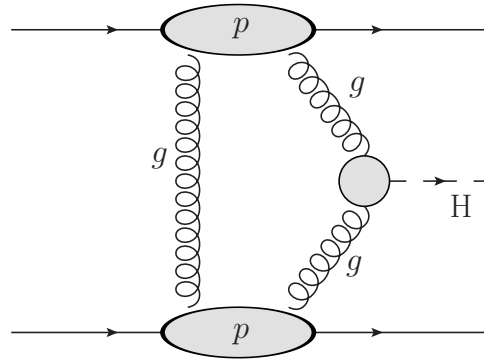


Figure 4.8: Leading order diagram for exclusive Higgs boson productions in pp collision.

reconstruction of fractional momentum loss of the proton $\xi = |\vec{p}'|/|\vec{p}|$. The invariant mass M_X is then given by

$$M_X \approx \sqrt{\xi_1 \xi_2 s}, \quad (4.37)$$

where ξ_1 and ξ_2 are fractional momentum losses of the protons and s is center-of-mass energy squared. In addition, the centrally produced object has almost zero orbital momentum in z direction $J_z \approx 0$ in exclusive events. This implies that the production of di-jet system with mass M_{jj} initiated by quarks with mass m_q is suppressed by factor m_q/M_{jj} and thus the heavy quark production is enhanced at given M_{jj} . Moreover, the produced system has to carry a positive C-charge conjugation and P-parity which is the consequence of gluon exchange with the quantum numbers of a vacuum.

One of the biggest motivation for measurement of the QCD exclusive processes was measurement of the Higgs boson at LHC. Even though Monte Carlo studies suggest that the measurement of the SM Higgs will not be possible due to its small cross section which has been estimated to be 3 fb [30] there are still possibilities of light Higgs in MSSM scenario or other exotic measurements for which exclusive production can be used [31].

There are several phenomenological models describing exclusive QCD production. The non-perturbative Bialas-Landschoff model [32] applies Regge theory in order to describe exclusive production. The exclusivity of the process is provided by exchange of two reggeized gluons between interacting hadrons and hard subprocess which is then described by perturbative QFT.

A perturbative QCD approach was invented in Durham by Khoze, Martin and Ryskin [30]. Since their model is currently the most successful in description of available data, we choose it for implementation to the HERWIG++ MC generator. Therefore this model is worth a closer description which can be found in Section 7.3.1.

It should be mentioned that a perturbative model with similar approach as KMR has been recently developed by Cudell, Hernández, Ivanov, Dechambre which differs from KMR mainly by different kinematical assumptions [33].

Different explanation of rapidity gaps and exclusivity is achieved by Soft Color Interaction

model [34]. In this case, the colour singlet exchange is achieved by additional soft gluon exchange. In particular, when the gluon from the proton enters to the hard processes it leaves the proton remnant and the hard scattering state in the colour octet state. An additional soft gluon exchange which takes place at hadronisation phase can change these objects back into the colour singlet states separated by rapidity gap. This model has a great success at HERA but it can provide also alternative description of exclusive processes in hadron-hadron collisions.

The first measurement of central exclusive processes in hadron-hadron collisions has been made at Tevatron by CDF collaboration in which exclusive production of di-jet system was observed [35]. In order to distinguish CEP processes from the inclusive DPE in which both protons also remain in the beam pipe, they used the following observable

$$R_{jj} = \frac{M_{jj}}{M_x}, \quad (4.38)$$

in which M_{jj} is the di-jet mass and M_x is the mass of the whole final state excluding the p and \bar{p} . In the case of CEP di-jet production it is expected that $R_{jj} = 1$, while for the DPE di-jet production the R_{jj} distribution should be concentrated at smaller values due to the presence of pomeron remnants. The excess of the events with $R_{jj} \approx 1$ has been observed and described by the MC implementation of KMR (EXHUME [36]) and Bialas-Landschoff model (DPEMC [37]). It should be mentioned that the Bialas-Landschoff model predicts much weaker p_T spectra of the jets than perturbative KMR model. More tests have been done in order to tune parameters of models for exclusive diffraction. This is necessary if one wants to use the models for measurement of new physics at the LHC. For example Tevatron made observations of exclusive production of charmonium state χ_C [38] and few rare events of $\gamma\gamma$ [39] which give further constraints to CEP models. Recently, LHCb collaboration presented its preliminary results on the measurements of exclusive χ_C and $J/\Psi, \Psi(2S)$ at $\sqrt{s} = 7$ TeV [40] which are in good agreement with theoretical predictions.

4.5 Photon Initiated Processes

Exclusive production of some final states such as di-leptons, WW in SM is dominated by two-photon exchange rather than gluon singlet exchange. The interaction of the photons yields production of central object separated by large rapidity gaps from the scattered intact hadrons. The schematic diagram of two photon production can be seen in Figure 4.9. Such mechanism is well described in the framework of Quantum Electrodynamics in which the cross section can be very precisely computed as a convolution of photon luminosity and hard interaction of the radiated photons. The probability of emitting photon with virtuality Q^2 and carrying momentum fraction x of the initial proton is expressed by flux derived by Budnev [41]. This small Q^2 approximation will be described in Section 7.1 in more detail.

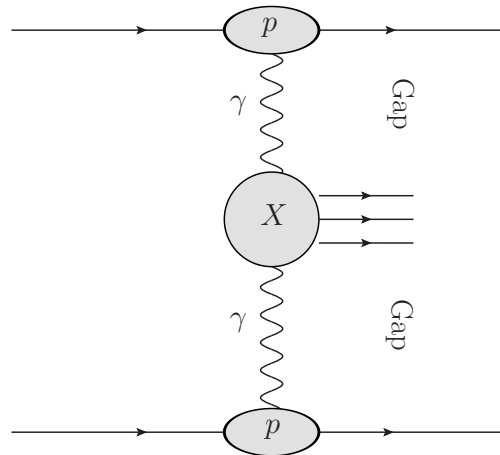


Figure 4.9: Diagram of two photon production of exclusive central system X in pp collisions.

In analogy to exclusive QCD processes, there is a possibility that an exchange of soft parton between outgoing protons can occur which leads to dissociation of the protons and spoils the rapidity gap. The Durham group estimates in [30] the survival probability in two photon production to be 0.75 and 0.9 for Tevatron and LHC ($\sqrt{s} = 14$ TeV) energies respectively. The cross sections for two photon production are very small (total cross section for WW at $\sqrt{s} = 14$ TeV is predicted to be 96 fb) and thus most of the interesting measurements can be done only at LHC. So far only production of e^+e^- [42] and $\mu^+\mu^-$ [38] pairs were measured by CDF at Tevatron and by CMS at LHC at $\sqrt{s} = 7$ TeV in small data sample 36 pb^{-1} [43]. The obtained results agree very well with the theoretical predictions.

Chapter 5

Large Hadron Collider and ATLAS Experiment

5.1 Large Hadron Collider

The Large Hadron Collider (LHC) is currently the most powerful hadron-hadron (ion-ion) collider in the world situated in Switzerland French boarder near Geneva. LHC is designed to accelerate proton beams with energy of 7 TeV and large instantaneous luminosity $\mathcal{L} = 1 \times 10^{34} \text{ cm}^2\text{s}^{-1}$. The luminosity expresses proportionality between event rate R_{ev} and cross section of the process of interest

$$R_{\text{ev}} = \mathcal{L}\sigma \quad (5.1)$$

and therefore high luminosity is desired for discoveries or precise measurement of rare processes. The luminosity depends on the beam parameters and in the case of beams with Gaussian distribution it can be written as

$$\mathcal{L} = \frac{N^2 n f_{\text{rev}} F}{4\pi\sigma_x\sigma_y}, \quad (5.2)$$

where N is number of protons in bunch, n number of bunches per beam, f_{rev} is revolution frequency, σ_x, σ_y are vertical and horizontal beam sizes, and F the geometric luminosity reduction factor due to beam crossing angle at the interaction point [44, 45].

Such high performance of LHC machine is achieved by 16 radio frequency cavities that accelerate the beams, 1232 super-conducting bending dipole magnets producing a magnetic field strength of 8.33 T, 392 focusing quadrupole and further optical elements which are distributed around the circle with circumference of 27 km.

There are several steps before the protons are injected to the LHC and accelerated into required energy. The accelerating complex with the main LHC detectors can be seen in Figure 5.1. First, the protons are extracted from hydrogen atoms using a high electric field and accelerated to energy of 50 MeV at linear accelerator Linac2. The protons continue to Proton Synchrotron

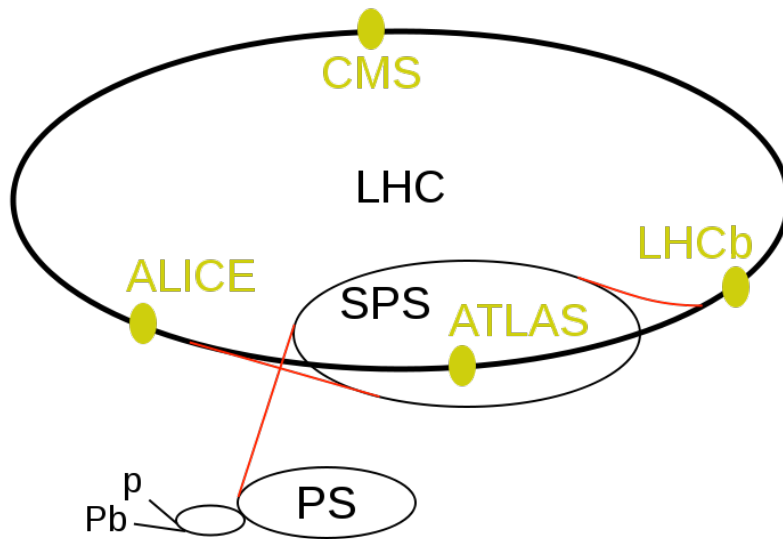


Figure 5.1: Schematic plot of CERN accelerator complex with LHC and its 4 main experiments.

Booster to obtain an energy of 1.4 GeV. After that, protons gradually increase their speed in Proton Synchrotron (PS) and Super Proton Synchrotron (SPS) to energies 25 GeV and 350 GeV respectively. Finally, the beams are fed to LHC where they are accelerated to final energy. After that, the beams are collided at four different interaction points (IP) at which six following experiments are placed: ATLAS [46], CMS [47], ALICE [48], LHCb [49], TOTEM [50], LHCf [51].

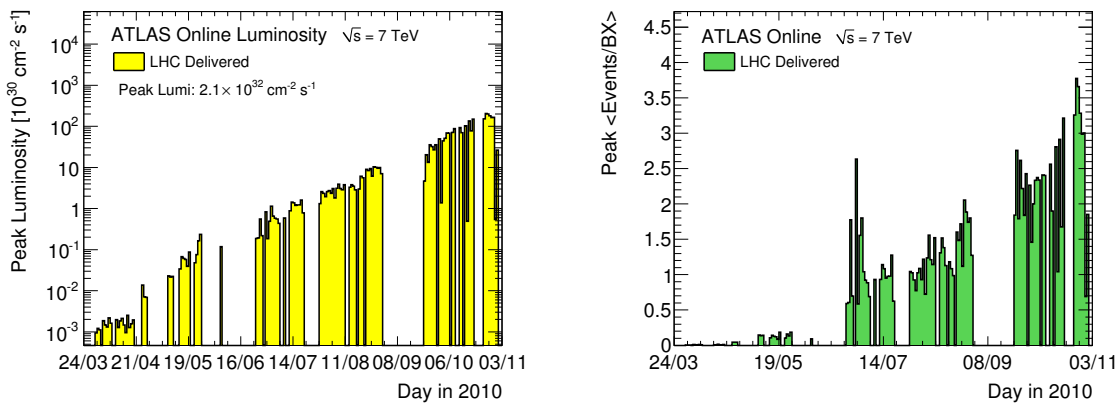


Figure 5.2: The maximum instantaneous luminosity versus week delivered to ATLAS (left) and average number of events per beam crossing at the start of an LHC fill versus day (right). Figures taken from ref. [52].

The LHC accelerated its first beam and recorded first collisions in September 2008. Due to an accident, which caused large damage on the accelerator optics, the LHC was shut down for more than one year. In November 2009, LHC was restarted again. In the first period, LHC accelerated

protons only up to 450 GeV and used beams of low intensity. In March 2010, the LHC started to collide protons with center-of-mass energy $\sqrt{s} = 7$ TeV, which was the largest energy that had been achieved in hadron-hadron colliders. The first periods of data taking were done at low instantaneous luminosity which was gradually increased during the year 2010, see Figure 5.2. Higher instantaneous luminosity can be achieved either by addition of further bunches into the beam, i.e. by increasing n in (5.2), or by squeezing the bunches, i.e. decreasing the beam size σ_x, σ_y . The later approach leads to higher probability of multiple collisions per bunch crossing which is described by Poisson distribution with the mean number of interactions μ given by

$$\mu = \sigma_{\text{tot}} \mathcal{L} / f, \quad (5.3)$$

where f is bunch crossing frequency. The bunch crossing frequency can differ from revolution frequency, f_{rev} , because not all the beam buckets around the ring where bunches could be injected have to be filled. It should be noted, that during a particular run the instantaneous luminosity decreases due to degradation of the beam. The degeneration of luminosity as a function of time has following dependence

$$\mathcal{L}(t) = \frac{\mathcal{L}_0}{(1 + t/\tau)^2}, \quad (5.4)$$

where initial decay time τ is given by the initial beam parameters. The peaked luminosity in the first LHC runs was $\mathcal{L} = 1 \times 10^{27} \text{cm}^2 \text{s}^{-1}$ which corresponds to $\mu \simeq 0.005$. While runs, collected by ATLAS at the end of the year 2011, reached peak luminosity $\mathcal{L} = 3 \times 10^{33} \text{cm}^2 \text{s}^{-1}$ and $\mu = 20$. Figure 5.2 presents the peaked luminosity and mean number of interactions per bunch crossing as a function of days in the year 2010.

The mean number of interactions per bunch crossing plays an important role for diffractive measurements which are done using rapidity gap method. The rapidity gaps cannot be reconstructed in events with more than one interaction per bunch crossing and therefore the runs with large μ are not convenient for these measurements. Rapidity gap measurements discussed in Chapters 10 and 11 were done using the first run in 2010 where the mean number of interactions per bunch crossing was below 0.005.

5.2 ATLAS Detector

A Toroidal LHC ApparatuS (ATLAS) is the largest detector at the LHC. This general purpose detector is designed to explore new physics phenomena which are either predicted by various theoretical models or not and they could lead to rise of new theories. Moreover, ATLAS has also large potential to perform high precision measurements especially of heavy particles as W , Z or top quark and final states with large transverse momenta.

ATLAS overall length and height are about 46 m and 26 m, respectively, and it weights about 7000 tons. The layout of the detector can be seen in Figure 5.3. ATLAS is composed of Inner

Detector tracker, which is the inner most detector dedicated for reconstruction of tracks and vertices of charged particles. Superconducting solenoid magnet surrounding the inner detector with strength of 2 T enables precise measurement of transverse momenta of charged particles. Inner Detector is followed by electromagnetic and hadronic calorimeter system which is designed to measure energies of particles with very high transverse momenta. Muon chambers are outer most detectors dedicated for measurement of muons tracks and their transverse momenta. A toroidal magnets consist of barrel toroid and two end-cap toroids which create a magnetic field of magnitude 3.9 T and 4.1 T, respectively, provide large bending power for muon spectrometers.

Several forward detectors are available at the ATLAS: Minimum Bias Trigger Scintillator, LUCID, Zero Degree Calorimeter and ALFA which serve mainly for event triggering and luminosity measurement.

The coordinate system of ATLAS detector which will be used in the following text is briefly summarized here. The nominal interaction point defines origin of the coordinate system. The beam axis is identical to z -axis. Its positive and negative sides are denoted as A and C respectively. The positive x -axis points from the interaction point to the center of the LHC ring and the positive y -axis is defined as pointing upwards. The azimuthal angle, ϕ , is measured around the beam axis. The polar angle, θ , is the angle from the beam axis and the pseudorapidity is defined according to formula (4.24). Transverse momentum p_T and distance R are projections of the momentum p and the distance from the origin, respectively, to transverse plane, x - y .

The detectors which were used or can be possibly used in future for the rapidity gap analysis are discussed in more detail in this chapter. For the rest of the detectors a reader is referred to [46].

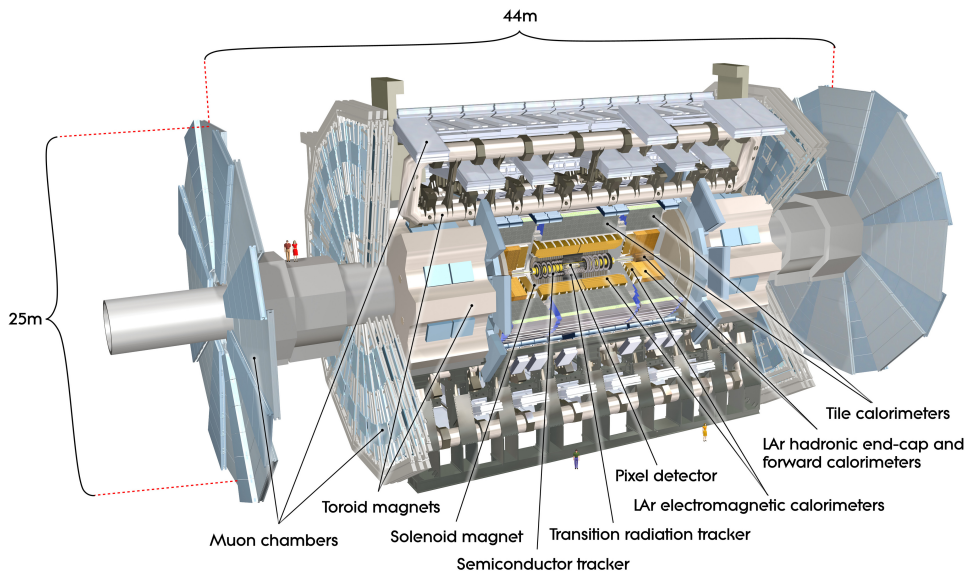


Figure 5.3: Overall view of the ATLAS detector. Figure is from [53].

5.2.1 Inner Detector

Inner Detector (ID) provides hermetic and robust pattern recognition and primary and secondary vertex measurements. It reconstructs tracks of charged particles with very high efficiency down to small transverse momenta (50 MeV) therefore it has been used for rapidity gap definition. Due to solenoidal magnetic field of strength 2 T ID gives accurate information about transverse momenta of charged particles. The detector is situated very close to the beam pipe. The most inner layer is only 50.5 mm away from the beam. The pseudorapidity acceptance of ID spans up to $|\eta| = 2.5$. The inner detector layout can be seen in Figure 5.4. The ID consists of three independent but complementary sub-detectors: Pixel Detector, Semiconductor Tracker (SCT), Transition Radiation Tracker (TRT).

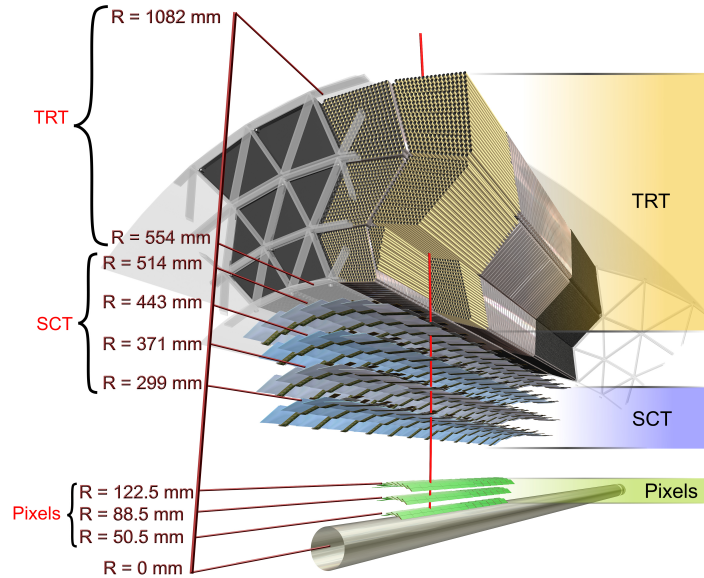


Figure 5.4: The Inner Detector consists of three subdetectors: Pixel Detectors, Silicon Tracker (SCT) and Transition Radiation Tracker (TRT). Figure is from [54].

Pixel Detector

Pixel Detector is the inner most detector with highly granular silicon sensors. It consists of three barrel and three end-cap layers. Overall, they contain 1744 pixel modules in which sensors and readout electronics are assembled. The basic readout unit pixel has size in $(R - \phi \times z)$ only $50 \times 400 \mu\text{m}^2$ providing precision of measurement to be $10 \mu\text{m}$ ($R - \phi$) and $115 \mu\text{m}$ (z) in both barrel and end-cap regions [46]. The high accuracy in all three detector coordinates is necessary especially in high multiplicity events that are produced in LHC.

Semiconductor Tracker

SCT is a silicon detector similar to pixel detector with strip sensor elements and $80 \mu\text{m}$ readout pitch. SCT has four barrel layers and four end-cap layers on both sides. Each layer is composed of modules which have two sensors to measure both coordinates. Thus SCT usually provides 4 precision points in the ϕ , z , R coordinates per track. The precision of measurement of z coordinate is smaller than precision of pixel detector.

Transition Radiation Tracker

TRT is the most outer component of the inner detector with smaller tracking precision with respect to Pixel and SCT detectors. TRT plays an important role in electron identification, cross-checking and complementing the calorimeter information, especially at energies below 25 GeV. It is composed of straw tubes with a diameter of 4 mm filled with non-flammable gas mixture and wire in the center. TRT detects the transition radiation emitted by passing high energetic particle. The different emission thresholds for electrons and particles with higher masses allow effective electron identification, especially e/π^\pm separation. The TRT can give about 36 hits on average for a passing particle. The large number of hits increases robustness and precision of the momentum measurements.

5.2.2 Calorimeter

Due to large pseudorapidity coverage, $|\eta| < 4.9$, and ability to detect both charged and neutral hadrons, ATLAS calorimeter system is well suited for rapidity gap measurements. A view of the ATLAS calorimeter system is presented in Figure 5.5. The calorimetry is composed of an electromagnetic calorimeter (EM) covering the pseudorapidity region $|\eta| < 3.2$, a hadronic barrel calorimeter (TileCal) covering $|\eta| < 1.7$, Liquid Argon (LAr) hadronic end-cap calorimeters (HEC) covering $1.5 < |\eta| < 3.2$, and forward calorimeters (FCal) covering $3.1 < |\eta| < 4.9$.

Electromagnetic Calorimeter

The EM calorimeter is divided into a barrel part ($|\eta| < 1.475$) and two end-caps ($1.375 < |\eta| < 3.2$). The barrel calorimeter has two identical half-barrels, separated by a small gap (6 mm) at $z = 0$. Each end-cap calorimeter is mechanically divided into two coaxial wheels: an outer wheel covering the region $1.375 < |\eta| < 2.5$, and an inner wheel covering the region $2.5 < |\eta| < 3.2$. The EM calorimeter is a lead-liquid argon (LAr) sampling detector. The EM has accordion-shaped geometry providing complete ϕ symmetry without azimuthal cracks. The lead absorber thickness was optimized as a function of η to achieve a good performance in energy resolution. The total thickness of the EM calorimeter is > 24 radiation lengths (X_0) in the barrel and $> 26 X_0$ in the end-caps.

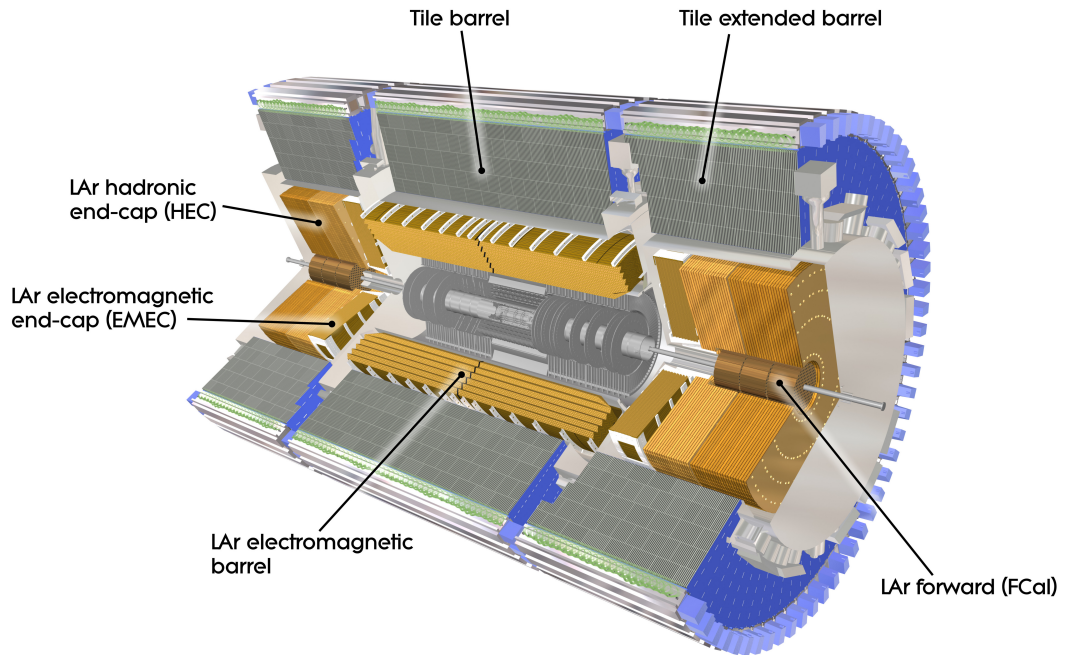


Figure 5.5: Scheme of the ATLAS calorimeter system. Figure taken from [55].

The total dead material placed in front of the calorimeter has about $2.3 X_0$ at $\eta = 0$, and increases with pseudorapidity in the barrel, see Figure 5.6. In order to correct for particle energy losses due to passing the dead material presampler is installed in pseudorapidity region $|\eta| < 1.8$.

Over the high precision measurement range $|\eta| < 2.5$ which overlaps with the inner detector acceptance, the EM calorimeter has three sampling layers in depth and high granularity. The rest of the EM calorimeter, $2.5 < |\eta| < 3.2$, has two sampling layers and a coarser lateral granularity. Overall, there are about 180000 calorimeter cells in the EM calorimeter.

The EM calorimeter performance was measured with electron test beam of energies up to 300 GeV. The energy resolution of the EM barrel at $\eta = 0.9$ was measured to be [56]

$$\frac{\sigma(E)}{E} = \frac{10\%}{\sqrt{E}} \oplus \frac{0.39\%}{E} \oplus 3\%, \quad (5.5)$$

where E denotes energy of the beam in units of GeV and $\sigma(E)$ is the standard deviation of reconstructed energy in EM. The terms on the right hand side corresponds to sampling fluctuations, electronic noise and effects due to non-homogeneity of the calorimeter.

Tile Calorimeter

Tile calorimeter is a large hadronic sampling calorimeter using iron as the absorber and scintillating tiles as the active material. The tiles are placed radially and staggered in depth. They create periodic structure along z axis. Tiles are 3 mm thick and the total thickness of the iron

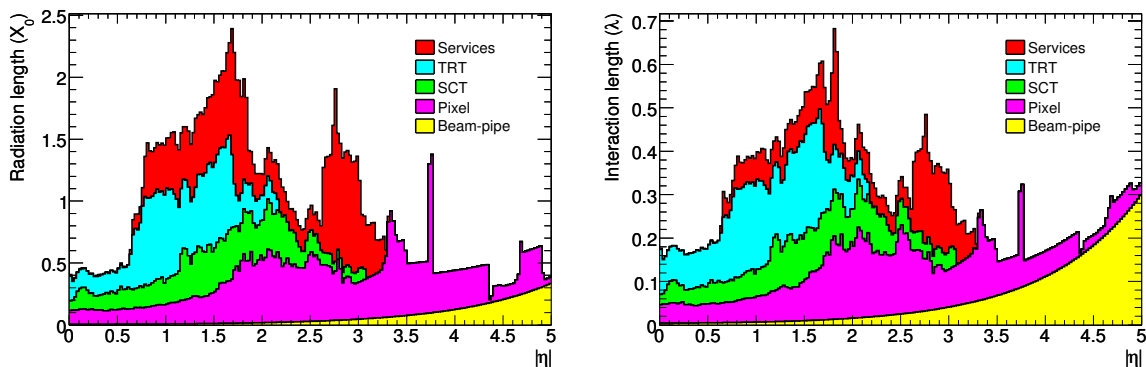


Figure 5.6: Material distribution in X_0 (left) and λ (right) at the exit of the ID envelope, including the services and thermal enclosures. The distributions are shown as a function of $|\eta|$ and averaged over ϕ . The breakdown indicates the contributions of external services and of individual sub-detectors, including services in their active volume. Figures are from [46].

plates in one period is 14 mm. The light produced from the tiles is converted into electric signal using wavelength shifting fibers followed by two separated photo-multipliers. The readout cells are pseudo-projective, in η , towards the interaction region. The granularity of TileCal is $\Delta\eta \times \Delta\Phi = 0.1 \times 0.1$ with total number of channels about 10 000.

TileCal is composed of one barrel and two extended barrels. The barrel and extended barrels are azimuthally divided into 64 modules. Radially, the TileCal is segmented into three layers with 1.5, 4.1 and 1.8 nuclear interaction lengths (λ) in barrel and 1.5, 2.6 and 3.3 λ in extended barrel. The total depth of the calorimeter system at the outer edge of the tile-instrumented region is 9.7 at $\eta = 0$.

TileCal provides energy resolution

$$\frac{\sigma(E)}{E} = \frac{52\%}{\sqrt{E}} \oplus 5\%, \quad (5.6)$$

which has been estimated from the test beam of pions with energy between 20 and 350 GeV [57].

LAr Hadronic End-Cap

HEC calorimeters are copper LAr sandwiches with parallel geometry. The LAr technology has been used in forward region due to larger radiation hardness with respect to tiles. Each of the HEC consists of two independent wheels of an outer radius 2.03 m. In addition, each wheel is divided into two longitudinal segments. In order to avoid a dip in calorimeter performance at the transition region between the hadronic end-cap and the forward calorimeter, the HEC reaches up to $|\eta| = 3.2$ to overlap with the forward calorimeter which acceptance starts at $|\eta| = 3.1$. The HEC resolution for single pions of energy from 5 to 200 GeV was measured in a test beam and

found to be [56]

$$\frac{\sigma(E)}{E} = \frac{71\%}{\sqrt{E}} \oplus 6\%. \quad (5.7)$$

Forward Calorimeter

The FCal has to cope with the high level of radiation. It is integrated into the end-cap cryostat, with a front face at about 4.7 m from the interaction point. The FCal contains both electromagnetic and hadronic parts. The first electromagnetic segment uses copper as absorber material, while the other two hadronic segments are made out of tungsten. The LAr is used as the sensitive medium due to radiation hardness. The energy resolution in the forward region is [56]

$$\frac{\sigma(E)}{E} = \frac{100\%}{\sqrt{E}} \oplus 10\%. \quad (5.8)$$

5.2.3 Minimum Bias Trigger Scintillator

The Minimum Bias Trigger Scintillator (MBTS) is a detector devoted for triggering of minimum bias interactions in first years of LHC run. The quality of the MBTS detector is gradually degraded due to the radiation damage. Two MBTS arms are located about 3.6 m from the IP in the z direction on the inner face of the end-cap calorimeter cryostat. Both arms are divided into inner and outer wheel covering a pseudorapidity regions $2.09 < |\eta| < 2.82$ and $2.82 < |\eta| < 3.84$, respectively. Each wheel is uniformly segmented in ϕ and is composed of eight counters. Due to its high efficiency to detect charged particles and forward region coverage, the MBTS detector is convenient for event selection in rapidity gap measurements of minimum bias interactions.

5.2.4 LUCID

LUCID detector (LUminosity measurement using Čerenkov Integration Detector) is installed 17 m from the ATLAS interaction point. Its main purpose is measurement of instantaneous luminosity by determining an average number of interactions per bunch crossing. This is achieved by counting the number of charged particles in the forward direction in each bunch crossing. The luminosity calibration is determined through van der Meer beam scans [59, 60].

The LUCID detector consists of two modules that are located in the available space between the beam pipe and the conical beam-pipe support structure and cover pseudorapidity in range $5.4 < |\eta| < 6.1$. As its name suggests, the detector is based on Čerenkov light detection which is emitted by charged particles passing its medium isobutane (C_4F_{10}). The photomultiplier signal output time can be measured with an accuracy of 100 ps which is by far sufficient to allow bunch-by-bunch luminosity monitoring.

It should be noted that the efficiency of detecting charged particles is rather low (about 5%) and taking into account its small coverage, the detector is not ideal for rapidity gap definition.

EM CALORIMETER	Barrel	End-cap	
Coverage	$ \eta < 1.475$	$1.375 < \eta < 3.2$	
Longitudinal segmentation	3 samplings	3 samplings	$1.5 < \eta < 2.5$
		2 samplings	$1.375 < \eta < 1.5$
			$2.5 < \eta < 3.2$
Granularity ($\Delta\eta \times \Delta\phi$)			
- Sampling 1	0.003×0.1	0.025×0.1	$1.375 < \eta < 1.5$
		0.003×0.1	$1.5 < \eta < 1.8$
		0.004×0.1	$1.8 < \eta < 2.0$
		0.006×0.1	$2.0 < \eta < 2.5$
		0.1×0.1	$2.5 < \eta < 3.2$
- Sampling 2	0.025×0.025	0.025×0.025	$1.375 < \eta < 2.5$
		0.1×0.1	$2.5 < \eta < 3.2$
- Sampling 3	0.05×0.025	0.05×0.025	$1.5 < \eta < 2.5$
PRESAMPLER	Barrel	End-cap	
Coverage	$ \eta < 1.52$	$1.5 < \eta < 1.8$	
Longitudinal segmentation	1 sampling	1 sampling	
Granularity ($\Delta\eta \times \Delta\phi$)	0.025×0.1	0.025×0.1	
HADRONIC TILE	Barrel	Extended barrel	
Coverage	$ \eta < 1.0$	$0.8 < \eta < 1.7$	
Longitudinal segmentation	3 samplings	3 samplings	
Granularity ($\Delta\eta \times \Delta\phi$)			
- Samplings 1 and 2	0.1×0.1	0.1×0.1	
- Samplings 3	0.2×0.1	0.2×0.1	
HADRONIC LAr	End-cap		
Coverage	$1.5 < \eta < 3.2$		
Longitudinal segmentation	4 sampling		
Granularity ($\Delta\eta \times \Delta\phi$)			
		0.1×0.1	$1.5 < \eta < 2.5$
		0.2×0.2	$2.5 < \eta < 3.2$
FORWARD CALORIMETER	Forward		
Coverage	$3.1 < \eta < 4.9$		
Longitudinal segmentation	3 samplings		
Granularity ($\Delta\eta \times \Delta\phi$)	$\sim 0.2 \times 0.2$		

Table 5.1: Pseudorapidity coverage, granularity and longitudinal segmentation of the ATLAS calorimeters [58].

5.2.5 Zero Degree Calorimeter

Zero Degree Calorimeter (ZDC) is a sampling calorimeter with tungsten and steel plates used as radiators and quartz strips as a sensitive medium. The calorimeter has an electromagnetic and hadronic part corresponding to approximately $29 X_0$ radiation length and 1.14λ nuclear interaction length, respectively. Two stations are placed 140 m downstream from the IP, one on each side of ATLAS. They occupy the region of a neutral particle absorber just behind the point where the beam pipe splits into two. Since charged particles are deflected outwards by beam magnetic elements, the ZDC calorimeter is sensitive primarily to neutral particles in a pseudorapidity region $|\eta| \geq 8.3$. The ZDC is dedicated for beam tuning, luminosity monitoring and triggering on minimum bias events. ZDC calorimeter could be useful especially for discrimination between different diffractive topologies (separation of SD, DD and DPE) but in first two years of the LHC runs the MC simulation of ZDC was not ready and thus it was not used for gap definition.

5.3 ATLAS Trigger

LHC produces events in rate of the order of 10^9 collisions per second, therefore it is impossible to record and store such amount of data with the current technology. Experiments have a set of hardware and software algorithms called trigger that selects the interesting rare physics processes with high efficiency and rejects much higher rate background. The decision has to be made each bunch crossing for every interaction thus the speed of the algorithms is crucial. The ATLAS strategy foresees a reduction of the event rate at three levels: LVL1, LVL2 and Event Filter (EF).

The LVL1 trigger receives data at the full LHC bunch-crossing rate of 40 MHz and needs to reduce this rate to 100 kHz. The LVL1 contains very fast hardware based algorithms with limited precision. LVL2 algorithms are software algorithms with higher accuracy. However, in order to achieve required speed only objects from the region of interest, which is a window in phase-space in which LVL1 algorithm made positive decision, are processed. The LVL2 trigger needs to be able to reduce the rate to 1 kHz. The EF algorithms work with almost the same accuracy as the offline algorithms. They use information about the whole events but they are usually seeded from LVL2 trigger. EF reduces the rate down to 100 Hz which can be recorded into a storage element.

In the first runs, the luminosity was so low that LVL1 trigger has been primarily used to select data. In the case of rapidity gap analysis, MBTS_1 trigger has been used to select events from colliding proton bunch crossings with at least single hit in MBTS. For beam-background and for study of cell noise the Random Trigger was used. This trigger selects events in empty bunches, single bunches and bunch crossing randomly with some prescale.

Chapter 6

Monte Carlo Event Generators

Monte Carlo (MC) generators are programs which attempt to generate physical events with the same probability as they occur in nature. This requires to integrate differential cross section predicted by theory but also include non-perturbative hadronisation effects and underlying events in order to describe real situation of particle state before entering a detector. Propagation of the particles through matter of the detector is then simulated using another programs as GEANT4 [61] which are also based on MC technique but they will not be discussed here. These programs enable comparison between theory and data and therefore MC generators play role of an interface between theory and experiment.

There is a vast number of MC generators dedicated for description of high energy collisions. Some of them are general purpose as PYTHIA [62], HERWIG [63], SHERPA [64] or PHOJET [65] but there are also many generators specialized for specific processes. Diffractive and exclusive processes discussed in the previous chapter are spread among many MC generators. Minimum bias models including soft diffraction can be found in PYTHIA6, PHOJET [66] and recently they have been also included into C++ version PYTHIA8 [67]. Soft diffraction description is based there on the Regge triple-pomeron approach. These three generators were used for measurements of rapidity gaps which is going to be discussed in Chapters 10 and 11.

The generators dedicated for a description of hard diffraction are POMPYT [68], based on PYTHIA6, and POMWIG [69] based on HERWIG. The QCD exclusive production has been implemented into DPEMC and later to EXHUME as was already mentioned in the previous section. The LPAIR [70] generator has been intensively used at the Tevatron for a description of two photon initiated processes. At last, it should be mentioned that many of above forward physics processes have been recently collected into FPMC [71] MC generator which extends DPEMC.

The list of the generators containing different diffractive processes is rather long and some of the generators starts to be obsolete and thus it is difficult to use them. Moreover, in last few years, the leading generators PYTHIA, HERWIG written in FORTRAN has been rewritten to new C++ versions as PYTHIA8, HERWIG++ [72] or SHERPA. These generators are now intensively

being extended to include new processes both in LO and NLO of perturbation theory, multi-jets algorithms and most importantly their models are tuned to data.

Due to the above reasons HERWIG++ has been extended for hard diffraction, QCD and QED exclusive processes which are interesting to study at the LHC. The concrete implementation will be discussed in the next Chapter 7. This section gives an overview of the basic MC integration techniques which are necessary to understand for implementation of new physics into MC generators. Furthermore, summary of particle production in perturbative partons showers and non-perturbative hadronisation phase is given together with basis of modeling underlying events and minimum bias interactions. These phenomena are closely connected with the production of rapidity gaps discussed in Chapters 10, 11.

6.1 Monte Carlo Integration

Monte Carlo is a name for a class of numerical algorithms which are based on the generation of random numbers. It is difficult to generate truly random numbers because they can be produced only by physical processes such as thermal noise or radioactive decays. Therefore in practice, a pseudo-random generators which can generate long sequences with good random properties are used. The sequence is usually determined with fixed set of numbers, called seed, which enables to repeat calculation with exactly the same random numbers sequence. Further properties of pseudo-random generators can be found in ref. [73].

One of the basic MC method is a numerical integration. An integral of function $F(x) = f(x) \cdot g(x)$ in interval $[x_1, x_2]$ where $g(x)$ is an probability density function with $\int_{x_1}^{x_2} dx g(x) = 1$ and $f(x)$ is any integrable function on the interval $[x_1, x_2]$ can be estimated as

$$I = \int_{x_1}^{x_2} dx F(x) \approx \frac{x_2 - x_1}{N} \sum_{i=1}^N f(x_i) \equiv \langle f \rangle_g, \quad (6.1)$$

where x_1, x_2, \dots, x_N are random numbers generated according to the probability distribution function $g(x)$. In the basic method, the random numbers are generated uniformly in interval $[0, 1]$ and thus $g(x) = 1$. Formula (6.1) represents an average of the function $f(x)$ at the generated points x_i and it converges to precise value I according to the Strong Law of Large Numbers. The uncertainty σ_I is given by

$$\sigma_I \approx \sqrt{\frac{x_2 - x_1}{N} [\langle f^2 \rangle_g - \langle f \rangle_g^2]}, \quad (6.2)$$

where $\langle f \rangle_g, \langle f^2 \rangle_g$ are averages of the function f and f^2 respectively defined in the sense of (6.1) and the term in the brackets is a variance of the estimator $\langle f \rangle_g$.

First, equation (6.2) shows that the speed of convergence goes as $\mathcal{O}(\sqrt{1/N})$. In the case of one dimensional function $f(x)$, the MC method is much slower than other common integration techniques as Trapezium rule $\mathcal{O}(1/N^2)$ or Simpson rule $\mathcal{O}(1/N^4)$. However, performance of these

algorithms decreases with increasing number of dimensions d as $\mathcal{O}(1/N^{\frac{k}{d}})$, where k corresponds to the speed in 1-dimension, while the convergence speed of MC integration remains the same with increasing number of dimensions d . Thus the MC integration is well suited for the integration of differential cross sections which require integration over multidimensional phase-space.

The second thing that can be read off (6.2) is a possibility of improving convergence by variance reduction. The improvement is achieved by choosing an appropriate probability distribution function $g(x)$ that smoothes the function $f(x)$. The new probability distribution function \tilde{g} that approximate function $f(x) \cdot g(x)$ can be introduced as

$$I = \int_{x_1}^{x_2} \frac{f(x)g(x)}{\tilde{g}(x)} \tilde{g}(x) dx \approx \frac{x_2 - x_1}{N} \sum_{i=1}^N \frac{f(x_i)g(x_i)}{\tilde{g}(x_i)} \quad (6.3)$$

to reduce the variance and thus enhance the convergence speed. This method is called importance sampling and in practice it can be achieved by a proper Jacobian transformation of the integral (6.1) so that the integral is flat in the new transformation variable.

In many cases we do not have the prior knowledge of the distribution in order to use an analytic transformation. For such situations there are adaptive MC methods which are able to reduce the variance automatically. These methods divide an integration area into smaller elements which size is based on the behavior of the integrand. The MC integrations are performed separately in each of these regions to yield an estimate of the integral and the variance. If the variance is too large the region is further divided into smaller partitions. One of the commonly used automatic approaches for evaluation of multidimensional integrals in MC generators is called VEGAS and its detailed description can be found in ref. [74]. It should be noted, that such automatic adaptive algorithms are never as good as analytic Jacobian transformations.

As we have seen, we need to be able to generate random variables according to various distribution functions in order to make the integration more effective. In several cases, there is an analytic method how to transform random numbers r_1, r_2, \dots, r_N which are generated according to uniform distribution $u(r)$ to sequence x_1, x_2, \dots, x_N distributed according to desired probability distribution $g(x)$. The transformation function $x(r)$ can be obtained from the comparison of cumulative distributions

$$F(x(r)) = \int_{-\infty}^{x(r)} g(x') dx' = \int_{-\infty}^x u(r') dr' = r \quad (6.4)$$

if the integral of function $g(x)$ can be inverted. This is possible only in few special cases. For the rest, a numerical algorithm called von Neumann's acceptance rejection can be alternatively used. The algorithm can be described as follows

- Generate a random number according to the distribution $w(x)$ which can be obtained by analytic transformation (6.4) and which approximates the distribution $g(x)$ with condition $w(x) \geq g(x)$.

- Random number x is accepted with a probability given by $g(x)/w(x)$.

The last point is called unweighting. The sequence of the accepted random numbers x is then distributed according the parton distribution function $g(x)$.

6.2 Event Generation

It is clear from the previous discussion that Monte Carlo integration can effectively integrate high dimensional functions with complicated boundaries. Therefore, it is well suited for evaluation of cross sections where an integral over multi-particle phase-space and incoming parton densities functions needs to be performed. Differential cross section $d\sigma(x_1, \dots, x_n)$ can be very complicated and can contain a large number of peaks. An example can be a sharp peak coming from Breit-Wiegner distribution which is frequently used in resonance decays. These peaks need to be removed by a proper Jacobian transformation as was described in the previous section. The resulted flattened cross section is integrated using an adaptive sampling method. The kinematics of produced particles in given event is generated according to the new distributions using the acceptance rejection method. In order to get events as they occur in nature an unweighting needs to be performed. The generator uses several thousands of events in order to find the maximum of differential cross section $d\sigma^{\max}$. An event is then accepted with probability $d\sigma(x_1, \dots, x_n)/d\sigma^{\max}$. The unweighting efficiency is usually estimated as the average $\langle d\sigma/d\sigma^{\max} \rangle$ and if its value is in range 0.001...0.005, the generation is considered to be effective.

This straight forward algorithm can be directly used for generation of processes at leading order of perturbation theory. However, in the next to leading order calculation it is know from KLN theorem that it is necessary to sum up the virtual and the real emissions in order to cancel out infrared divergences. For m particles in a final state this can be written as

$$\sigma^{\text{NLO}} = \int d\sigma^{\text{NLO}} = \int_m d\sigma^{\text{V}} + \int_{m+1} d\sigma^{\text{R}}. \quad (6.5)$$

In the numerical algorithm, the separate integrals cannot be evaluated and summed due to the infinities which they contain. One needs to reorganize them in such a way that each separate integral is finite. There are two general methods used for NLO matrix element integration. The older one is phase-space slicing algorithm [75] which separates problematic slice of phase-space and approximates its integrand by a constant. The second algorithm called subtraction method was introduced by Catany and Seymour [76]. The basic idea of the algorithm is existence of a function $d\sigma^{\text{A}}$ which has similar behavior as the real contribution $d\sigma^{\text{R}}$ and therefore by their subtraction we get a finite integral. On the other hand, if $d\sigma^{\text{A}}$ can be analytically integrated over one particle final state it can be added to the virtual contribution $d\sigma^{\text{V}}$ which also results into a finite integral. Since we added and subtracted the same number the overall integral remains the

same. In general MC techniques for integration of higher orders in perturbation theory are very complicated and go beyond the scope of this thesis.

6.3 Parton Showers

Parton showers represent an intermediate step between hard scattering and non-perturbative hadronisation process. In QCD, quarks and gluons radiate another partons which are predominantly soft or emitted in collinear direction. The parton showers are based on the assumption of collinear emissions same as the DGLAP equations (3.26). In the collinear approximation, the cross section for $(n + 1)$ final state partons can be written in the universal form

$$d\sigma^{(n+1)} = \sigma^{(n)} \frac{\alpha_S}{2\pi} \frac{dQ^2}{Q^2} P_{ij}(z) dz, \quad (6.6)$$

where $\sigma^{(n)}$ is a cross section for n partons in final state, $P_{ij}(z)$ are Altarelli-Parisi splitting kernels already introduced in Section 3.2 and Q^2 is virtuality of the branching parton. The parton shower can be understood as a Markov process describing a series of independent branchings which is driven by the so called Sudakov Form Factor. The Sudakov Form Factor $\Delta_i(Q^2, Q_0^2)$ expresses a probability that there is no resolvable emission during evolution of parton i from scale Q^2 to Q_0^2 and it reads

$$\Delta_i(Q^2, Q_0^2) = \exp \left[- \int_{Q_0^2}^{Q^2} \frac{dQ'^2}{Q'^2} \int \frac{dx}{x} \frac{\alpha_S(Q'^2)}{2\pi} \sum_j P_{ij}(x) \right]. \quad (6.7)$$

Using the Sudakov Form Factor the DGLAP equation can be rewritten into the integral form [7]

$$f_i(x, Q^2) = \Delta_i(Q^2, Q_0^2) f_i(x, Q_0^2) + \int_{Q_0^2}^{Q^2} \frac{dQ'^2}{Q'^2} \frac{\Delta_i(Q^2, Q_0^2)}{\Delta_i(Q'^2, Q_0^2)} \sum_j \int \frac{dz}{z} \frac{\alpha_S(Q'^2)}{2\pi} P_{ij}(z) f_j(x/z, Q'^2). \quad (6.8)$$

The first term gives the probability of having no resolvable emission during evolution from the scale Q^2 down to scale Q_0^2 . The second term corresponds to the probability that a branching $i \rightarrow ij$ occurs at a scale Q'^2 with momentum fraction z . The set of integral equation (6.8) can be solved by repeated back substitution. However in practice, MC generator generates uniformly a random number R_Q inside the interval $[0, 1]$ and solve

$$R_Q = \frac{\Delta_i(Q^2, Q_0^2)}{\Delta_i(Q'^2, Q_0^2)} \quad (6.9)$$

to determine the scale Q'^2 at which the emission occurs. This is recursively repeated for all partons until their scale Q^2 does not drop below some cut-off scale Q_{\min}^2 where the parton shower stops. The new momentum fraction, x' , carried by the emitted parton, j , is determined by equation

$$\int_{\epsilon}^{x'/x} \frac{\alpha_S(Q'^2)}{2\pi} P_{ij}(z) dz = R_x \int_{\epsilon}^{1-\epsilon} \frac{\alpha_S(Q'^2)}{2\pi} P_{ij}(z), \quad (6.10)$$

where R_x is a uniformly distributed random number at the interval $[0, 1]$. The resolution parameter ϵ is introduced in order to avoid the divergence of the splitting function corresponding to unresolved soft emission.

The above algorithm is used for a time-like evolution of final parton radiation. The numerical implementation of initial state radiation cannot directly use (6.8). It would not be possible to guarantee that the generated parton cascade will produce a parton compatible with preselected hard scattering. This problem can be solved by backward evolution scheme in which partons entering to the hard scattering are evolved back to low-scale hadrons by taking into account PDFs that specifies the hard process. To do this, the Sudakov Form Factor $\Delta_i(Q^2, Q_0^2)$ needs to be replaced by

$$\Pi_i(Q^2, Q_0^2; x) = \Delta_i(Q^2, Q_0^2) \frac{f_i(x, Q_0^2)}{f_i(x, Q^2)}, \quad (6.11)$$

which corresponds to probability of evolving parton, i , backward from the scale Q^2 and momentum fraction x to the scale $Q_0^2 < Q^2$ with unchanged momentum fraction x and without any resolvable emission. To see this, let $dF_i(Q^2, Q_0^2; x)$ denote the fraction of partons of flavour i having virtuality Q^2 and momentum fraction x and coming from a resolvable branching in the interval $[Q^2, Q^2 + dQ^2]$. Then $\Pi_i(Q^2, Q_0^2; x)$ can be expressed as

$$\begin{aligned} \Pi_i(Q^2, Q_0^2; x) &= 1 - \int_{Q_0^2}^{Q^2} dF_i(Q^2, Q_0^2; x) = \\ &= 1 - \int_{Q_0^2}^{Q^2} dQ'^2 \frac{1}{f_i(x, Q^2)} \sum_j \int \frac{dz}{z} \Delta(Q'^2, Q^2) \frac{\alpha_S(Q'^2)}{2\pi} P_{ij}(z) f_j(x/z, Q'^2) = \\ &= 1 - \frac{1}{f_i(x, Q^2)} \int_{Q_0^2}^{Q^2} dQ'^2 \frac{\partial}{\partial Q'^2} \left[\frac{f_i(x, Q'^2)}{\Delta(Q'^2, Q^2)} \right], \end{aligned} \quad (6.12)$$

where the third equality uses the fact that $\Delta(Q^2, Q'^2) = \Delta^{-1}(Q'^2, Q^2)$. Generation of branching at scale Q'^2 is then implemented in the same manner as in the case of the forward evolution

$$R_Q = \Pi_i(Q^2, Q'^2; x), \quad (6.13)$$

where R_Q is a uniform random number generated in interval $[0, 1]$. To estimate the momentum fraction x' , the (6.12) have to be multiplied by extra factor of $f(x', Q'^2)$ that will be divided out in the next backward step in Q^2 . Thus $z = x/x'$ needs to be generated according to the probability distribution

$$\frac{\alpha_S(Q'^2)}{2\pi} \frac{P_{ij}(z)}{z} f(x/z). \quad (6.14)$$

All the previous treatments of parton showers were derived in the collinear approximation. In the case of soft gluon radiation, which is also enhanced in the multi-parton cross section, universality as (6.6) holds only at the level of amplitudes i.e. the cross section for emission of extra soft gluon contains an interference between more Feynman diagrams. However, in order to formulate an algorithm for MC generator, the emission of the soft gluon needs to be

associated with a particular parton. As already mentioned in Section 3.2, the DGLAP equation requires strongly ordered virtualities in order to resum leading logarithms but one can redefine the DGLAP equation in term of different 'equivalent' ordering variable. It has been shown that coherent soft gluon effects can be taken into account if we choose the ordering variable of parton shower to be an opening angle between two partons. This is known as angular ordering of the parton showers.

The angular ordering parton showers are implemented in the most frequently used generators PYTHIA and HERWIG. It is worth noting that there is a complementary approach which solves the problem of soft enhancement in terms of dual dipole cascade. The model is based on observation that colour dipole e.g. $q\bar{q}$ pair radiates a gluon in analogy with electromagnetism. The colour dipole model is implemented in MC program ARIADNE [77].

6.4 Hadronisation Models

The parton shower produces perturbatively parton cascade with final partons of scale down to a fixed cut-off $Q_0 \approx 1 \text{ GeV}$. Due to such low scale the QCD coupling is large and pQCD cannot be further used. In order to describe transition of partons into final stable hadrons which can be experimentally observed phenomenological hadronisation models have to be employed. Three basic hadronisation models are discussed in this chapter: independent fragmentation which does not take into account colour connection and is less successful as other two models, string fragmentation implemented in PYTHIA for which colour connection is essential, and its alternative, the cluster hadronisation used in HERWIG.

6.4.1 Independent Fragmentation

The first hadronisation model which has been introduced by Field and Feynman [78] is known as the independent fragmentation. The model assumes that each parton fragments independently. The fragmenting quark is combined with an anti-quark from $q\bar{q}$ pair, created from the vacuum, to produce a meson which carries momentum fraction z of the original quark. The leftover quark with momentum fraction $(1 - z)$ then fragments in the same way. The procedure is repeated until the left energy drops below some cut-off. The momentum fraction is determined according to the fragmentation function $D_q^h(z, p_T)$ which expresses the probability that quark q fragments into hadron h that carries a momentum fraction z of the original quark and transverse momentum p_T . The fragmentation function cannot be derived from the first principles and has to be measured. Independent fragmentation treats gluon as $q\bar{q}$ pair in which gluon momentum is distributed between quark and anti-quark either according to Altarelli-Parisi splitting function $P_{qg}(z)$ or quark carries whole gluon momentum and anti-quark zero momentum or other way around. Although the model was quite successful in describing multi-jet events at LEP it suffers

by several weaknesses such as violation of momentum and flavour conservation and infrared safety. Therefore nowadays the independent fragmentation is rarely used.

6.4.2 String Hadronisation

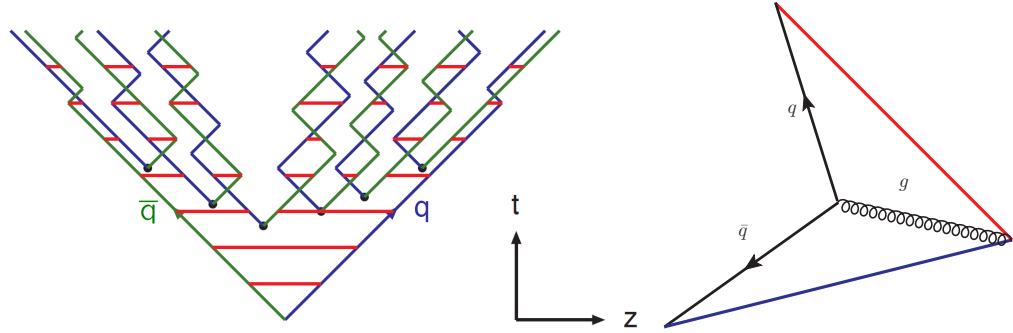


Figure 6.1: a) String evolution initiated by $q\bar{q}$ pair. b) Gluons are treated as kinks that carries energy and momentum on the string.

String hadronisation model has practically similar algorithm to fragment $q\bar{q}$ pairs into mesons as independent fragmentation. The model is based on the idea that when quarks in $q\bar{q}$ pair are moving apart, a colour field between the q and \bar{q} collapses into a narrow flux tube of uniform energy density per unit length. The field is approximated by a linear potential created by a string with tension $\kappa \approx 1 \text{ GeV/fm}$. Thus $q\bar{q}$ pair oscillates outwards and inwards passing through one another and transferring energy to and from the string what is termed as yo-yo mode. If the kinetic energy of the initial $q_0\bar{q}_0$ pair is large enough the string breaks up and creates another $q_1\bar{q}_1$ pair. The q_0 can join the \bar{q}_1 to create a meson leaving the q_1 unpaired. The $q_1\bar{q}_0$ can again produce new $q_2\bar{q}_2$ pair in the same manner and the creation of mesons iteratively continues until there is no energy left. The space time picture of the string evolution can be seen in Figure 6.1. The probability of breaking up the string and creating a $q\bar{q}$ pair is given by Wilson's exponential area decay law which takes the form

$$\frac{dP}{dA} = P_0 \exp(-P_0 A), \quad (6.15)$$

where A is the space-time area within the backward light-cone of the point at which the new $q\bar{q}$ is created and P_0 is a constant reflecting uniformness of the string.

In practice, the model is described in transverse mass $m_T = \sqrt{m^2 + p_T^2}$ and light-cone momentum fraction z of the fragment. First, the algorithm selects flavour of the $q_i\bar{q}_i$ pair according to some probabilities. If the $q_i\bar{q}_i$ have no transverse mass, the pair is classically created at one point and it is propagated in the field. However, if the pair has a transverse mass the quarks in the pair would have to be produced in some distance that the field between them can be transformed into the transverse mass. The Lund model invents a concept of quantum

mechanical tunneling i.e. the pair is created at one point and tunnels to classically allowed region with probability

$$\exp\left(-\frac{\pi m_{\text{T}}^2}{\kappa}\right) = \exp\left(-\frac{\pi m^2}{\kappa}\right) \exp\left(-\frac{\pi p_{\text{T}}^2}{\kappa}\right). \quad (6.16)$$

This leads to a flavour independent p_{T} component which is generated according to Gaussian distribution. Since the string has initially no transverse momentum the p_{T} is compensated between $q_i \bar{q}_i$. Having the transverse momentum generated we need to determine the energy of mesons and longitudinal momentum z . Since the hadrons are required to be on-shell it is enough to generate only momentum fraction z . This is usually generated according to a fragmentation function $f_{ij}(z)$ describing the probability that a quark with flavour i combines with an anti-quark with flavour j to give a meson with remaining fractional momentum of the system z . It should be noted that there is a freedom from which side of the string the hadronisation proceeds. The requirement of the independence of such choice, called left-right symmetry, uniquely determines the fragmentation function to be

$$f_{ij}(z) \propto \frac{1}{z} z^{a_i} \left(\frac{1-z}{z}\right)^{a_j} \exp\left(-b \frac{m_{\text{T}}^2}{z}\right). \quad (6.17)$$

The string model becomes more distinct from independent fragmentation when the gluons are added into the game. The gluons produce energy and momentum carrying kinks on each string. As an example, a $q\bar{q}g$ event in which the string is stretched from the q via g to \bar{q} can be seen in Figure 6.1. Since the gluon is attached to two strings, the force acting on the gluon has double magnitude compared to the force acting on individual quarks. It has been shown in QCD that the ratio between the force on gluon and on quark is $2/(1 - 1/N_c^2)$ thus the string model has effectively infinitely many colours. The fragmentation of kinked strings leads to a better agreement with experiment than independent fragmentation in angular distribution of hadrons in e^+e^- three-jet final state.

So far we have discussed the production mechanism of mesons only. The generalization of the mesons production into baryons is not unique and three different mechanisms are available in PYTHIA. The simplest scenario assumes that any flavour q_i can represent a quark or a di-quark $q_i q_i$ in a colour triplet state. The baryons are then produced by combination of nearest quark or di-quark pairs in a similar way to meson production. More general frameworks for baryon production are simple popcorn and advanced popcorn models where baryons are produced from several $q\bar{q}$ pairs between which one or several mesons are formed from intermediate $q\bar{q}$ pairs. A schematic diagram for baryon production in these models can be seen in Figure 6.2.

It should be emphasized that Lund String hadronisation solves the weaknesses of the independent fragmentation, such as momentum and flavour violations, infrared and collinear safety. Its sometimes criticized feature is a large set of free parameters, especially related to the flavour properties, that needs to be tuned to data. On the other hand, the Lund String hadronisation model gives in general the most successful description of experimental data.



Figure 6.2: A schematic diagram of baryon production taken from ref. [79]. Diquark model (left) which produces $B\bar{B}$ as nearest neighbours and popcorn model (right) allowing configuration $BM\bar{B}$, where B and M denotes baryon and meson respectively. The lines show flavour correlation.

6.4.3 Cluster Hadronisation

The cluster hadronisation models are based on preconfinement property derived in pQCD [80]. Preconfinement states that at the end of the parton shower the mass and spatial distributions of colour singlet combinations of partons (clusters) are universal i.e. they depend only on the cut-off scale of the parton shower Q_0 and QCD parameter Λ_{QCD} but not on the scale or nature of the hard process. The preconfinement also implies that the mass distribution of clusters rapidly falls at high masses. Typical cluster mass distribution for different scales of hard process Q^2 generated in HERWIG is presented in Figure 6.3.

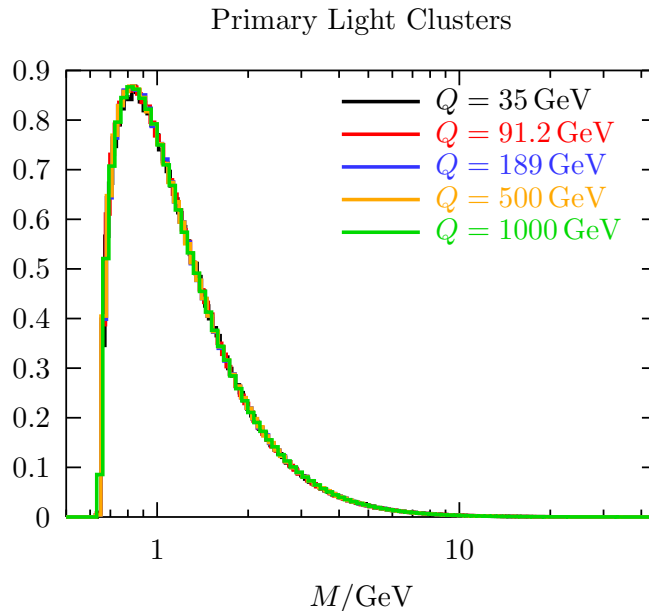


Figure 6.3: Invariant mass distribution of colour singlet of clusters simulated in HERWIG, taken from ref. [81]. The spectrum does not depend on the scale of the hard process Q and rapidly falls in large masses.

The simplest way how to form a colour singlet cluster is to non-perturbatively split the gluons

produced by the parton shower into $q\bar{q}$ pairs. Neighbours $q\bar{q}$ can be then combined into colour singlets with the momentum given by the sum of the momenta of the constituent quarks. This approach creates the basis of hadronisation model used in HERWIG. Since the cluster mass spectrum is both universal and peaks at low masses, the clusters are considered as highly excited hadron resonances which decay into hadrons. If the cluster is too heavy, that can happen in a small fraction of cases, it needs to be split into lighter clusters before it can be decayed to hadrons. The cluster fissions into two cluster if its mass M satisfies

$$M^{Cl_{\text{pow}}} \leq Cl_{\text{max}} + (m_1 + m_2)^{Cl_{\text{pow}}}, \quad (6.18)$$

where Cl_{max} , Cl_{pow} are parameters of the model and m_1 , m_2 are masses of parton constituents of the cluster. The fission continues until clusters do not reach required masses for decay into hadrons. For a cluster of a given flavour¹ (q_1, \bar{q}_2) a quark-antiquark or diquark-antidiquark pair (q, \bar{q}) is extracted from the vacuum and a pair of hadrons with flavours (q_1, \bar{q}) and (q, \bar{q}_2) is formed. For the production of hadrons $a_{(q_1, \bar{q})}$ and $b_{(q, \bar{q}_2)}$ the weight W is estimated as

$$W(a_{(q_1, \bar{q})}, b_{(q, \bar{q}_2)}) = P_q w_a s_a w_b s_b p_{ab}, \quad (6.19)$$

where P_q is the weight for production $q_1\bar{q}_2$ pair with given flavour, w_a and w_b are weights for production of hadrons a and b , s_a and s_b are suppression factors for given hadrons and p_{ab} is the phase-space available for their production. There are different approaches that vary in implementation of the cluster decay products selection. The original approach in [82] has been improved by model [83] which cures the issue of low rate baryon production.

HERWIG++ extends the described cluster hadronisation model by possibility of colour reconnection [84]. This occurs at the stage where clusters are formed from the parton-shower products. Algorithm allows to reshuffle colour cluster constituents between two cluster pairs. It looks for cluster pairs where reconnection would result in the smallest sum of cluster masses and performs a reconnection according to a reconnection probability parameter. The introduction of colour reconnection led to a great improvement in the description of charge particle distributions measured by ATLAS collaboration [1, 85].

The cluster model in combination with angular-ordered parton showers gives a fairly good overall description of high-energy collider data, usually slightly less good than the string model, but involving fewer parameters.

6.5 Underlying Events and Minimum Bias Simulation

When two hadrons pass through each other there is a change that more than one parton-parton interaction occurs. The probability grows with increasing center-of-mass energy, \sqrt{s} , of colliding

¹Information about flavour of cluster constituents is propagated through the cluster fission procedure, see [81] for further details.

hadrons thus the effect at LHC energies is important. Most of the parton-parton collisions lead to production of soft particles and thus create a 'pedestal' to hard process of our primary interest which occurs much less likely than the soft process. In order to perform precise measurement of the hard processes it is necessary to understand the underlying production and be able to model it in MC programs.

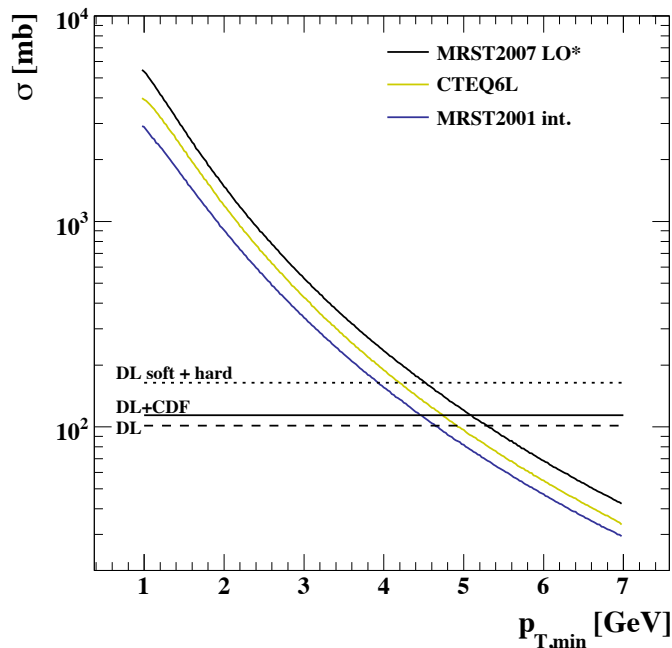


Figure 6.4: The inclusive hard cross section for three different proton PDFs, compared to various extrapolations of the non-perturbative fits to the total pp cross section at 14 TeV center-of-mass energy. Plot taken from ref. [86].

The idea of multi-parton interactions is based on an observation that a cross section of hard parton-parton scattering per one hadron-hadron collision as a function of minimum transverse momentum p_T^{\min} exceeds the total cross section at sufficiently small p_T^{\min}

$$\sigma^{\text{hard}}(p_T^{\min}) = \int_{p_T^{\min}}^{\sqrt{s}/4} dp_T \frac{d\sigma}{dp_T} > \sigma_{pp}^{\text{tot}}. \quad (6.20)$$

The example of the predicted dependence $\sigma^{\text{hard}}(p_T^{\min})$ on the p_T^{\min} for LHC at $\sqrt{s} = 14$ TeV can be seen in Figure 6.4. The $\sigma^{\text{hard}}(p_T^{\min})$ exceeds the total inelastic cross section estimated by Donnachie-Landshoff at $p_T \simeq 5$ GeV. In order to interpret this behavior one needs to realize that the σ^{tot} expresses inclusive number i.e. if n parton interactions with $p > p_T^{\min}$ occur during one pp collision this needs to be counted as one event for σ^{tot} but as n events in $\sigma^{\text{hard}}(p_T^{\min})$. In fact, one needs to deal with a divergence of the number of interactions per one hadron collision as $p_T^{\min} \rightarrow 0$ which is due to rapidly increasing parton distribution functions at small x .

The divergence is suppressed by employing correlation due to momentum conservation. This is approached differently in PYTHIA and HERWIG. While PYTHIA orders the multiple interactions in Bjorken variable x and ensures that the sum of momentum fraction x over all interactions does not exceed unity, HERWIG++ estimates the number of interactions n as a first guess but generates only so many interactions so that the energy conservation is not violated.

The residual divergence for $p_T^{\min} \rightarrow 0$ in the non-perturbative region can be understood in following way. If a gluon with a sufficiently small transverse momentum is emitted from the hadron it cannot resolve the individual colour charges and thus its effective coupling decreases. This is expected to happen at least at

$$p_T^{\min} \simeq \frac{\hbar}{r_p} \approx \frac{0.2 \text{ GeV} \cdot \text{fm}}{0.7 \text{ fm}} \approx 0.3 \text{ GeV} \simeq \Lambda_{\text{QCD}} \quad (6.21)$$

but the typical value where MC generators starts to regulate is $p_T^{\min} \approx 2 \text{ GeV}$. The most simple regularization is a sharp cut-off, however, HERWIG++ and PYTHIA8 use more smooth regularization scenarios. HERWIG++ generates soft scatters below the cut p_T^{\min} , where the cross section for soft scatters is estimated as the difference of the non-diffractive cross section determined from Donnachie-Landshoff model and the cross section for semi-hard scattering. PYTHIA8 uses the fact that the cross section diverges as $\alpha_S^2(p_T^2)/p_T^4$ and it can be smoothly regularized by factor

$$\frac{\alpha_S^2(p_T^2 + p_{T0}^2)}{\alpha_S^2(p_T^2)} \frac{p_T^4}{(p_T^4 + p_{T0}^4)}, \quad (6.22)$$

where p_{T0} is a free parameter which needs to be tuned to data.

The multi parton interactions in PYTHIA and HERWIG are based on assumptions that the scatterings between partons are independent. Hence, the number of semi-hard (soft) interactions per hadron-hadron collision is estimated using Poisson distribution

$$P_n(b, s) = \frac{\langle n(b, s) \rangle^n}{n!} e^{-\langle n(b, s) \rangle}. \quad (6.23)$$

It is reasonable to assume that the average number of scatters $\langle n(b, s) \rangle$ depends on the impact parameter b of hadron-hadron collision because there is larger chance that more scatters occur during the head on collision than during the peripheral collision with large impact parameter b . In order to quantify the hadronic matter overlap in pp collision, one assumes symmetric spatial distribution of the matter inside hadrons, $\rho(\vec{x})d\vec{x} = \rho(r)d\vec{x}$. In PYTHIA, $\rho(r)$ is approximated by a (double) Gaussian, exponential distributions or some distributions interpolating between these, where as HERWIG++ uses electromagnetic form factors [87]. The time integrated overlap function between the matter distributions of the colliding hadrons is given by

$$A(b) \propto \int dt \int d^3\vec{x} \rho(x, y, z) \rho(x + b, y, z + t). \quad (6.24)$$

The relation between the mean value of scatters and overlap function has simply linear form $\langle n(b, s) \rangle = f(s)A(b)$, where $f(s)$ is proportional to parton-parton cross section.

It should be noted that, in order to obtain finite total cross sections, PYTHIA model requires that each event contains at least one semi-hard interaction, while HERWIG does not. There are further slight differences between the models in PYTHIA and HERWIG. It is worth to mention that PYTHIA implements the possibility of perturbative rescattering which takes place during partonic showering of the multiple semi-hard scattering products. This leads to slight increase in the mean p_T of the partonic final states, but more dramatic signatures have not been identified yet.

Minimum bias in PYTHIA8 and HERWIG++ is simulated in similar way. As already mentioned, the total cross section is computed using Donnachie-Landshoff model [11]. The particles are produced according to QCD $2 \rightarrow 2$ in semi-hard processes with $p_T > p_T^{\min}$ for PYTHIA8 while HERWIG++ uses special matrix element dedicated for minimum bias simulation which enhances the production of soft p_T final states. Both generators have special treatment of soft particle production i.e. below p_T^{\min} . The minimum bias model in PYTHIA contains diffractive production which is not included in HERWIG++ yet.

6.6 Modeling of Inclusive Diffraction in MC Generators

The current MC generators use models based on the triple pomeron approach introduced in Section 4.2. The models mainly differ in the t dependence, the parameterization of pomeron trajectory $\alpha_{\mathbb{P}}(t) = \alpha_{\mathbb{P}}(0) + \alpha'_{\mathbb{P}} t$, and modeling of high p_T production. In PYTHIA, cross section is by default parameterized by Schuler and Sjöstrand model in which $\alpha_{\mathbb{P}}(0) = 1$ and exponential t dependence $\exp(-B(\xi_X, \xi_Y)t)$. There are three other alternatives available. The Bruni and Ingelman [88] is similar to Schuler and Sjöstrand [89], except that its t dependence is given by the sum of two exponentials. In the Berger and Streng [90,91] and Donnachie and Landshoff [92] models the default pomeron trajectory is $\alpha_{\mathbb{P}}(t) = 1.085 + 0.25t$, consistent with results from fits to total and elastic hadronic cross section data [11]. Whilst the model attributed to Berger and Streng has an exponential t dependence, the Donnachie and Landshoff version is based on a dipole model of the proton elastic form factor. For all flux parameterizations in PYTHIA, additional factors are applied to modify the distributions in kinematic regions in which a triple-pomeron approach is known to be inappropriate. Their main effects are to enhance the low mass components of the dissociation spectra, to suppress the production of very large masses and, in the DD case, to reduce the probability of the systems X and Y overlapping in rapidity space. The treatment of particle production in PYTHIA6 depends on the diffractive mass M . For $M \leq 1$ GeV, the system is allowed to decay isotropically into a two-body system. In the case of larger masses, the system is treated as a string with quantum number of the original proton. This leads to production of final state hadrons distributed in a longitudinal phase-space with limited transverse momenta. PYTHIA8 uses similar mechanism for particle production with diffractive masses below 10 GeV. However, for larger masses there is a smooth transition to perturbative

description based on the Ingelman-Schlein model. The model consider pomeron to be composite object whose content is described by the diffractive PDF as it was discussed in Section 4.3. This approach yields a significantly harder final state particle transverse momentum spectrum in SD and DD processes in PYTHIA8 compared with PYTHIA6.

Cross section at $\sqrt{s} = 7 \text{ TeV}$			
Process	PYTHIA6	PYTHIA8	PHOJET
σ_{ND} (mb)	48.5	50.9	61.6
σ_{SD} (mb)	13.7	12.4	10.7
σ_{DD} (mb)	9.2	8.1	3.9
σ_{CD} (mb)	0.0	0.0	1.3
Default f_{ND} (%)	67.9	71.3	79.4
Default f_{SD} (%)	19.2	17.3	13.8
Default f_{DD} (%)	12.9	11.4	5.1
Default f_{CD} (%)	0.0	0.0	1.7
Tuned f_{ND} (%)	70.0	70.2	70.2
Tuned f_{SD} (%)	20.7	20.6	16.1
Tuned f_{DD} (%)	9.3	9.2	11.2
Tuned f_{CD} (%)	0.0	0.0	2.5

Table 6.1: Cross sections and relative fractions predicted by the MC generators for collisions $\sqrt{s} = 7 \text{ TeV}$ and used in ATLAS AMBT1 tune for PYTHIA6. Tuned overall diffractive fraction used in 4C and AMBT2B tunes which has been measured at the ATLAS [3] with total inelastic cross section fixed.

The PHOJET model uses the two component dual parton model [93] to combine features of Regge phenomenology with AGK cutting rules [94] and leading order QCD. Diffractive dissociation is described in a two-channel eikonal model, combining a triple Regge approach to soft processes with the lowest order QCD for processes with parton scattering transverse momenta above 3 GeV. The pomeron intercept is taken to be $\alpha_{\text{p}}(0) = 1.08$ and for hard diffraction, the diffractive parton densities are taken from [95,96]. Hadronisation follows the Lund String model, as for PYTHIA. PHOJET is the only generator that implements central diffractive production contributing by 1.7% into the total inelastic cross section. The version used for rapidity gap analysis is PHOJET1.12.1.35, with fragmentation and hadronisation as in PYTHIA6.1.15.

The specific versions used in rapidity gap analysis are PYTHIA6.4.21 (with the AMBT1 tune performed by ATLAS) and PYTHIA8.145 (with the 4C tune). Updated versions, PYTHIA8.150 and PYTHIA6.4.25 (using the 4C and AMBT2B tunes, respectively), are used for comparisons with the corrected data, see Table 6.1. The 4C tune of PYTHIA8 takes into account the measurement

of the diffractive fraction f_D of the inelastic cross section in [3], whilst keeping the total cross section fixed, resulting in a somewhat smaller diffractive cross section than in PYTHIA6. The measurement of diffractive fraction in total inelastic cross section will be discussed in detail in Chapter 10.

Chapter 7

Forward Processes in Herwig++

HERWIG++ generator has been extended for some of the forward physics processes which are particularly interesting for LHC measurement. These are diffractive production of 'hard' objects, QCD exclusive production and two photon initiated processes. Some of the processes with large yields have been already studied using rapidity gap methods at the LHC but for the rare processes, in which a new physics can be probed, the very forward detectors for proton tagging need to be used for pile-up and background separation. ATLAS experiment recently approved a project ATLAS Forward Physics (AFP) [97] aiming to install proton taggers at 220 m from the interaction point. The silicon tracking detectors together with fast timing detectors placed in movable beam pipe allowing to approach the detectors very close to the beam will provide measurement of high mass exclusive and diffractive objects even at high instantaneous luminosities.

HERWIG++ is a new C++ MC generator providing vast number of processes both in LO and NLO accuracy. HERWIG++ is based on THEPEG (the Toolkit for High Energy Physics Event Generation) [98] framework for implementing MC event generators. THEPEG provides an code infrastructure as a collection of modular building blocks that is independent of physics models. HERWIG++ implements a specific physics models on the top of the framework. The framework enables an easy extension for various models and new processes but also comfortable user setup interface. Hard diffraction, QED and QCD exclusive production have been implemented to HERWIG++ as a part of the work for this thesis. The hard diffraction and two photon initiated processes were added to HERWIG++ release v2.5 [84]. This chapter is devoted to detailed description of the processes which have been implemented so far and to outlook for further developments. First, the implementation of photon initiated processes is discussed, then details of hard diffractive model are reviewed. Finally, the QCD central exclusive production framework in HERWIG++ with the already added processes is summarized.

7.1 Photon Initiated Processes

As it was already mentioned, QED exclusive production mechanism schematically illustrated in Figure 4.9 is described by Equivalent Photon Approximation (EPA) first invented by Weizsäcker-Williams [99, 100] for description of low virtuality photon emission by electron. Later the approximation was extended by Budnev [41] for photon radiation from hadrons. We use EPA to describe a probability $f(x, Q^2)$ that almost real photon with virtuality $[Q^2, Q^2 + dQ^2]$ is emitted off proton and carries proton momentum fraction $[x, x + dx]$ given by

$$f(x, Q^2) = \frac{\alpha}{\pi} \frac{dx}{x} \frac{dQ^2}{Q^2} \left[(1-x) \left(1 - \frac{Q_{\min}^2}{Q^2} \right) F_E + \frac{x^2}{2} F_M \right], \quad (7.1)$$

where $Q_{\min}^2 = m_p^2 x^2 / (1-x)$ is the minimum photon virtuality allowed by kinematics in which m_p is proton mass. The electric and magnetic form factors F_E and F_M are rapidly falling functions of the form

$$F_M = G_M^2 \quad (7.2)$$

$$F_E = (4m_p^2 G_E^2 + Q^2 G_M^2) / (4m_p^2 + Q^2) \quad (7.3)$$

$$G_E^2 = G_M^2 / \mu_p^2 = (1 + Q^2 / Q_0^2)^{-4}, \quad (7.4)$$

with proton magnetic moment $\mu_p = 7.78$ and fitted scale $Q_0^2 = 0.71 \text{ GeV}^2$. HERWIG++ treats the $f(x, Q^2)$ as a parton distribution function allowing to combine with different PDF to generate processes such as photoproduction or photon-pomeron interactions. The processes currently available for two photon initiated processes are two lepton production, di-jet production and WW in SM.

p_T [GeV]	HERWIG++ [pb]	FPMC [pb]	LPAIR [pb]
3	47.24	49.42	47.66
5	13.18	13.54	13.24
10	2.203	2.223	2.182
30	1.094×10^{-1}	1.097×10^{-1}	1.110×10^{-1}
50	2.486×10^{-2}	2.494×10^{-2}	2.466×10^{-2}

Table 7.1: Cross sections for di-muon production in two photon initiated processes in collisions with $\sqrt{s} = 14 \text{ TeV}$. All generators predictions are in good agreement.

The HERWIG++ implementation was tested with di-muon production $pp \rightarrow p \oplus \mu\mu \oplus p$ and comparison was made with FPMC and LPAIR generators at $\sqrt{s} = 14 \text{ TeV}$. A good agreement is achieved in cross sections for different cuts on transverse momentum of produced μ between the MCs. This can be seen from Table 7.1. Relevant distributions are compared in Figure 7.1. A disagreement between FPMC and HERWIG++ and also LPAIR is seen in the outgoing proton

transverse momentum distribution which is proportional to photon virtuality, $p_T^{\text{proton}} \sim -Q$. The discrepancy can be explained by the fact that the spin correlation between leptons and protons is taken into account in LPAIR and HERWIG++ but not in FPMC [101]. Lepton rapidity distribution exhibit small disagreement between HERWIG++ and LPAIR with FPMC for large rapidities $|y| > 4$. This deviation is attributed to implementation details of particular MC generators. Particularly, kinematical cuts can be applied in different frames (laboratory frame or center-of-mass of hard process) what is responsible for slight discrepancy at the very beginning of lepton p_T distribution in Figure 7.1. In the other distributions, the MCs are in good agreement.

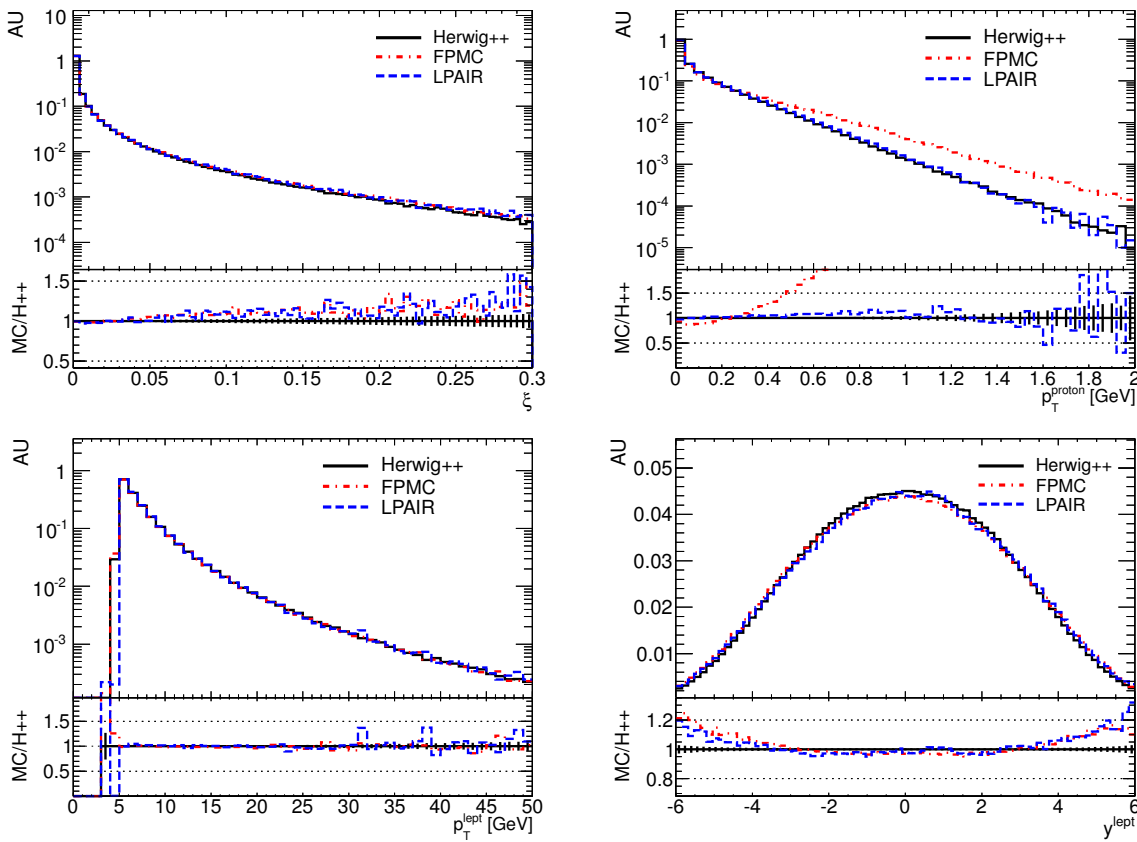


Figure 7.1: Comparison of exclusive muon production at $\sqrt{s} = 14$ TeV in HERWIG++, LPAIR and FPMC. The figure presents distributions of proton momentum fraction loss, transverse momentum of outgoing photon, rapidity of outgoing muons and transverse momentum of outgoing muons.

7.2 Hard Diffractive Processes

For description of diffractive processes in which a high mass object is produced HERWIG++ contains Ingelman-Schlein [20] model introduced in Section 4.3. The cross section in pp collision

is described by convolution of diffractive PDF (DPDF) and a cross section of a hard process (4.30). The DPDF can be further factorized (4.30) into pomeron flux which is motivated by Regge theory (4.32) and pomeron distribution function measured at HERA. HERWIG++ offers three NLO DPDF provided by H1 collaboration in year 2006 [102] (fits A and B) and 2007 [21]. The DPDF fits determine all free parameters in pomeron flux and HERWIG++ sets them as default allowing a user to change it. The reggeon contribution which is small for high mass production can also be included or generated separately. In case of reggeon contribution no reggeon PDF exists but it is a custom practice to use a pion distribution functions which successfully describe H1 data. Thus HERWIG++ provides class which is only an interface to LHAPDF library [103]. In order to treat the pomeron or reggeon remnant correctly their parton content needs to be set. Since both experiment and theory suggest that the pomeron is composed of gluons HERWIG++ uses this as default option. Gluonic content of the pomeron leads to larger particle production with respect to the option where pomeron is composed of $q\bar{q}$. Reggeon is treated as $q\bar{q}$ pair only, in order to be consistent with pion PDF. As it was already discussed in Section 4.3, the factorization (4.30) is broken down in pp collisions and the cross section needs to be scaled by the corresponding survival probability factor. This suppression factor is not included in HERWIG++ therefore the resulted cross section has to be scaled by corresponding factor by user.

Single diffractive and double pomeron exchange production of many SM processes as well as some MSSM processes are available in HERWIG++. Moreover, few NLO processes with POWHEG mechanism [104] for merging NLO hard process with parton shower listed in can be used. Diffractive production in HERWIG++ was validated against POMWIG which is actually

p_T [GeV]	POMWIG 2006 A [μb]	HERWIG++ 2006 A [μb]	HERWIG++ 2006 B [μb]	HERWIG++ 2007 [μb]
10	95.63	96.33	98.69	92.51
30	1.546	1.554	1.435	1.357
50	1.886×10^{-1}	1.901×10^{-1}	1.659×10^{-1}	1.537×10^{-1}

Table 7.2: Cross sections for di-jet production in DPE at $\sqrt{s} = 14 \text{ TeV}$ for various DPDF fits.

the most frequently used generator for hard inclusive diffraction and contains the same model as HERWIG++. The cross sections for DPE di-jet at $\sqrt{s} = 14 \text{ TeV}$ production for different p_T cuts are summarized in Table 7.2. All the three diffractive PDF fits 2006 A, 2006 B and 2007 in HERWIG++ are compared with 2006 A in POMWIG. The cross sections well agrees between POMWIG and HERWIG++ for the same fit 2006 A. The choice of the PDF fit has effect of $\sim 5\%$. The relevant distributions on the parton level for DPE di-jet production with $p_T^{\text{cut}} = 10 \text{ GeV}$ can be seen in Figure 7.2. Again, HERWIG++ and POMWIG, with the same 2006 A fit, well agree for all distributions. Some small discrepancies can be seen at the beginning of the p_T and mass distributions and at the tails of rapidity distribution of the outgoing partons. These are

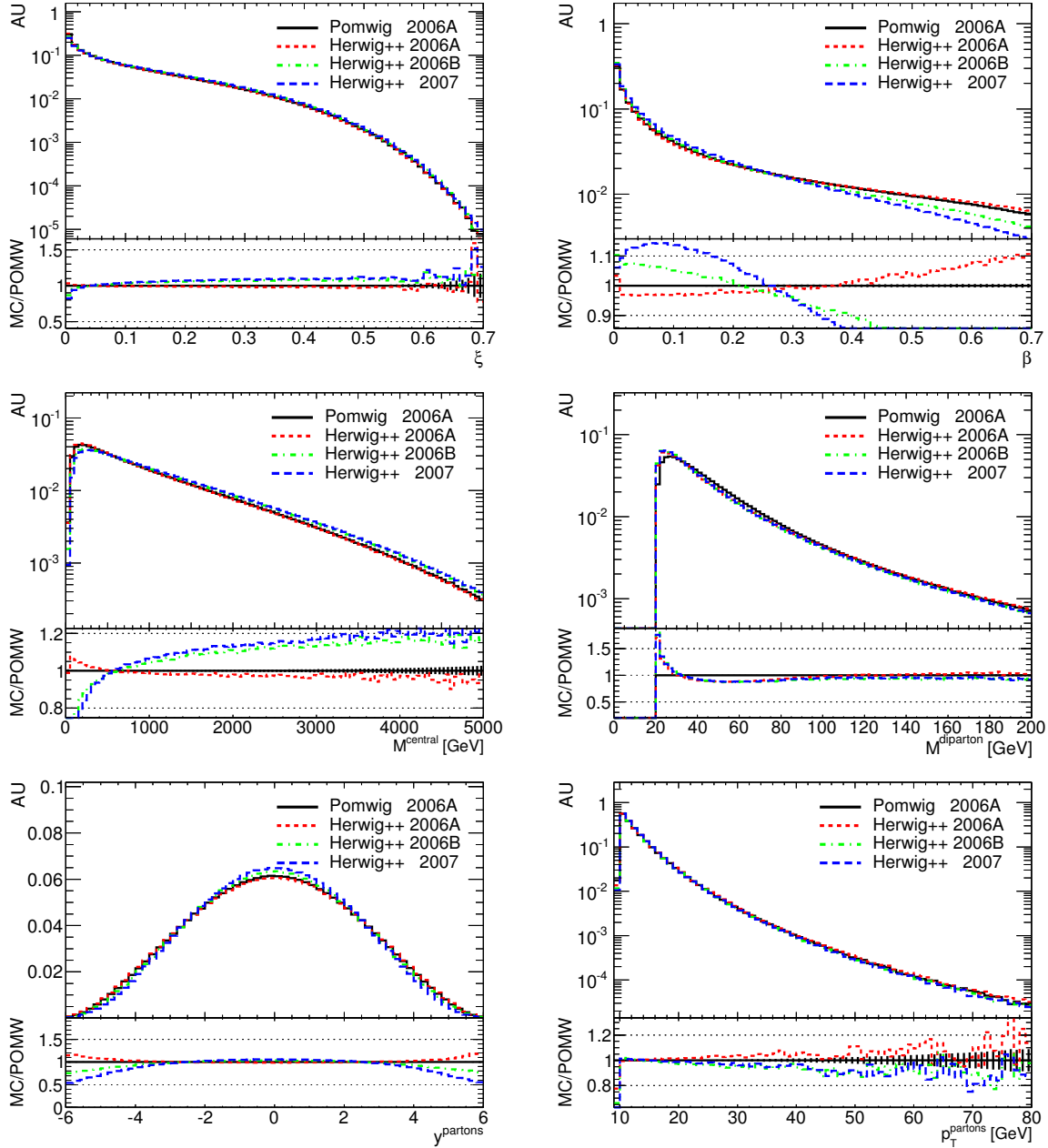


Figure 7.2: Comparison of DPE di-jet production at $\sqrt{s} = 14$ TeV between POMWIG and HERWIG++. HERWIG++ is presented for its three PDF fits 2006 A, 2006 B, 2007. Figure shows momentum fraction loss of proton and pomeron, mass of the produced system including and without pomeron remnants, rapidity and transverse momentum of partons produced in hard process. A small differences on parton level between POMWIG and HERWIG++ with the same PDF 2006 A are caused by implementation details of the hard processes and PDF. Larger discrepancy can be seen on the level of stable hadrons which is caused by different HERWIG++ hadronisation tune.

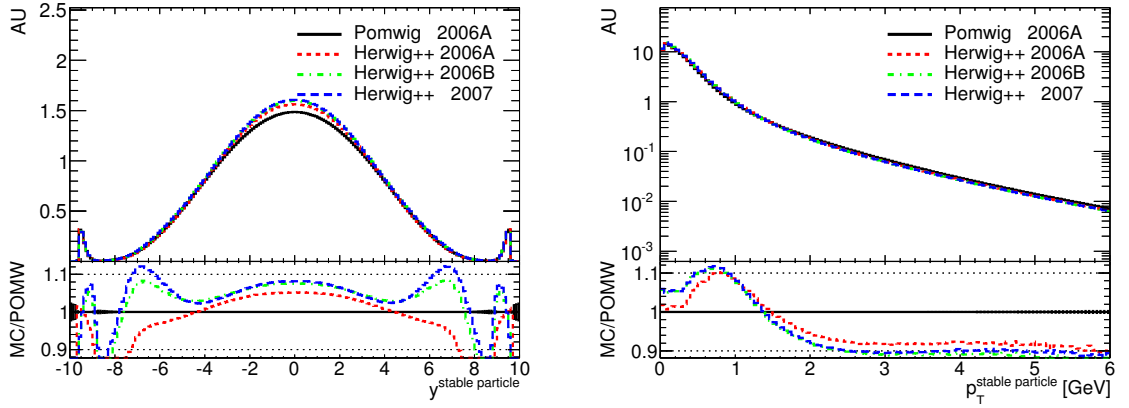


Figure 7.3: Comparison of DPE di-jet production at $\sqrt{s} = 14\text{TeV}$ between POMWIG and HERWIG++. HERWIG++ is presented for its three PDF fits 2006 A, 2006 B, 2007. Larger discrepancy can be seen on the level of stable hadrons which is caused by different HERWIG++ hadronisation tune.

attributed to implementation details such as frame at which the parton masses and momenta are generated. Larger differences are apparent for the distributions of hadrons at generator level which are shown in Figure 7.3. HERWIG++ produces particles with smaller transverse momentum than HERWIG. The rapidity distribution of final hadrons is also different even when the same PDF is used. This difference is due to tuning of HERWIG++ hadronisation model to LEP data.

7.3 QCD Exclusive Processes

Implementation of QCD exclusive processes is based on the Durham model [30] which has been successful in description of these phenomena at Tevatron. So far the following set of one and two particle final states has been implemented: Higgs production, di-jet production, and di-photon production. The final goal is supplement these processes by three particle final state production which can have higher yields than two particle production due to $J_z = 0$ selection rule. For example, $q\bar{q}g$ can create larger background to Higgs production than $q\bar{q}$ production.

The complexity of the phase-space integration grows exponentially with increasing number of final states. Thus a high performance automatic sampler is necessary to integrate the complicated phase-space of three particle production. This is one of the reasons why those processes have not been implemented in any other MC generator yet.

7.3.1 Durham Model in Herwig++

The Feynman diagram for the Higgs production in Durham model is displayed in Figure 4.8. In this model, differential cross section is factorized into luminosity of radiated gluons \mathcal{L} and the

hard matrix element of desired process $\hat{\sigma}(gg \rightarrow X)$

$$M_X^2 \frac{\partial \sigma(pp \rightarrow pXp)}{\partial M_X^2 \partial y \partial t_1 \partial t_2} = S e^{b(t_1+t_2)} \frac{\partial^2 \mathcal{L}}{\partial M_X^2 \partial y} \hat{\sigma}(gg \rightarrow X), \quad (7.5)$$

where M_X is invariant mass of produced object X , y denotes its rapidity, $t_1 = (p_1 - p'_1)^2$, $t_2 = (p_2 - p'_2)^2$ are momenta transferred squared for both protons, $b = 4 \text{ GeV}^{-2}$, and constant factor S stands for gap survival probability. The derivation of the differential luminosity starts

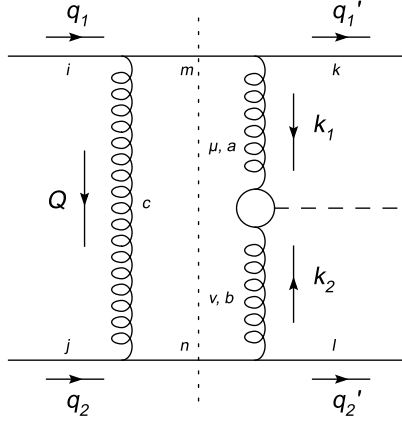


Figure 7.4: Feynman diagram for $qq \rightarrow q + H + q$. Figure taken from reference [105].

from the amplitude where the protons are replaced by quarks. The corresponding diagram is shown in Figure 7.4, where Q is four momentum of screening gluon and k_2 , k_1 are corresponding four momenta of fusing gluons. The imaginary part of the amplitude is computed using the Cutowsky rule. Approximating $Q \approx Q_T$ and considering the forward scattering limit in which the outgoing quarks carry no transverse momentum $Q_T = -k_{1T} = k_{2T}$, the cross section for $qq \rightarrow q + X + q$ takes a form

$$\sigma(qq \rightarrow q + X + q) = \frac{4}{s} \int \frac{dQ_T^2}{Q_T^4} \frac{(N_C^2 - 1)}{N_C^2} \alpha_S^2(Q_T) \hat{\sigma}(gg \rightarrow X). \quad (7.6)$$

In diagonal limit where momentum fractions carried by screening and fusing gluons are equivalent i.e. $x = x'$, and $k_T = 0$, the proton-gluon coupling is obtained by replacement of quark-gluon coupling $\alpha_S C_F / \pi$ by unintegrated gluon distribution function (3.29), see Figure 7.4. The Durham group corrects for the off-diagonality by factor R_g which takes a form

$$R_g(x, Q_T^2) = \left[1 + \frac{\partial \ln g(x, Q_T^2)}{\partial x} \left(0.82 + 0.56 \frac{\partial \ln g(x, Q_T^2)}{\partial x} \right) \right]. \quad (7.7)$$

In case of Higgs production at $\sqrt{s} = 14 \text{ TeV}$ it can be approximated by constant $R_g = 1.2$ with high accuracy. The unintegrated gluon distribution functions are provided by LHAPDF [103] and the derivative is performed numerically in HERWIG++. The cross section of exclusive production

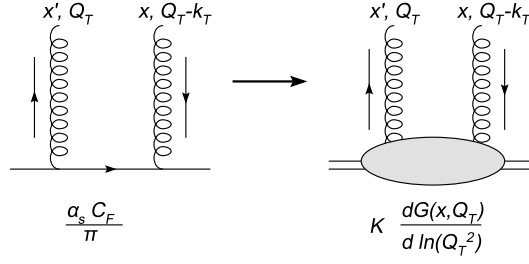


Figure 7.5: The recipe for replacing the quark line (left) by a proton line (right). Figure taken from reference [105].

has to be supplemented by Sudakov Form Factor

$$T(Q_T, \mu) = \exp \left[- \int_{Q_T^2}^{(\mu/2)^2} \frac{dp_T^2}{p_T^2} \frac{\alpha_S(p_T)}{2\pi} \int_0^{1-\Delta} dz (n_f P_{qg}(z) + z P_{gg}(z)) \right], \quad (7.8)$$

where $\Delta = \frac{k_T}{\mu + k_T}$ and n_f is number of active flavours. The Sudakov Form Factor ensures that gluons attached to the centrally produced system X do not radiate further partons between scales $\mu/2$ and Q_T . By default, HERWIG++ sets $\mu = \sqrt{s}$ according to a new calculation of T. Coughlin [106] which corrects original KMR value $\mu = 0.64\sqrt{s}$. In addition, the rapid fall of the Sudakov Form Factor $T(Q_T, \mu)$ makes infrared limit $Q_T \rightarrow 0$ of equation (7.6) finite. One of the free choices of the model is the form of the running coupling $\alpha_S(Q)$. HERWIG++ uses the same as in the EXHUME and freezes the $\alpha_S(Q)$ at some low scale Q_{freeze}

$$\alpha_S(Q) = \begin{cases} \frac{3}{11} \ln \frac{Q}{\Lambda_{\text{QCD}}}, & Q \geq Q_{\text{freeze}} \\ \frac{3}{11} \ln \frac{Q_{\text{freeze}}}{\Lambda_{\text{QCD}}}, & Q < Q_{\text{freeze}} \end{cases}, \quad (7.9)$$

where $Q_{\text{freeze}} = \Lambda_{\text{QCD}} = 80 \text{ MeV}$ is used by default in HERWIG++.

Finally, the differential luminosity can be written in form

$$M_X^2 \frac{\partial^2 \mathcal{L}}{\partial M_X^2 \partial y} = \left[\frac{\pi}{8b} \int \frac{dQ_T^2}{Q_T^4} f_g(x_1, Q_T^2) f_g(x_2, Q_T^2) \right]^2, \quad (7.10)$$

where $f_g(x, Q_T^2)$ are the off-diagonal gluon densities which are implemented in HERWIG++ as

$$f_g(x, Q_T^2) \simeq R_g(x, Q_T) \frac{\partial [\sqrt{T(x, Q_T)} x g(x, Q_T)]}{\partial \ln Q_T^2}. \quad (7.11)$$

The integral (7.10) is computed using Gaussian quadratures. In order to numerically integrate $Q_T \rightarrow \infty$ the integral has to be split at some point Q_T^{mid} and the transformation $Q_T \rightarrow 1/Q_T$ needs to be performed. The integrand of (7.10) is plotted in Figure 7.6 from which can be seen that the function has sharp peak about $Q_T \approx 1.1 \text{ GeV}$ and then falls to 0 while going to infinity. Thus it is reasonable to choose $Q_T^{\text{mid}} \approx 4 \text{ GeV}$ and compute the first interval with high precision.

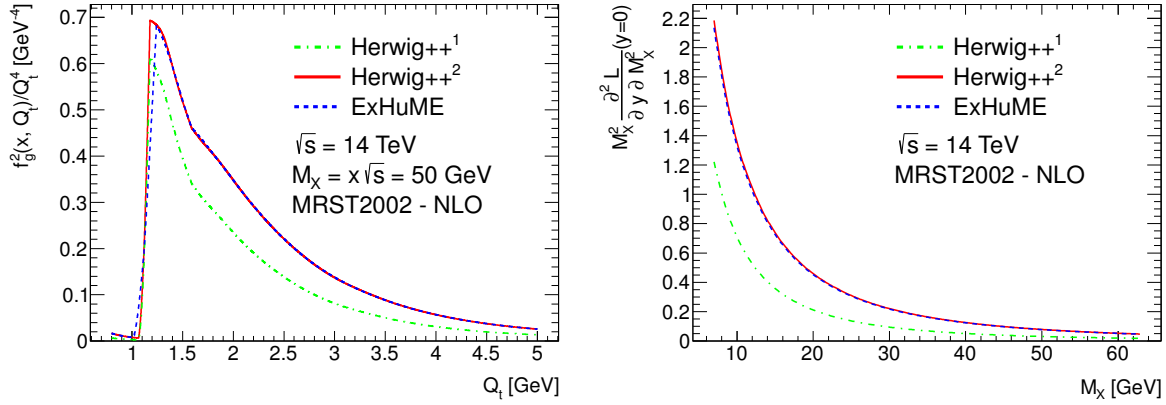


Figure 7.6: Comparison of HERWIG++ luminosity with EXHUME. Version HERWIG++¹ uses precise derivation of Sudakov Form Factor while HERWIG++² uses the same approximation as EXHUME.

The evaluation of luminosity is CPU demanding and thus on-the-fly event generation would be slow. Therefore, HERWIG++ generates a table with differential luminosity (7.10) which is interpolated during MC generation. HERWIG++ provides default set of tables with luminosity for LHC and Tevatron energies but user can easily generate any other table to meet his specific requirements.

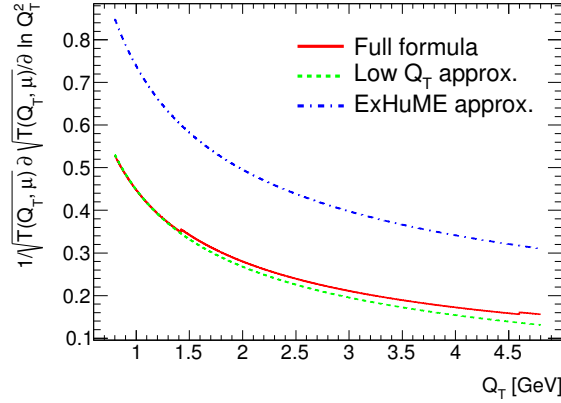


Figure 7.7: Comparison between analytic derivative of Sudakov Form Factor (7.12) (Full formula), approximation at small Q_T (7.13) (Low Q_T approx.), and formula (7.14) used in EXHUME (EXHUME approx.).

The implementation of the luminosity in HERWIG++ has been validated against well tested EXHUME. The main difference between the implementation is in the evaluation of derivative of

Sudakov Form Factor. The analytic derivative of Sudakov Form Factor (7.8) has the form

$$\begin{aligned} \frac{\partial \sqrt{T(Q_T^2, \mu)}}{\partial \ln Q_T^2} &= -\sqrt{T(Q_T^2, \mu)} \frac{\alpha_S(Q_T)}{4\pi} \\ &\times 6 \left[-(1-\Delta)^2 + \frac{(1-\Delta)^3}{3} - \frac{(1-\Delta)^4}{4} - \ln \Delta \right] \\ &+ n_f \left[\frac{[(1-\Delta) - (1-\Delta)^2]}{2} + \frac{(1-\Delta)^3}{3} \right] \end{aligned} \quad (7.12)$$

and is used in HERWIG++. Since the integrand of the differential luminosity (7.10) dominates at small Q_T the (7.12), neglecting Δ in polynomial terms and fixing $n_f = 3$ does not cause large error. Thus formula

$$\frac{\partial \sqrt{T(Q_T^2, \mu)}}{\partial \ln Q_T^2} \approx -\sqrt{T(Q_T^2, \mu)} \frac{3\alpha_S(Q_T)}{2\pi} \ln \left(\frac{2Q_T}{\mu + Q_T} \right) \quad (7.13)$$

approximates well (7.12) at small Q_T as can be seen from Figure 7.7. However, ExHUME uses formula [107]

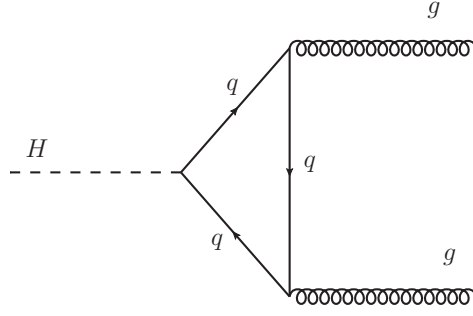
$$\frac{\partial \sqrt{T(Q_T^2, \mu)}}{\partial \ln Q_T^2} \approx -\sqrt{T(Q_T^2, \mu)} \frac{3\alpha_S(Q_T)}{2\pi} \ln \left(\frac{Q_T}{3(\mu + Q_T)} \right). \quad (7.14)$$

with factor $\frac{1}{3}$ instead of 2 inside the logarithm. This has approximately double magnitude at small Q_T as shown in Figure 7.7. The discrepancy is currently discussed with ExHUME and Durham model authors.

The effect on the luminosity is presented in Figure 7.6, where two versions of HERWIG++ are compared with ExHUME. The HERWIG++¹ uses precise analytic Sudakov derivative (7.12) while HERWIG++² contains exactly the same formula as in ExHUME, (7.14), in order to make sure that the rest of the implementation agrees between these two generators. The difference in the luminosity and thus in the final cross section is around 50%.

Process	HERWIG++ ¹	HERWIG++ ²	ExHUME
Higgs	0.889 fb	2.78 fb	2.75 fb
$q\bar{q}$	0.0718 nb	0.171 nb	0.18 nb
gg	69.9 nb	177 nb	96.5 nb
$\gamma\gamma$	7.79 fb	19.3 fb	20.8 fb

Table 7.3: Cross section for central exclusive production at $\sqrt{s} = 14$ TeV of Higgs boson of mass 120 GeV, $q\bar{q}$, gg , and $\gamma\gamma$ pairs with $p_T^{\text{cut}} = 10$ GeV, $20 < M < 120$ GeV and $|\cos \theta| < 0.95$ where M is invariant mass of the pair and θ is polar angle of the scattered particle in center-of-mass of gg collision. Cross sections are compared between HERWIG++¹, HERWIG++² with (7.14) and ExHUME.

Figure 7.8: Feynman diagram for Higgs decay amplitude $H \rightarrow gg$.

7.3.2 SM Higgs Production

Cross section for Standard Model Higgs production for colour singlet gluons with $J_z = 0$ is calculated using

$$\hat{\sigma}(gg \rightarrow H) = \frac{2\pi^2 K \Gamma_0(H \rightarrow gg)}{M} \lambda(M), \quad (7.15)$$

where factor the $K = 1 + \frac{\alpha_s(M/2)}{\pi}(\pi^2 + 11/2) \simeq 1.5$ is a NLO correction, M is Higgs boson off-shell mass, $\Gamma_0(H \rightarrow gg)$ is partial Higgs decay width and $\lambda(M)$ is Breit-Wigner distribution or lineshape defined in [108] in order to generate Higgs mass off-shellness M . Partial decay width $\Gamma_0(H \rightarrow gg)$ is given by [109]

$$\Gamma_0(H \rightarrow gg) = \frac{\alpha_s^2(M/2) g^2 M_H^3}{128\pi^3 m_W^2} \left| \sum_q \tau_q [1 + (1 - \tau_q) f(\tau_q)] \right|^2 \quad (7.16)$$

$$f(\tau) = \begin{cases} \sin^{-2}(1/\sqrt{\tau}), & \tau \geq 1 \\ -\frac{1}{4} \ln \left[\frac{1+\sqrt{1+\tau}}{1-\sqrt{1+\tau}} - i\pi \right], & \tau < 1 \end{cases}, \quad (7.17)$$

where g is electroweak coupling, m_W is mass of the W boson. The sum runs over quark flavours, q , contributing into the loop in the Feynman diagram displayed in Figure 7.8. Since $\tau_q = 4m_q^2/M_H^2$ can be neglected for $m_q \ll M_H$ HERWIG++ implements only contribution from t and b quark giving the dominant contribution.

The cross section for SM Higgs production at $\sqrt{s} = 14$ TeV is calculated using HERWIG++¹ and HERWIG++² and compared with EXHUME and Durham theoretical prediction ~ 3 fb for Higgs with mass of 120 GeV [30]. Both the cross section and individual distribution exhibit nice agreement between HERWIG++² and EXHUME. The suppression of HERWIG++¹ cross section reflects the suppression in luminosity due to precise formula for derivative of Sudakov Form Factor (7.12) discussed previously. Apart from the cross section, HERWIG++¹ slightly differs also at large ξ and therefore large rapidities. It should be noted that there is a large uncertainty in the choice of the PDF which influence the final cross section up to factor 3 therefore the value 3 fb can be easily achieved with HERWIG++¹ and $\mu = \sqrt{s}$ instead of $\mu = 0.64\sqrt{s}$.

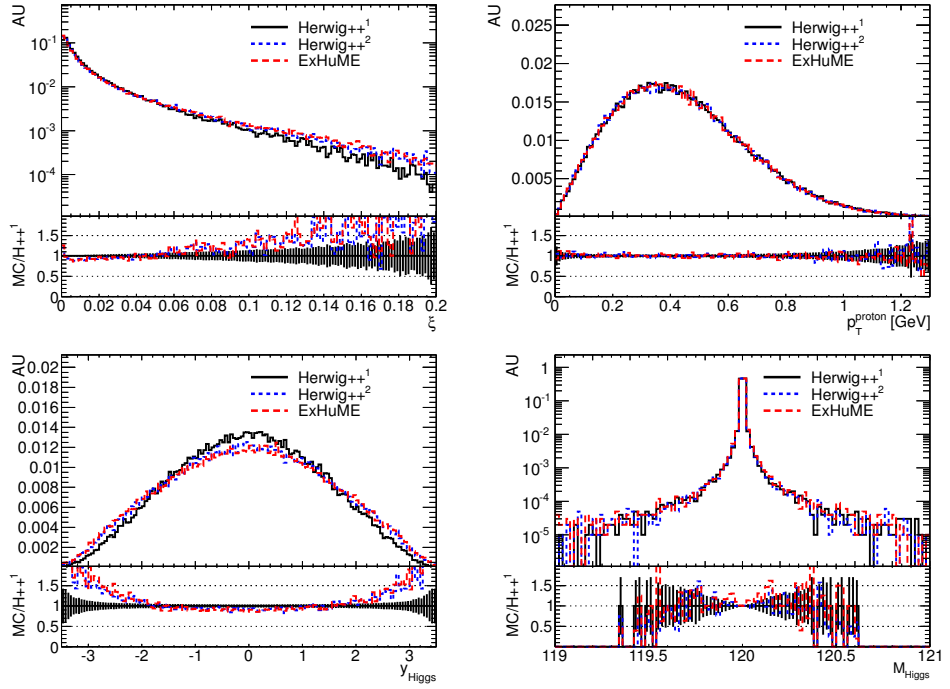


Figure 7.9: Comparison of ξ , transverse momenta of proton, Higgs mass and rapidity distributions in central exclusive production of Higgs boson of mass 120 GeV at $\sqrt{s} = 14$ TeV between HERWIG $++^1$, HERWIG $++^2$ with (7.14) and EXHUME.

7.3.3 Di-Jet Production

Two particle final state cross sections are integrated over $\cos \theta$, where θ is an polar angle of one of the outgoing particles in the center-of-mass frame of colliding gluons. The differential cross section for di-jet production is separated into $q\bar{q}$ and gg production where the cross section of the subprocesses is constrained by $J_z = 0$ and colour singlet rules [30]

$$\frac{d\hat{\sigma}^{q\bar{q}}}{d\cos\theta} = \frac{4}{3} \frac{\pi\alpha_S^2(M^2)}{M^2} \frac{m_q^2}{M^2} \left(1 - \frac{4m_q^2}{M^2}\right)^{\frac{3}{2}}, \quad (7.18)$$

$$\frac{d\hat{\sigma}^{gg}}{d\cos\theta} = 18 \frac{\pi\alpha_S^2(M^2)}{M^2 \sin^4\theta}. \quad (7.19)$$

The equations show that $q\bar{q}$ production is suppressed with respect to gg by factor $\frac{m_q^2}{M^2}$ which prefers production of heavy quarks as was already mentioned. Since both cross sections diverge when $\theta \rightarrow 0$, a cut $|\cos\theta_{\max}|$ has to be applied.

The cross section for $q\bar{q}$ production well agrees between HERWIG $++^2$ and EXHUME while cross section for gg is smaller by factor two in EXHUME, see Table 7.3. In EXHUME the factor 1/2 is used for gg but not in $q\bar{q}$. This factor is supposed to come from substitution $t \rightarrow \cos\theta$ in the integration. The discrepancy is under discussion with EXHUME authors. The relevant distribution exhibits exact match between HERWIG $++^2$ and EXHUME, as can be seen from

Figure 7.10. The default version HERWIG++¹ slightly disagrees at large ξ and rapidities of the outgoing partons.

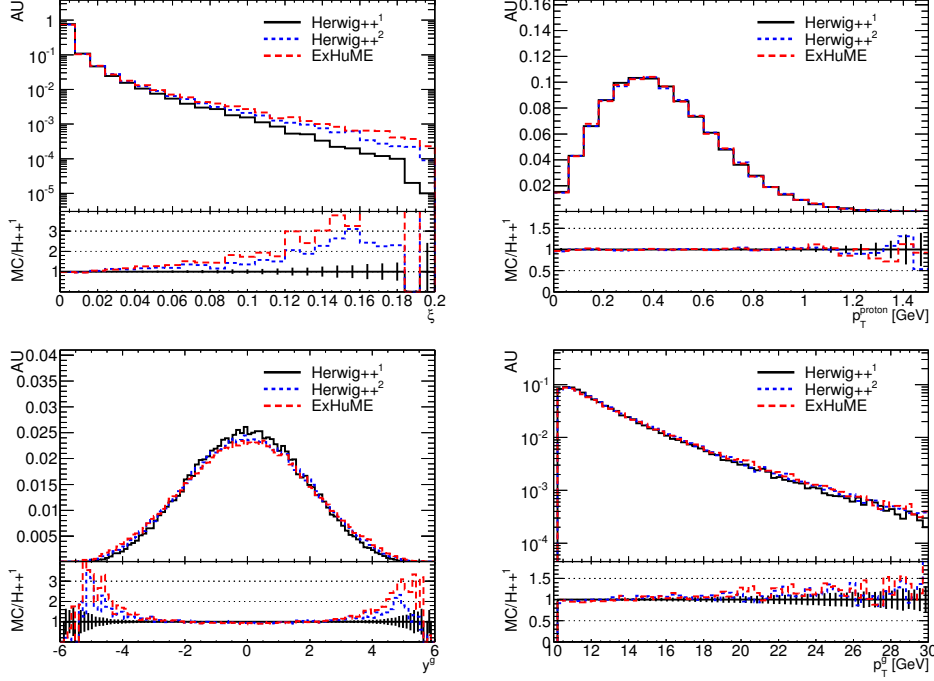


Figure 7.10: Distributions of ξ , proton p_T , gluon p_T and rapidity in central exclusive production of gg with $p_T^{\text{cut}} = 10 \text{ GeV}$, $20 < M < 120 \text{ GeV}$ and $|\cos \theta| < 0.95$, where M is invariant mass of the gluon system, θ is polar angle of the outgoing gluon in center-of-mass of gg collision. HERWIG++¹, HERWIG++² with (7.14) and EXHUME are compared.

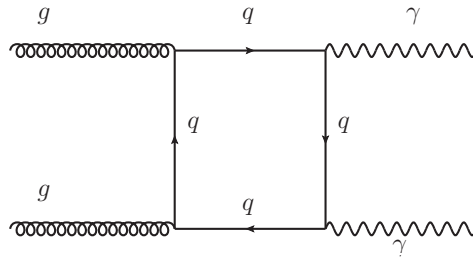


Figure 7.11: Feynman diagram for amplitude $gg \rightarrow \gamma\gamma$

7.3.4 Di-Photon Production

Two photons can be produced in SM via fermion loop similarly as in the case of the Higgs production thus an investigation of this process is important. The differential cross section is derived from reference [110] which provides helicity amplitudes for two photon scattering

$\gamma\gamma \rightarrow \gamma\gamma$. The amplitudes are related to helicity amplitudes $gg \rightarrow \gamma\gamma$ as

$$\mathcal{M}_{\lambda_1\lambda_2\lambda_3\lambda_4}^{gg\gamma\gamma} = \frac{\alpha_S}{2\alpha Q^2 N_C} \mathcal{M}_{\lambda_1\lambda_2\lambda_3\lambda_4}^{gg\gamma\gamma}, \quad (7.20)$$

where $\lambda_{1,2}, \lambda_{3,4}$ are helicities of incoming and outgoing bosons, Q^2 is quark fractional charge of units e in the fermion loop and $N_C = 3$ is number of colours. This relation is obtained by exchange of outgoing photon fermion vertices for gluon quark vertices. The amplitude for $J_z = 0$ rule has then the following form

$$\begin{aligned} \mathcal{M}_{J_z=0}^2 &= 2(\mathcal{M}_{++++} + \mathcal{M}_{--++})^2 + 2(\mathcal{M}_{++--} + \mathcal{M}_{--+-})^2 \\ &\propto 2 \left[-\frac{1}{4}(1 + \cos\theta) \left(\ln \left(\frac{1 - \cos\theta}{1 + \cos\theta} \right) + \pi^2 \right) - \cos\theta \ln \left(\frac{1 - \cos\theta}{1 + \cos\theta} \right) \right]^2 + 8 \\ &\equiv M_{J_z=0}^2 \end{aligned} \quad (7.21)$$

and the differential cross section is written as

$$\frac{d\hat{\sigma}^{\gamma\gamma}}{d\cos\theta} = \frac{34}{81} \frac{\alpha_S(M^2)\alpha}{4\pi^2 M^2} M_{J_z=0}^2. \quad (7.22)$$

Comparison of the cross section and relevant distributions can be seen in Table 7.3 and Figure 7.12. As in previous processes HERWIG++² well agrees with EXHUME but HERWIG++¹ gives smaller cross section and slightly different distributions due to changed derivative of Sudakov Form Factor (7.12).

7.4 Summary

Models for hard diffraction and exclusive production in two photon initiated processes were added into HERWIG++ release 2.5 [84] as a part of this work. The HERWIG++ provides many matrix elements that can be used for single diffractive, double pomeron exchange or QED exclusive productions. The framework with several matrix elements for exclusive QCD production of Higgs, di-jets and $\gamma\gamma$ is prepared to be submitted into HERWIG++ release after clarification of the mentioned discrepancies with EXHUME. The outlook is addition of $q\bar{q}g$ and $W\bar{q}q$ processes which are important backgrounds for Higgs production and $\gamma\gamma \rightarrow WW$ measurements.

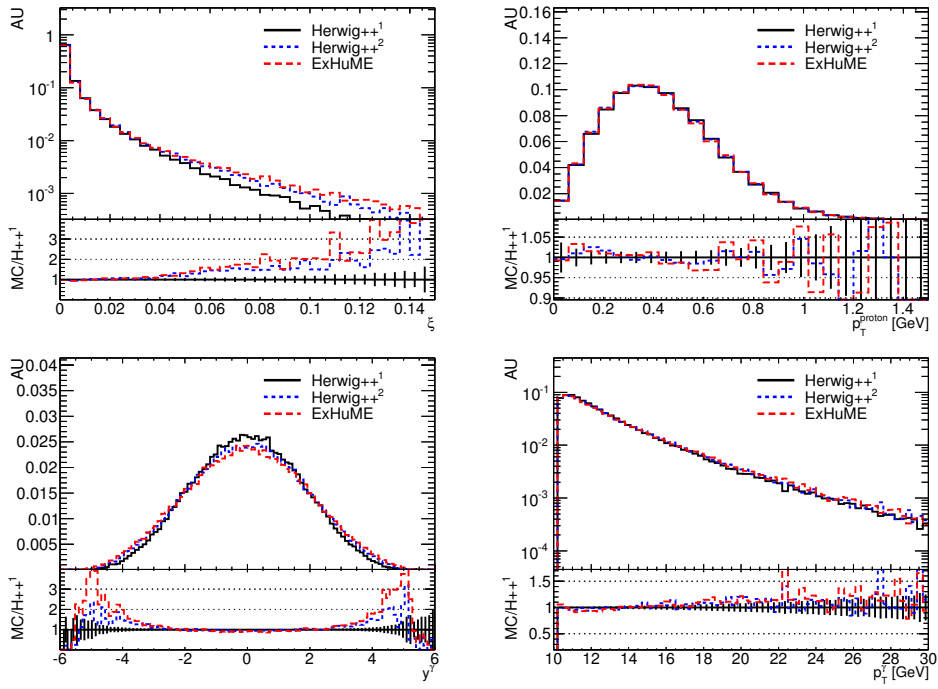


Figure 7.12: Distributions of ξ , protons p_T , photons p_T and rapidity in central exclusive production of $\gamma\gamma$ with $p_T^{\text{cut}} = 10 \text{ GeV}$, $20 < M < 120 \text{ GeV}$ and $|\cos\theta| < 0.95$, where M is invariant mass of $\gamma\gamma$ system, θ is polar angle of the outgoing photon in center-of-mass of gg collision. HERWIG++¹, HERWIG++² with (7.14) and EXHuME are compared.

Chapter 8

Experimental Definition of Rapidity Gaps

The experimental signature of diffractive events is production of large rapidity gaps, i.e. regions in rapidity devoid of particle activity. However, the rapidity gaps are also created in non-diffractive processes due to fluctuation in hadronisation process, although they are exponentially suppressed with size [111] of the gap, contrary to diffractive events. A precise experimental determination of rapidity gaps is required either to separate diffractive and non-diffractive events or to measure a cross section as a function of rapidity gaps.

This chapter is devoted to an experimental definition of rapidity gap using the ATLAS detector. In fact, pseudorapidity gap instead of rapidity gap is measured. As was already mentioned, this does not introduce large difference. Moreover, pseudorapidity is experimentally well measurable observable. In the following text, the rapidity gap means a pseudorapidity region without particle activity.

The rapidity gap is determined using the ATLAS calorimeter system in combination with Inner Detector. The algorithms for experimental gap reconstruction are discussed in the following. Two different definitions of rapidity gaps are used in the following analysis:

- **Forward rapidity gap** $\Delta\eta^F$: is the larger of the two empty pseudorapidity regions expanding between the edges of the detector of the acceptance $\eta = 4.9$ or $\eta = -4.9$ and the nearest particle.
- **Floating rapidity gap** $\Delta\eta$: is the largest empty pseudorapidity region between two nearest particles in η , inside the detector acceptance $\eta \in [-4.9, 4.9]$. The gap is fully determined by its position, defined as position of its edge having the larger absolute value of pseudo-rapidity, denoted as $|\eta_{\text{start}}|$.

The former definition is used for measurement of the rapidity gap cross section of inelastic processes in Chapter 11. Since the $\Delta\eta^F$ is one dimensional observable, both experimental corrections

and the result interpretation from the theoretical and experimental point of view is simple. The later definition provides the 2-dimensional information about size and position of the gap that improves separation between SD and DD topologies. Therefore, the 2-dimensional definition was used for estimation of diffractive fractions in Chapter 10.

8.1 Rapidity Gaps in the Calorimeter

The ATLAS calorimeter system is used for measurement of rapidity gaps because of its large coverage $|\eta| < 4.9$. To correctly reconstruct rapidity gaps, the lowest possible deposits of energy in the calorimeter have to be evaluated, however in such a way as not to be directly sensitive to detector noise. The calorimeter noise is controlled on the level of calorimeter cells which are the basic read-out units in ATLAS. The cell noise is in general well described by Gaussian distribution (except the Tile calorimeter see below) with standard deviation σ_{noise} . Therefore, significance variable S defined as

$$S = \frac{E}{\sigma_{\text{noise}}}, \quad (8.1)$$

where E is energy deposited in the cell, is convenient for noise discrimination, as was proposed in ref. [101]. A requirement that cell exceeds a significance threshold, S_{th} , thus determines a probability

$$P_{\text{cell}}(S_{\text{th}}) = \frac{1}{\sqrt{2\pi}} \int_{S_{\text{th}}}^{\infty} dS \exp\left(-\frac{S^2}{2}\right). \quad (8.2)$$

that energy deposit in given cell is noise fluctuation. In order to reconstruct particle energy, signal from several neighbouring cells along the particle trajectory needs to be read out. ATLAS uses topological clustering algorithm [112] which combines energy deposits in individual calorimeter cells. The algorithm looks for the cluster seed cell which significance fulfills condition $|S| > 4$. The seed cell is joined to the cluster with all surrounding cells satisfying $|S| > 2$. Finally, all the nearest neighbours to the already clustered cells are added. It should be noted that the absolute value in the significance conditions allows to cancel out the noise contribution either inside the individual clusters or in jets reconstructed from several clusters. Cluster n -th moments of a variable x defined as

$$\langle x^n \rangle = \frac{1}{E_{\text{clust}}} \sum_{\text{cell}, E_{\text{cell}} > 0} E_i x_i^n \quad (8.3)$$

describe position, size and shape of the cluster. These cluster properties are used for particle identification which allow to scale the energy response appropriately e.g. energy response is scaled differently for hadrons, electrons, photons. Topological clustering is good algorithm for estimation of real particle energy. However, it tends to pick up calorimeter noise. There are on average twelve reconstructed clusters in the whole calorimeter due to noise fluctuation. The default threshold $S_{\text{th}} = 4$ would spoil large rapidity gaps therefore it needs to be properly optimized to suppress the noise to acceptable level.

The clusters with the new optimized requirements for noise suppressions will be used for forward rapidity gap definition. The floating rapidity gaps used in the 2-dimensional algorithm are reconstructed at the cell level only i.e. cells above optimized significance threshold determine particle activity in given η region. The information about real particle energy is not required in the case of the 2-dimensional algorithm because it is used for estimation of diffractive fractions where the crucial point is to have different floating gap patterns for ND, SD, and DD topologies.

8.1.1 MC Simulation of Cell Noise

In order to compare gap distributions between MC and data, it is crucial to have a good description of the calorimeter noise in MC. The cell noise distributions and their parameterizations included in MC simulation is measured from the data. The noise was studied in more detail using the May ATLAS reprocessing of the data and MC. The level of understanding of the calorimeter noise is illustrated in Figures 8.1, 8.2. Figure 8.1 shows cell energy distributions for the whole calorimeter and for each of its sub-systems: EM, HEC, FCal, and Tile calorimeters. Cells which were flagged as bad by the offline shifters were all removed. There are three distributions: Minimum Bias MC generated with PYTHIA6, physics data from Minimum Bias Stream and data from Random Trigger Stream. For the physics data and PYTHIA6 prediction, the trigger L1_MBTS_1 was required to fire. On the other hand, events from Random Trigger Stream require the L1_RDO_EMPTY trigger, selecting events with no bunches present in ATLAS. In addition, the cell significance S is plotted in Figure 8.2. In the long positive tails the physics signal is clearly visible. Random Trigger data show the shape of the noise distribution in cells with minimum contamination from physics signal. It is symmetric around zero and the negative side exactly matches the negative part of the distributions in physics stream which is not contaminated by the physics signal.

In general, the noise distribution is described very well over seven orders of magnitude. Some discrepancy is observed between data and MC for negative energies in Figure 8.1, in HEC in particular. Presumably the same discrepancy is present at positive energies, but it is hidden in the physics signal. The effect of those discrepancies on the analysis are however not large because the observable which we use to reconstruct gaps is based on the cell significance S_{th} for which the disagreement is much less pronounced, i.e. these discrepancies are mapped to much higher significance. Moreover, the threshold cut is applied at positive energy values so that the small Data/MC disagreement at negative energies is irrelevant. It should be emphasized that the noise distributions included in MC model match those in data up to very high values of the significance so that cuts up to $S \approx 6$ can be safely applied to separate the physics signal from the noise.

Cell noise mean and RMS was also cross-checked for each cell individually using the Random Trigger sample with empty bunches in the run which was used for rapidity gap analysis. In

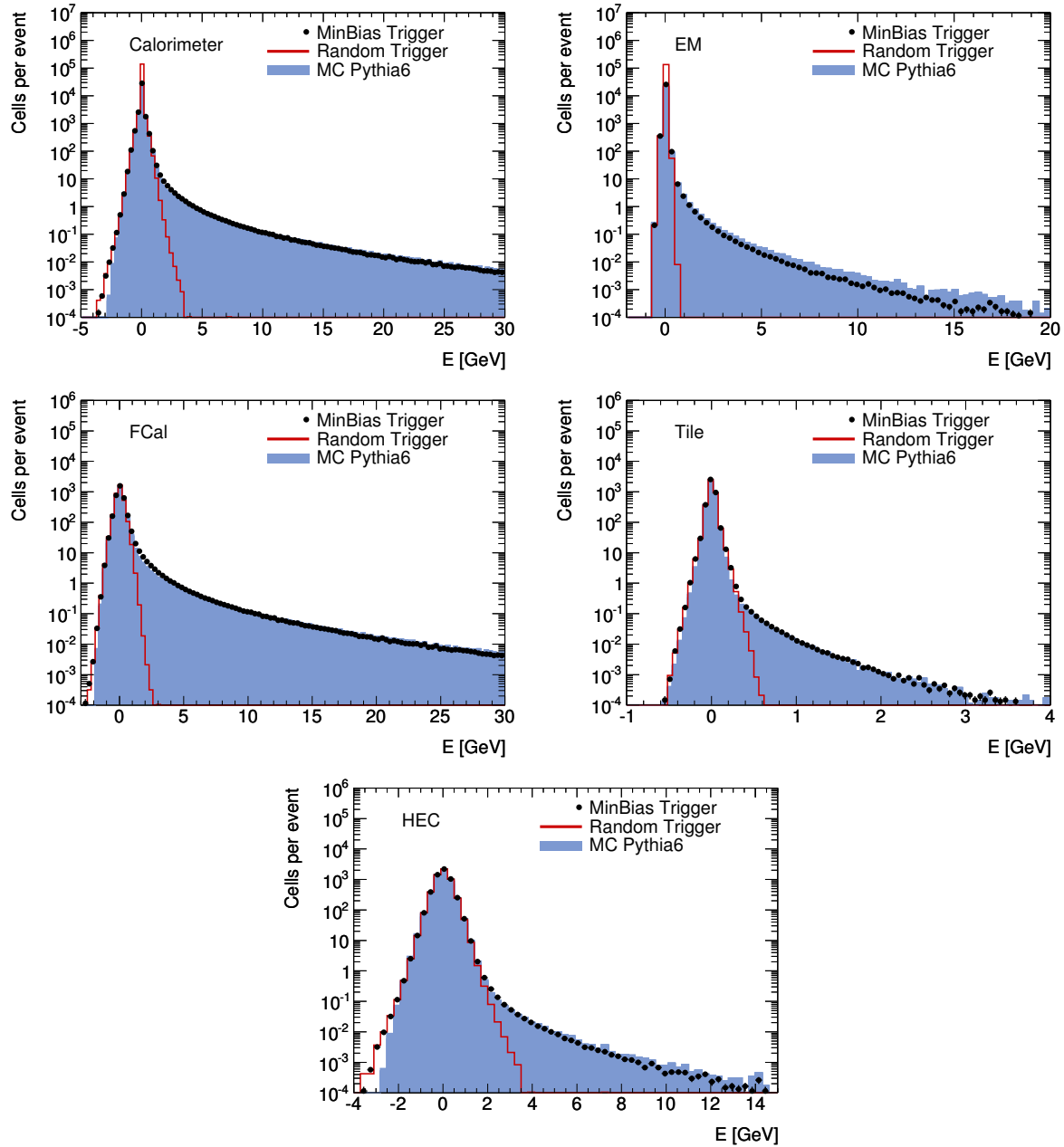


Figure 8.1: Cell energy distribution for cells in the whole calorimeter and for each calorimeter sub-detector: EM, FCal, HEC, Tile in physics and empty events.

addition the rate of a cell passing high $S_{\text{th}} = 5\sigma_{\text{noise}}$ noise was checked. 41 cells exhibiting slightly larger noise tails were identified and removed. This clean up has no effect on final results.

Shape of cell noise distribution in ATLAS calorimeter is well described by a Gaussian distribution with the exception of the Tile calorimeter which has a slightly longer tails. Double Gaussian distribution has to be used to describe the data satisfactory. Since the latter would create complications in constructing an algorithm based on simple Gaussian probabilities cells in the Tile calorimeter were ignored in the optimized cluster requirements. This exclusion does not deteriorate the gap resolution since the neutral hadrons are mostly π^0 which immediately decays two photons $\pi^0 \rightarrow \gamma\gamma$ and therefore they are detected in EM. Furthermore, those charged particles which do not leave enough signal in EM are detected in the Inner Detector with high efficiency.

8.1.2 Calorimeter Noise Separation

As it was already discussed, the identification of rapidity gap signatures relies crucially on the suppression of calorimeter noise contributions. To reduce the calorimeter noise, clusters of calorimeter energy deposits are considered only if they contain at least one cell outside the Tile calorimeter with an energy significance above an η -dependent threshold, $S_{\text{th}}(\eta)$.

Calorimeter region $[-4.9, 4.9]$ is divided into slices in η . The significance threshold $S_{\text{th}}(\eta)$ is set in such a way that a probability $P_{\text{slice}}(S_{\text{th}}(\eta)) = N_{\text{slice}}(\eta) \cdot P_{\text{cell}}(S_{\text{th}}(\eta))$, where $N_{\text{slice}}(\eta)$ is number of cells in given slice, that slice contains cell passing cut $S > S_{\text{th}}(\eta)$ due to noise fluctuation is the same for each slice i.e. the probability is uniform in whole calorimeter range, $P_{\text{slice}}(S_{\text{th}}(\eta)) = P$.

In the default configuration of the algorithm, detector range $|\eta| < 4.9$ is divided into 98 slices. The probability P and significance threshold $S_{\text{th}}(\eta)$ are fixed by pseudo-slice containing $N_{\text{norm}} = 500$ cells to value

$$P_{\text{slice}}(S_{\text{th}}(\eta)) = N_{\text{norm}} \cdot P_{\text{cell}}(S_{\text{norm}}) = P = 1.4 \times 10^{-4}, \quad (8.4)$$

where $S_{\text{norm}} = 5.5$. The number of cells in the calorimeter $N_{\text{slice}}(\eta)$ and the default significance threshold $S_{\text{th}}(\eta)$ as a function of η are shown in left and right plot of Figure 8.3, respectively. The threshold is small, $S_{\text{th}}(\eta) \sim 5.0$, in the forward region, where the cell density is low, and high, $S_{\text{th}}(\eta) \sim 5.8$, in the high density central region. The choice of the $S_{\text{norm}} = 5.5$ has been determined from the resolution of the rapidity gap reconstruction algorithm i.e. root mean square of correlation between rapidity gaps on MC truth and detector level. The resolutions for different thresholds $S_{\text{th}}(\eta)$ in which S_{norm} varies from 4.1 to 6.5 are presented in Figure 8.4. The small threshold values, S_{norm} , have good performance for small gaps but large gaps are very often spoiled by the calorimeter noise. On the other hand, large thresholds remove also physics

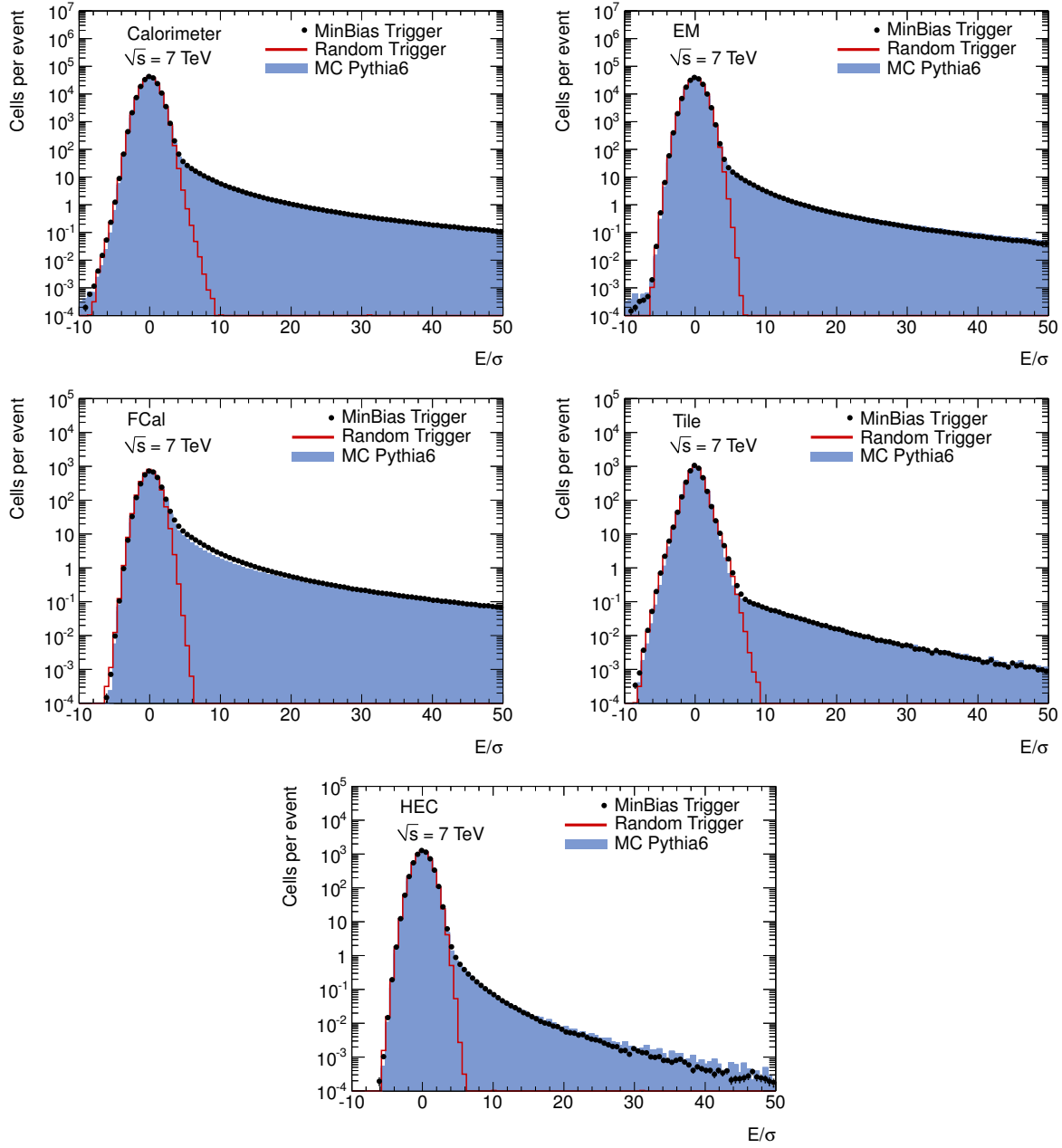


Figure 8.2: Cell energy significance for cells in the whole calorimeter and for each calorimeter sub-detector: EM, FCal, HEC, Tile physics and empty events.

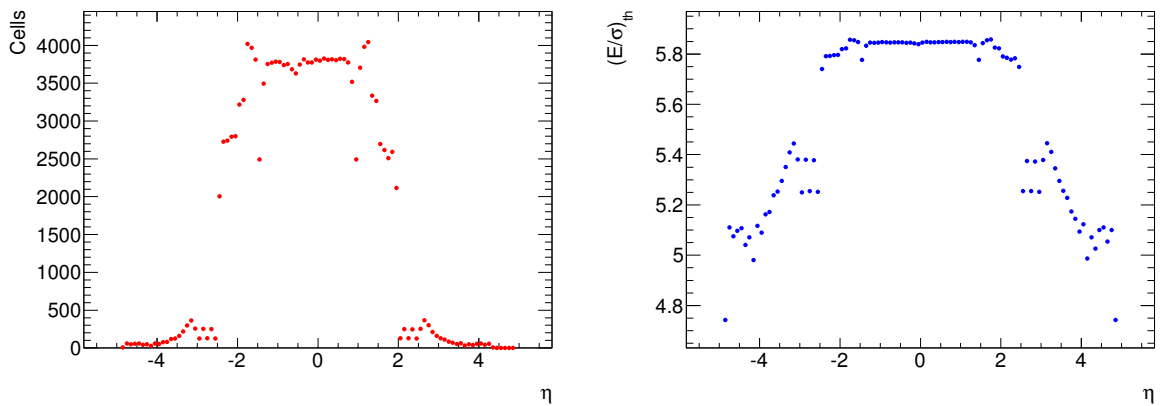


Figure 8.3: Number of cells in calorimeter, $N_{\text{slice}}(\eta)$, as a function of η (left) and cell threshold in terms of significance, $S_{\text{th}}(\eta)$, as a function of η (right).

signal and thus the algorithm makes the gap size larger. The threshold $S_{\text{norm}} = 5.5$ was chosen due to the best performance over the gap range from 0 to 8, which is the range used in our measurements. It should be noted that the nearest threshold 5.0 and 6.0 have similar behavior of the gap resolution and thus the result is not affected by small variation of the threshold $S_{\text{th}}(\eta)$.

Finally it is worth to mention that, many other algorithms were studied. For example, one can admit more cells above smaller significance threshold. This could lead to smaller effective cut on the particle energy with the same or better noise suppression, what is desired. It is also possible to think of many cuts on the cluster moments defined by (8.3). Such algorithms were studied and their performance was compared on minimum bias and empty events data samples. Data samples with empty events provide information about noise suppression performance while the minimum bias physics samples show how much physics signal is lost due to noise suppression requirements. The conclusion from these studies [113] is that the algorithm with simple significance cut presented above provides the best balance between the noise and signal suppression, from the set of the proposed algorithms, with a benefit of great simplicity.

8.2 Lowest Energy Detection Limit

The η -dependent significance cut established in order to remove calorimeter noise also remove non-negligible quantity of physics signal. In measurements of the rapidity gap distributions corrections for detector effects to level of stable final particles are required in order to compare the experimental results with the theory. If the probability of particle detection is low, large model dependent corrections are introduced to the experimental result. Therefore a particle level definition, ideally simple, theoretically unambiguous, which matches as closely as possible the detector level definition is required. On the other hand, the probability that energy deposited by a particle passing the calorimeter exceeds the threshold $S_{\text{th}}(\eta)$ is a function of many particle

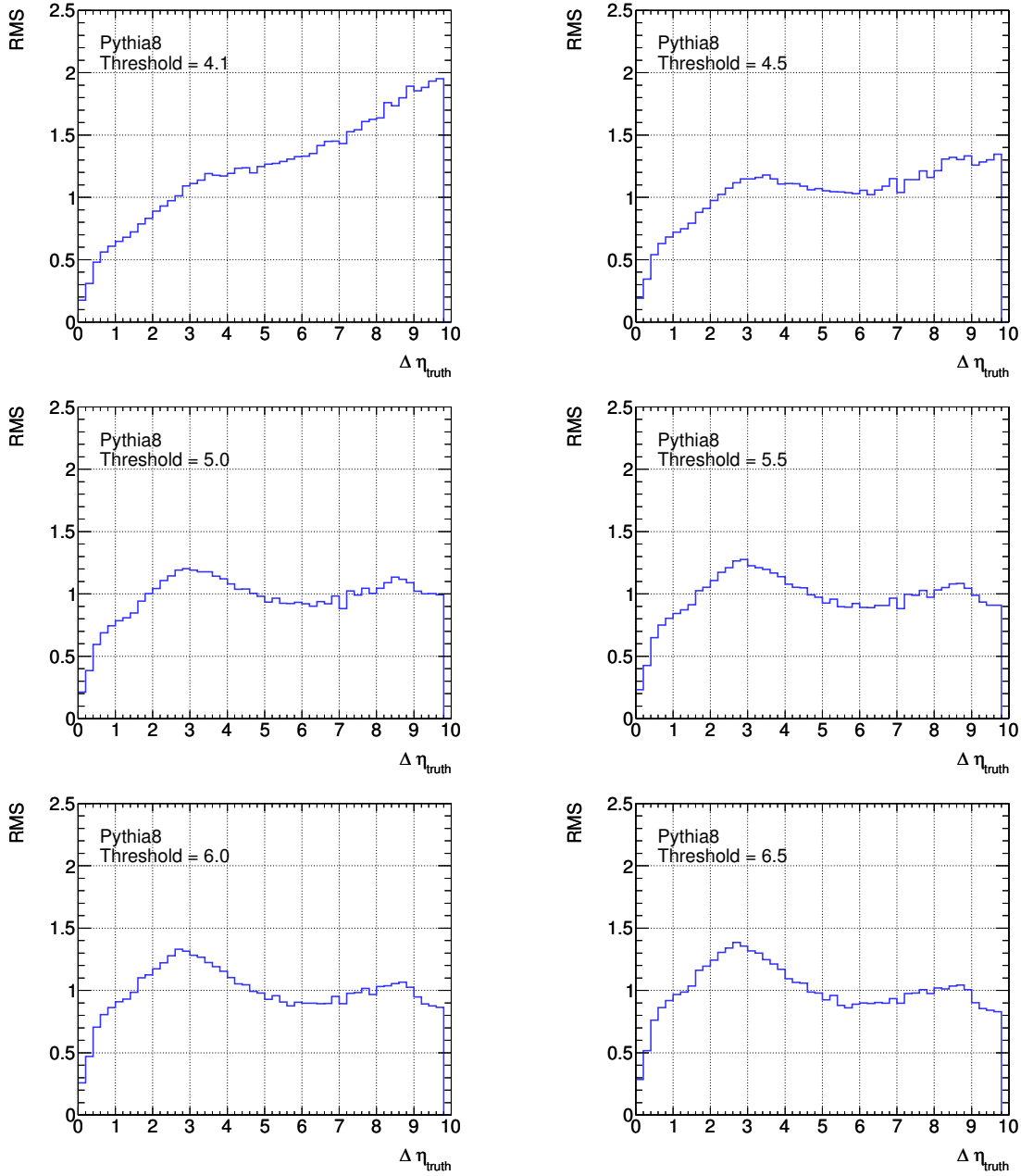


Figure 8.4: Gap resolution for ring noise probabilities observed in PYTHIAS: from left to right $P_{\text{noise}}(4.1, 4.5, 5, 5.5)$.

properties as momentum, charge, mass etc. and therefore an exact match between detector and generator level is difficult.

At the end, a fixed p_T cut of 200 MeV was chosen. The cut was applied to all stable particles at the generator level. A stable generator particle is defined by its decay length in the lab frame, $c\tau > 10$ mm. Under this definition, π_0 are not stable and are decayed (primarily to photons) by the generator. The choice of the cut on the transverse momentum was determined from several methods.

Figure 8.5 shows the Gaussian cell noise width averaged over cells in given η -slice scaled by the threshold cut $S_{th}(\eta)$ for each slice. In other words, it is an averaged minimum energy deposition in single calorimeter cell required for particle detection. The dashed lines maps transverse momentum p_T onto energy using the relation $\cos\theta = \tanh\eta$. First, it can be seen that it is better to perform a cut rather on the transverse momentum, which follows the average cell energy threshold, than cut on the particle energy. Second, since a particle traversing the calorimeter deposits only a fraction of its energy in a single cell its p_T has to be significantly above the averaged cell energy threshold over whole η range. Thus the lowest possible p_T which can be detected is around 200 MeV.

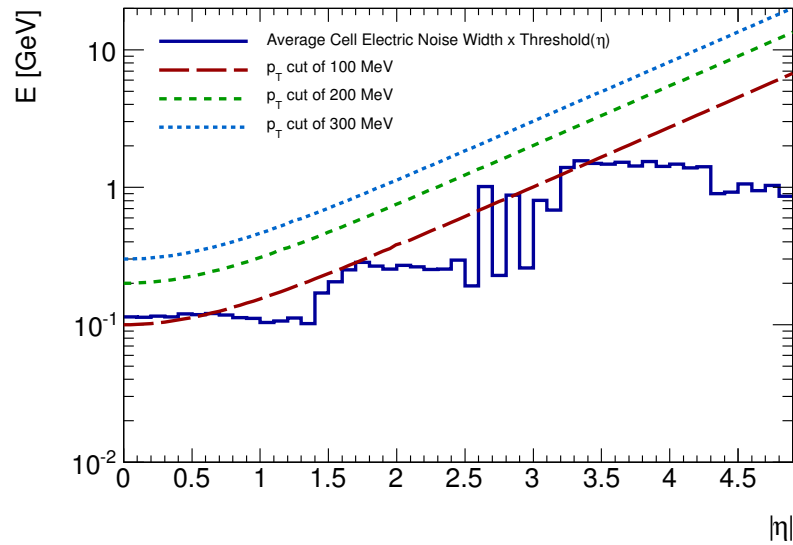


Figure 8.5: Average minimum energy deposition required in a single calorimeter cell to detect a particle as a function of $|\eta|$. The dashed lines show the minimum energy of a particle for different generator level p_T cuts. The chosen cut should be above the minimum energy to account for energy loss in the detector medium and energy deposition in multiple calorimeter cells.

Another approach to match the transverse momentum cut p_T^{cut} on generator level is a comparison of detector and generator level correlations matrices of forward rapidity gaps $\Delta\eta^F$ with different generator level p_T^{cut} . The correlation matrices for $p_T^{\text{cut}} = 0, 100, 200, 300, 400, 500$ MeV

are presented in Figure 8.6. The smallest migrations between detector and generator level and the best diagonality is achieved for cuts $p_T^{\text{cut}} = 100, 200, 300$ MeV. For smaller thresholds, the reconstruction of large gaps fails while at higher p_T^{cut} small gaps are incorrectly reconstructed.

The method based on the correlation plots purely relies on the MC simulation. A data driven method which uses tracks reconstructed in Inner Detector to estimate efficiency of detection in the calorimeter was used as well. The tracks needs to be extrapolated through solenoidal magnetic field in order to find their impact position in calorimeter. This method can estimate an efficiency only in central region in the Inner Detector coverage. The turn up of efficiency curves as function of particle momentum are very slow and it is difficult to choose a concrete cut. The probability to detect charged particle with $p_T > 200$ MeV is between 40% ($\eta \sim 0$) and 80% ($\eta \sim 2.5$). It should be noted that by adding the tracker into our gap finding algorithm the detection probability rapidly increases in the central region as it will be seen in next section. From the above studies, we conclude that the choice of $p_T^{\text{cut}} = 200$ MeV on stable particles at the generator level provides a reasonable match to the detector acceptance.

8.3 Adding Inner Detector Information

Merging an information about particle activity from the calorimeter and Inner Detector significantly improves the gap resolution. Since we chose cut on the transverse momentum of particles on generator level to be 200 MeV it is necessary to consider only tracks above this threshold. Additional requirements are applied in order to select tracks with a good reconstruction quality:

- kinematic cut: $p_T > 200$ MeV and $|\eta| < 2.5$;
- number of pixel hits $n_{\text{pix}} \geq 1$ and a B-Layer hit if hit expected from the track extrapolation;
- $n_{\text{SCT}} \geq 4$ if $p_T > 200$ MeV, $n_{\text{SCT}} \geq 6$ if $p_T > 300$ MeV;
- track algorithms: Inside Out or Low Pt [114];
- if vertex found: $|d_0| < 1.5$ mm, $|z_0| \sin(\theta) < 1.5$ mm with respect to primary vertex, else $|d_0| < 1.8$ mm with respect to beam spot,

where n_{pix} , n_{SCT} are number of hits in Pixel and SCT detectors, d_0 and z_0 are transverse and longitudinal distance of the closest approach with respect to primary vertex or beam-spot position. These are the ATLAS standard cuts used already for measurement of charged particle multiplicities [1, 85]. Figure 8.7 shows the benefit of the addition Inner Detector into the gap finding algorithm. Left plots show the correlation between $\Delta\eta$ at detector and particle level while the right plots show the same correlation for $\Delta\eta^F$ observable. The addition of the Inner detector makes the matrices more diagonal and improves the gap resolution.

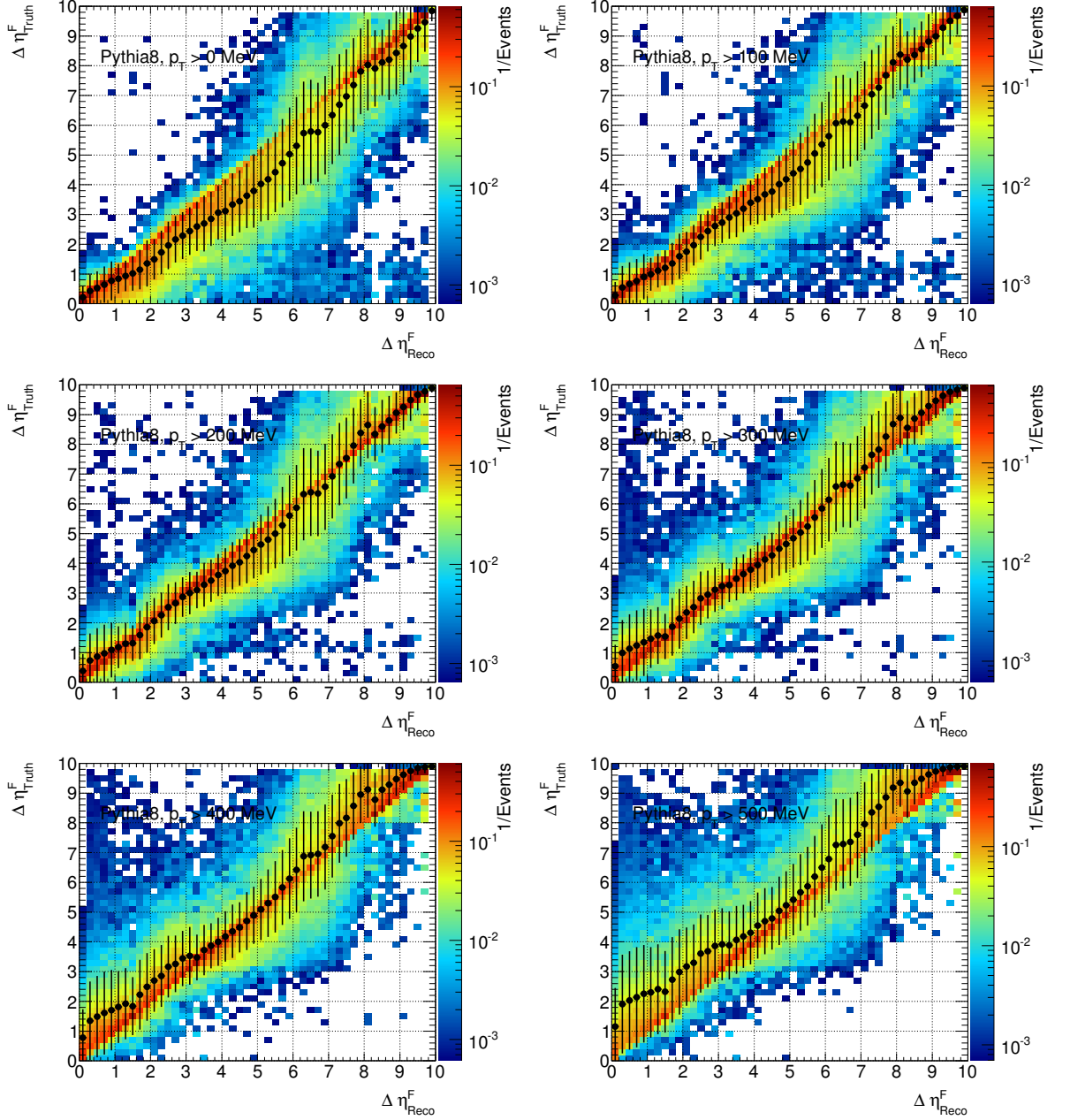


Figure 8.6: Plots show correlation of forward gaps on the detector and truth level. The error in the profile histograms represent detector resolution of forward rapidity gap reconstruction. Plots are made for various p_T on particle at truth level. For measurement of $\Delta\eta^F < 7$ the cut in range of 100 – 300 MeV cuts seems to be optimal.

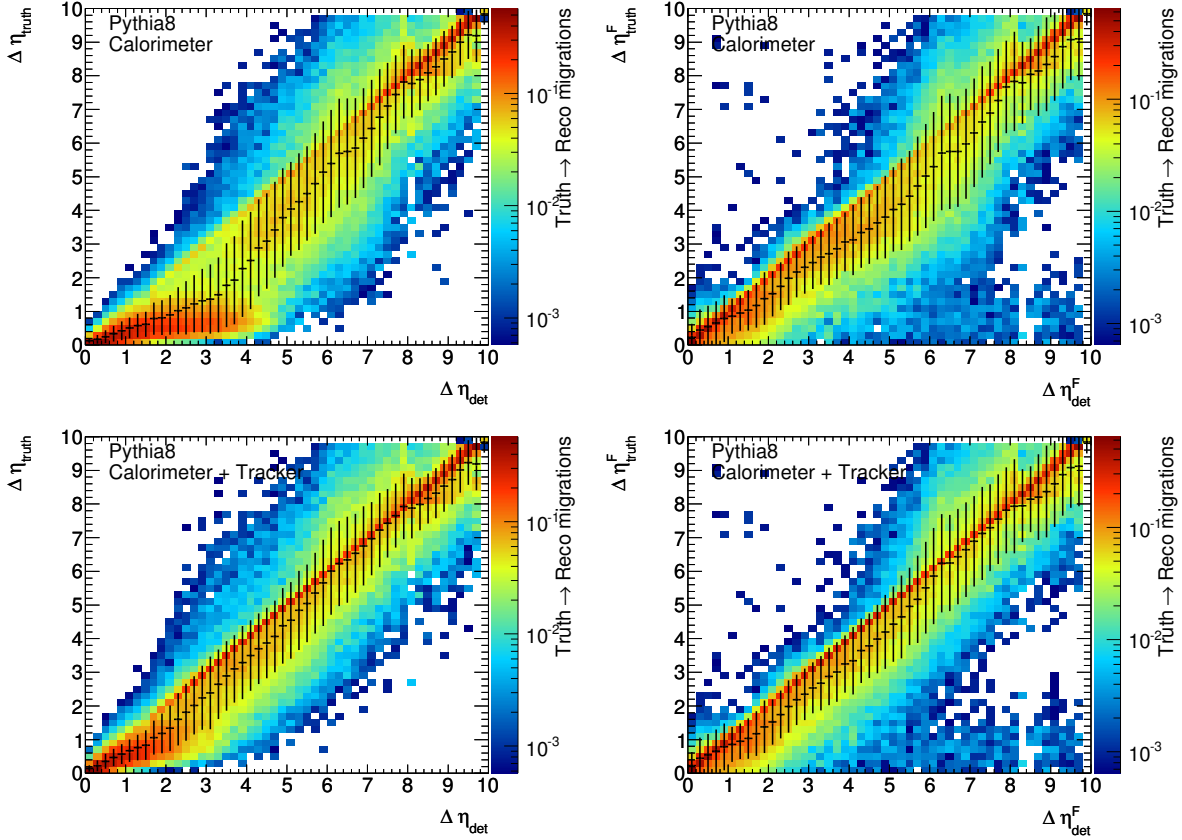


Figure 8.7: Correlation of the rapidity gap size between hadron and detector level using calorimeter only (top) and inner detector included (bottom). Correlation matrices are displayed for the largest floating gap found anywhere in the detector (left) and for the forward rapidity gap that is required to start at the edge of the detector $\eta_{\text{start}} = \pm 4.9$. Black markers and error bars denote the mean and RMS spread of the generator level gap as a function of the reconstructed gap size.

One could also consider adding information from the MBTS which has inner disc with coverage $2.09 < |\eta| < 2.82$ and outer disc $2.82 < |\eta| < 3.84$. However, the discs coverage would require a large bins in the distributions but more importantly the sensitivity of the MBTS is very different from the calorimeter and cannot be scaled to match the lowest calorimeter acceptance $p_{\text{T}}^{\text{cut}} = 200 \text{ MeV}$ as in the case of Inner Detector. This would cause a non-uniformity in the correlation matrices in Figure 8.7 leading to failure of unfolding algorithms that corrects for the detector effects.

8.4 Summary of the Gap Finding Algorithms

The algorithm for reconstruction of rapidity gaps in the ATLAS detector is summarized here. An inclusive forward rapidity gap finding algorithm proceeds as follows for every event:

- The pseudorapidities of all good tracks with $p_T > 200$ MeV are recorded.
- The pseudorapidities of the center of gravity of clusters satisfying $p_T > 200$ MeV are also recorded if the cluster contains one or more cell(s) above significance threshold $S_{\text{th}}(\eta)$. The cells in the Tile calorimeter are ignored.
- Forward gap size, $\Delta\eta^F$, is calculated from each side of the detector starting at $\eta = \pm 4.9$ and finishing at the first object which meets either of the above requirements. The size of the larger of the two gaps is $\Delta\eta^F$.

The algorithm for reconstruction of 2-dimensional floating gap does not use calorimeter clusters and works with cells only. This algorithm was used for estimation of diffractive fraction by fitting MC templates to data as it will be discussed in the next chapter. There is no need to match detector level with particle generator level, therefore information about real particle energy is not required. The 2-dimensional floating gaps are reconstructed as follows:

- The pseudorapidity of all good tracks with $p_T > 200$ MeV are recorded.
- The pseudorapidity of the cells above significance threshold $S_{\text{th}}(\eta)$ are also recorded. The cells in the Tile calorimeter are ignored.
- A given η -slice is deemed to contain particle activity if it contains object which meets either of the above requirement.
- The largest consecutive sequence of η -slices containing no particle activity is identified as floating rapidity gap, $\Delta\eta$.

Chapter 9

Description of Minimum Bias Data in MC Generators

The measurements presented in the next chapters rely on the used MC generators. In order to determine diffractive fractions, MC templates of rapidity gaps distributions are fitted to data. The result of the fit strongly depends on the MC model. Furthermore, for rapidity gap cross section, the result has to be corrected for detector effects in order to be useful for community outside the ATLAS collaboration. These corrections are also made using the MC generators and introduce some model dependence into the final result. Therefore, description of various observables related to rapidity gaps in different regimes by PYTHIA6, PYTHIA8 and PHOJET was tested. The purpose of these tests is selection of the generator with the best description of the data that will be used for the data corrections. The rest MCs provide estimation of model uncertainty if they do not exhibit any essential failure in the data description.

9.1 Cluster and Track Distributions

Several inclusive distributions were tested in measurement of charged particle multiplicities [1,85]. Similar distributions were measured in events in which diffractive contribution was enhanced by requirement of single sided hit in the MBTS i.e. only one arm of MBTS detector fired and veto was required in the opposite arm. An important conclusion from the measurement was observation that high p_T and high multiplicity particle production in PYTHIA6 are underestimated. This is a consequence of the missing model for high mass M_X (and M_Y) diffractive production which is included in both PYTHIA8 and PHOJET.

In this section, the multiplicities and transverse momentum distributions of tracks and calorimeter clusters are studied in events with various size of the gap which controls the ratio of diffractive to non-diffractive component. Distributions were made for gap sizes in the following intervals: $0 < \Delta\eta^F < 2$, $2 < \Delta\eta^F < 4$, $4 < \Delta\eta^F < 6$, $6 < \Delta\eta^F < 8$. According the MC

predictions, sample with the smallest gaps, $0 < \Delta\eta^F < 2$, is dominated by the ND contribution while $4 < \Delta\eta^F < 6$, $6 < \Delta\eta^F < 8$ are created almost exclusively by SD and those DD in which hadronic system Y does not reach the calorimeter.

Multiplicities of calorimeter clusters satisfying the noise suppression requirement are shown in left plots of Figure 9.1. The data are almost always bracketed between PYTHIA6 and PYTHIA8 with PHOJET in each rapidity gap interval. All MCs exhibit large disagreement at low multiplicities. Overall, PYTHIA6 underestimates the multiplicity in data while slight overestimation is seen in both PYTHIA8 and PHOJET.

Transverse momentum of the clusters exhibit good agreement with data for all MC. The worst description is obtained by PYTHIA6 which does not agree with data at large rapidity gaps. PYTHIA8 and PHOJET have similar behavior and overestimate data in $2 < \Delta\eta^F < 4$ where PYTHIA6 approximates the data well.

MC description of track multiplicities and transverse momenta reveal exactly the same behavior as in the case of clusters. The distributions are shown in Figure 9.2. In general, PYTHIA8 models the data best and the PYTHIA6 has worst description especially for large gaps.

Many more observables were investigated in the documents [115, 116]. The multiplicities of tracks and clusters were studied at the gap edge which probes the correctness of hadronisation models and test the detector simulation. None of the MC models describes correctly all the observables and each of them agrees or fails in different regimes.

9.2 Forward Energy Flow

An observable which effectively discriminates between diffractive and non-diffractive component is a sum over the energy plus (minus) longitudinal momentum of all particles, $\sum(E \pm p_z)$. In SD events, this sum approximately corresponds to twice the Pomeron energy: plus (minus) sign corresponds to proton emitting the pomeron in the positive (negative) z direction.

The $\sum(E + p_z)$ resp. $\sum(E - p_z)$ were reconstructed from the default calorimeter clusters. Only cluster from the A resp. C side of the FCal calorimeter were used in order to enhance the diffractive contribution at small $\sum(E + p_z)$. The $\sum(E + p_z)$ distributions are shown in Figure 9.3 for data, PYTHIA6, PYTHIA8, and PHOJET. The region of small $\sum(E + p_z)$ is quite well modeled by all MCs. PHOJET slightly underestimates the data due to high non-diffractive fraction. On the other hand, both PYTHIA8 and PYTHIA6 are above the data. All MCs fail to describe large $\sum(E + p_z) > 20 \text{ GeV}$ where they exhibit larger bump than present in the data. This suggests that MC models have too large energy flow in forward direction.

9.3 Summary

The multiplicities and transverse momentum of tracks and topological clusters were studied in PYTHIA6, PYTHIA8, and PHOJET and compared to data. None of the MC does describe correctly all the observables. Usually the data lies between the PYTHIA6, which underestimates the multiplicity and large transverse momentum in events with large rapidity gaps, and PYTHIA8 with PHOJET which exhibit similar behavior. The $\sum(E \pm p_z)$ distributions suggest that the normalizations of non-diffractive events is overestimated in PHOJET. Furthermore, the forward energy flow is slightly overestimated in all MCs. From all the tests which can be found in references [115, 116] we choose PYTHIA8 as nominal MC used for unfolding due to slightly better performance compared to PHOJET. Despite of the missing hard component of PYTHIA6 diffractive model, PYTHIA6 cannot be excluded because it bounds data from the other side than PYTHIA8 and PHOJET. Thus both PYTHIA6 and PHOJET are used for evaluation of MC model systematics uncertainty.

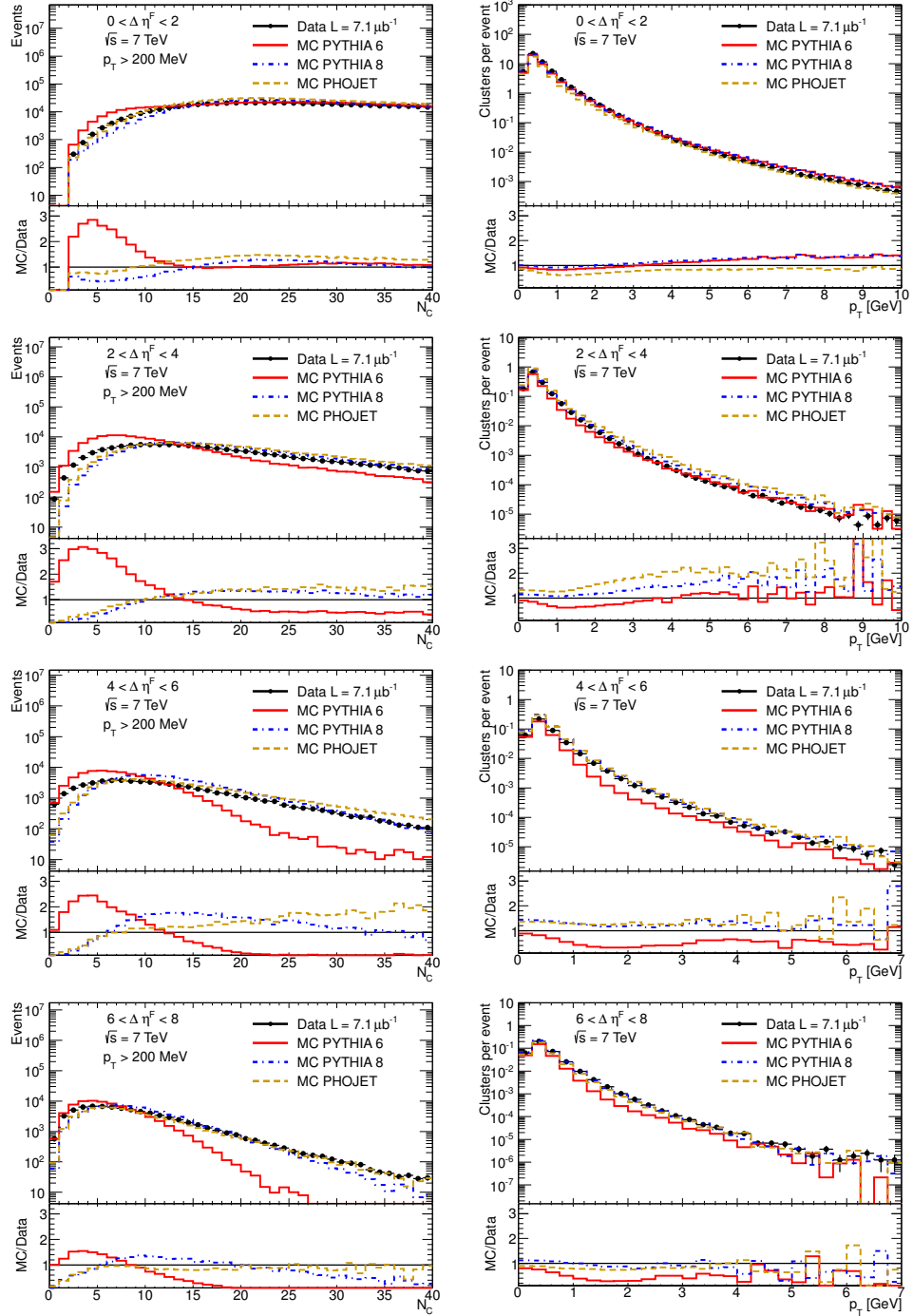


Figure 9.1: Multiplicity of clusters which passed the selection requirements defined in Section 8.4 (left) and transverse momentum of all clusters (right) in events with gap size: $0 < \Delta\eta^F < 2$, $2 < \Delta\eta^F < 4$, $4 < \Delta\eta^F < 6$, $6 < \Delta\eta^F < 8$.

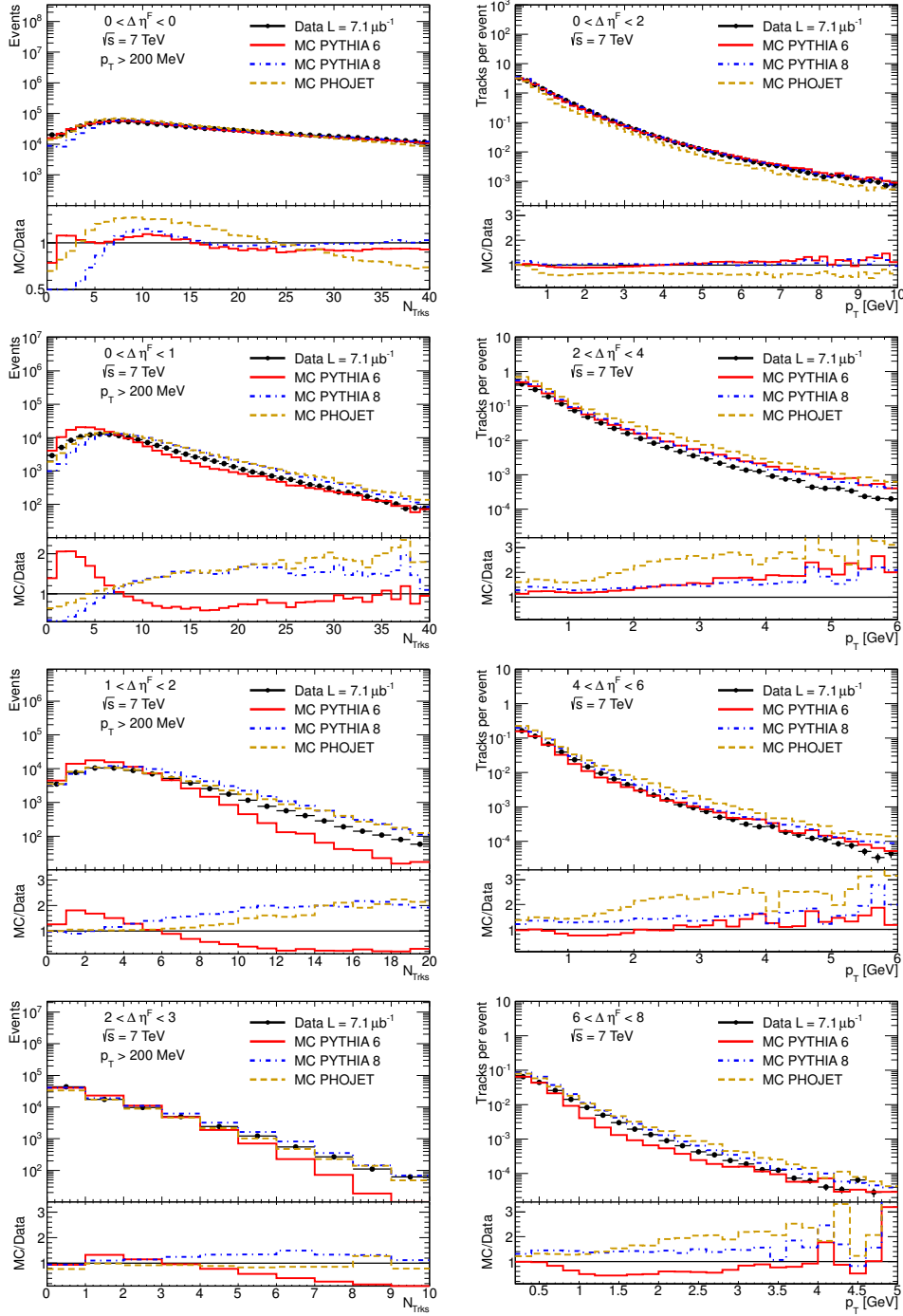


Figure 9.2: Multiplicity (left) and transverse momentum (right) of tracks which passed the selection requirements defined in Section 8.4 in events with gap size: $0 < \Delta\eta^F < 2$, $2 < \Delta\eta^F < 4$, $4 < \Delta\eta^F < 6$, $6 < \Delta\eta^F < 8$.

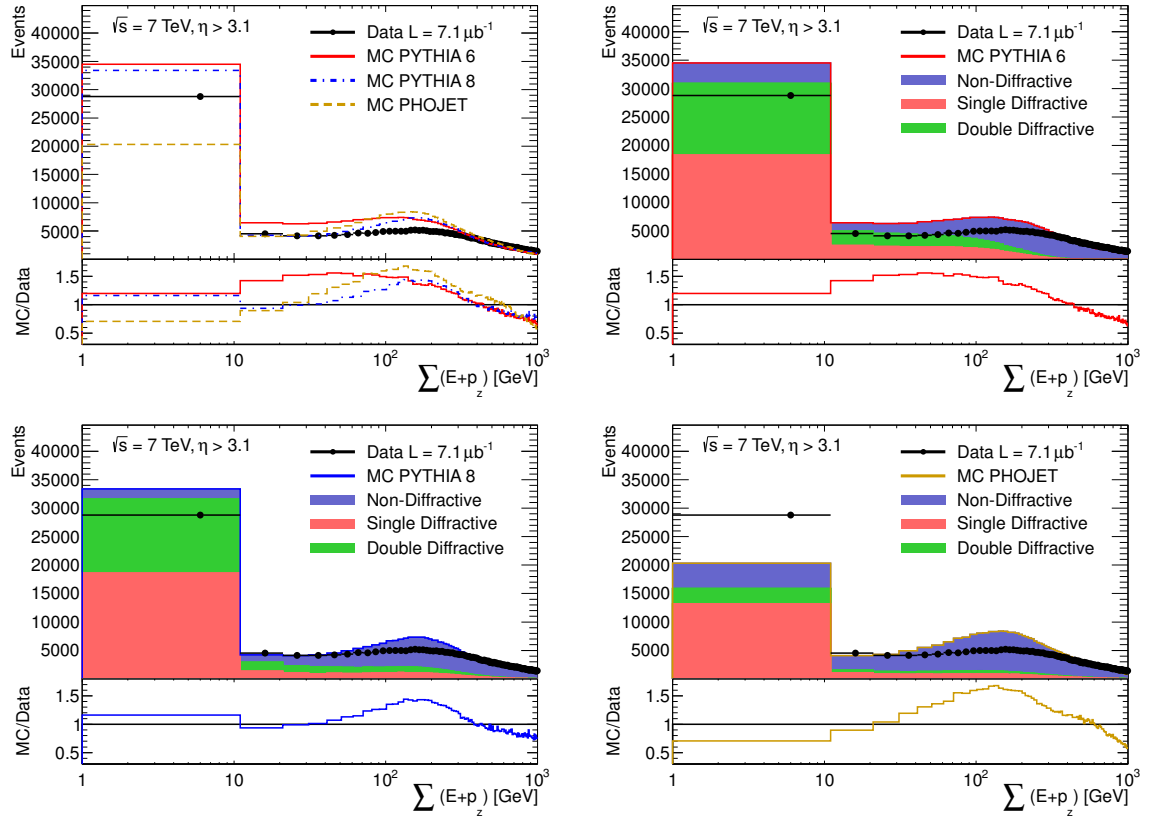


Figure 9.3: $\sum(E + p_z)$ distribution computed from calorimeter clusters in the FCal at $\eta > 3.1$. Data are compared with PYTHIA6, PYTHIA8, and PHOJET predictions. Relative contribution of ND, SD and DD components are shown for each MC.

Chapter 10

Diffractive Fractions in Total Inelastic Cross Section

The diffractive processes contribute significantly to the total inelastic cross section at LHC energies. The MC models predict that diffractive component constitutes about 20 - 30% of the total inelastic cross section at $\sqrt{s} = 7$ TeV, see Table 6.1.

ATLAS measured this fraction using the MBTS detector. The diffractive sample was enhanced by the requirement that only one arm of the MBTS trigger is hit and the other does not detect any particle activity. The measured ratio of these single sided events to all events triggered by MBTS_1 was $R_{ss} = 10.02 \pm 0.03(\text{stat.})_{-0.4}^{+0.1}(\text{syst.})\%$. The R_{ss} as a function of diffractive fraction f_D was evaluated using different MC models shown in Figure 10.1. The diffractive contribution corresponding to the measured R_{ss} is about $f_D \sim 27\%$ according to MC models. The value obtained by the default Donnachie-Lanshoff model of $\alpha_p(t) = 1.085t + 0.25 \text{ GeV}^2$ in PYTHIA8 for events inside kinematic range of detector acceptance corresponding to $\xi_X > 5 \times 10^{-6}$ is $f_D = 26.9_{-1.0}^{+2.5}\%$.

In this chapter, a novel method to estimate diffractive fractions based on the floating gap distribution is introduced. An advantage of the method is a possibility of separation of SD and DD events. This is motivated by the fact that SD events should create gaps starting from the edge of the detector while large fraction of DD produce gaps in central region. Moreover, wider rapidity coverage of the calorimeter should make the measurement less model dependent.

The estimation of the ND, SD and DD contributions is done by a fit of floating gap templates generated by PYTHIA6, PYTHIA8, and PHOJET to data. The templates produced by PYTHIA8 are displayed in Figure 10.2. ND processes produce small gaps randomly distributed in the detector, SD events produce large gaps starting from the edge of the detector $\eta = \pm 4.9$ and DD produce large gaps everywhere inside the detector.

Due to completely different shape of templates, the diffractive to non-diffractive ratio can be well estimated by the fit. As it will be shown later, the result has small dependency on the MC

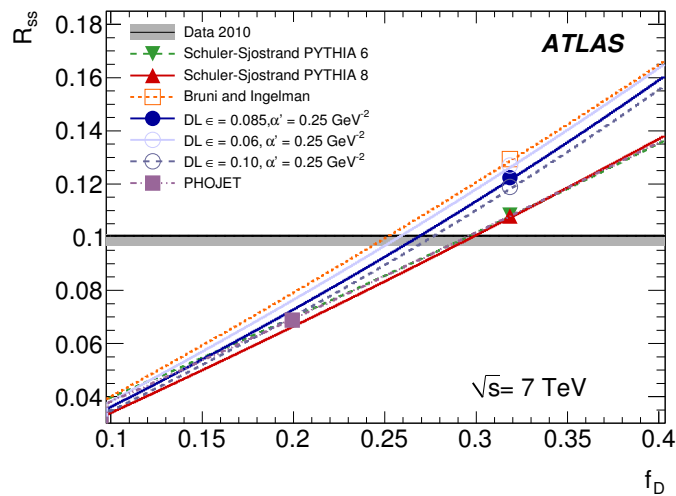


Figure 10.1: The ratio of the single-sided to inclusive event sample, R_{ss} as a function of the fractional contribution of diffractive events to the inelastic cross-section f_D predicted by different MC models. The data value for R_{ss} is shown as the horizontal line with its systematic uncertainties (grey band). Figure is taken from ref. [3].

model and it is compatible with measurement of single sided events using the MBTS detector [3]. However, the estimation of SD to DD ratio is more complicated. Due to small pseudorapidity coverage of the detector a large fraction of DD events mimics the SD event topology and their corresponding templates differ only slightly. The DD template contains large fraction of events having gap starting from the $\eta = \pm 4.9$. Thus, in order to obtain stable fit result, these two templates need to be redefined. The obtained ratio of these redefined templates strongly depends on the MC model therefore the result is interpreted as tuning of fractions in the MC generators. The results of this chapter has been published in the ATLAS public document [117]. However, due to the already mentioned complications systematic uncertainties were not finalized into the form of the rapidity gaps inelastic cross section presented in Chapter 11.

10.1 Event Selection

Data used in this analysis were collected during the first LHC run 152166 at $\sqrt{s} = 7$ TeV in April 2010. Only events in which the calorimeter systems and the Inner Detector tracker were fully functional were used. MBTS_1 trigger was used to collect events from colliding proton bunches. The recorded data sample corresponds to integrated luminosity of 7339 mb^{-1} at $\sqrt{s} = 7$ TeV and the number of events collected by the MBTS_1 trigger was 436687.

In order to reduce the electronic noise from MBTS which is well modeled by a Gaussian with 0.02 pC [118], the events are further required to have at least two hits in the MBTS after offline reconstruction above threshold of 0.15 pC .

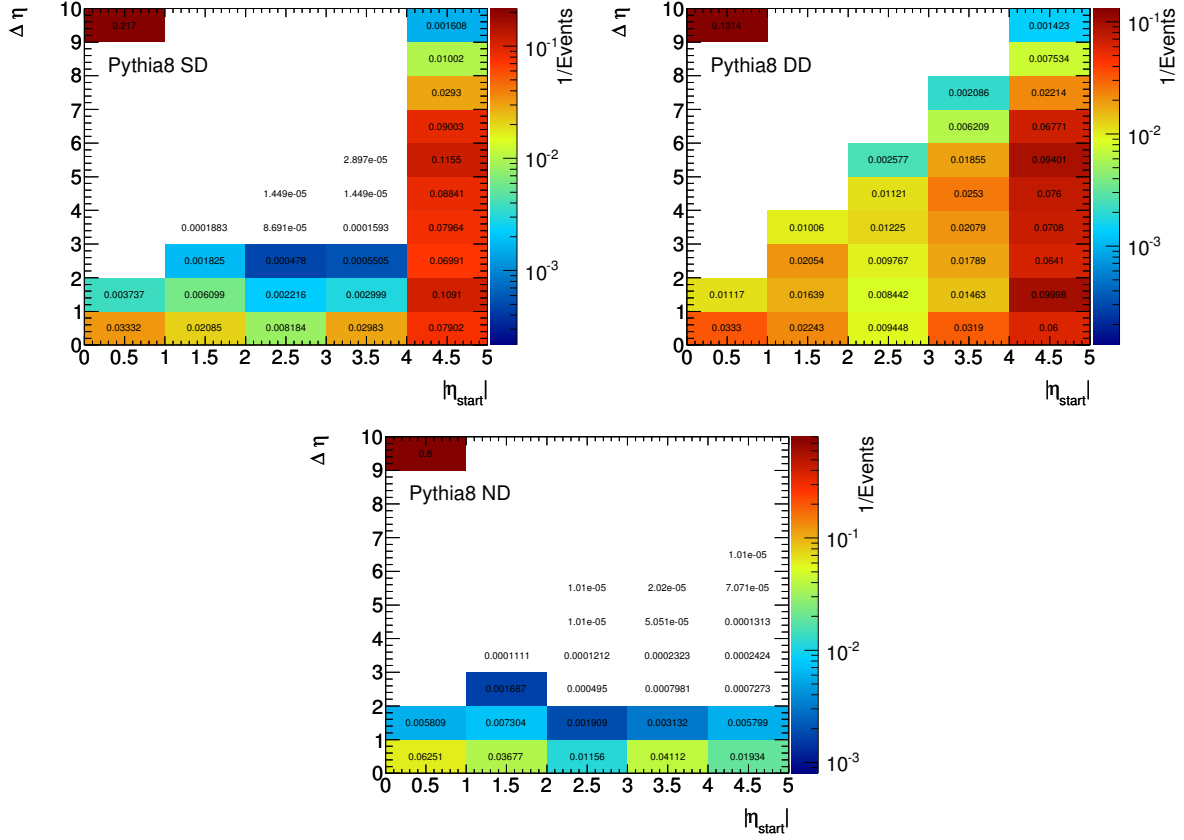


Figure 10.2: Detector level correlation in PYTHIA8 between start position $|\eta_{\text{start}}|$ and size $\Delta\eta$ for SD, DD, ND contributions. The bin $(|\eta_{\text{start}}|, \Delta\eta)=(0, 10)$ contains events with no gap found.

Different MBTS response in data and MC was fixed applying different thresholds in the MC. The outer counters require a threshold of 0.28 pC (0.26 pC) on the A (C) side, while 0.32 pC and 0.38 pC are used in the inner counters for A and C side respectively [118].

10.2 Estimation of Beam Induced Background

Interactions of the beam particle with the residual beam gas inside the detector or outside the beam cavern (beam halo) influence the rapidity gap distribution distributions in data. These effects are not simulated in the MC samples and needs to be removed from the data. Introducing the cuts on the number of tracks or vertices would bias the distributions towards smaller gap sizes therefore the rapidity gap distribution created by induced beam background needs to be extracted from data and statistically subtracted from signal distributions.

Pure beam background sample of floating rapidity gap distribution is obtained from the events of unpaired bunches using the MBTS offline selection of at least two hits above the thresholds. This sample needs to be properly normalized to data sample obtained from colliding bunches with the same MBTS selection. The normalization factor is determined from a comparison of

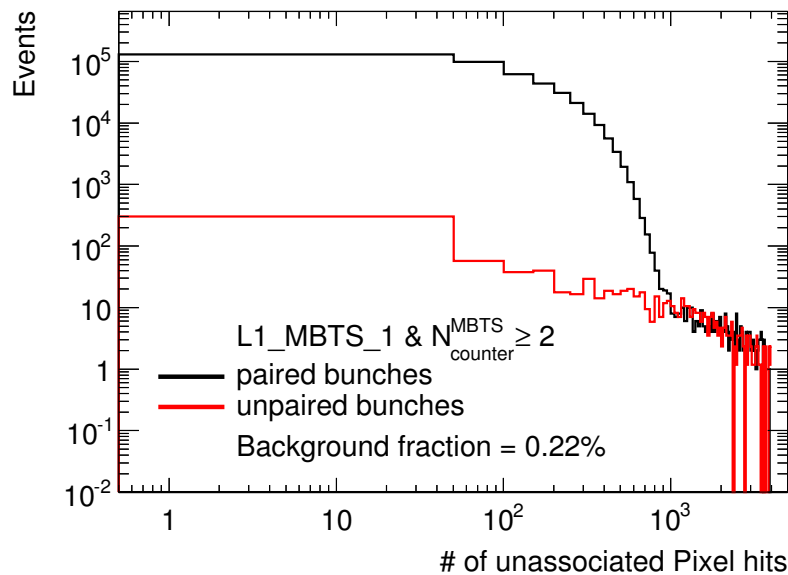


Figure 10.3: Number of unassociated hits in the Pixel detector observed in the sample selected with MBTS_1 in events with colliding bunches and with unpaired bunches. The background distribution was normalized to signal by number of events with more than 10^3 unassociated hits.

unassociated hits in the Pixel detector between events from colliding and unpaired bunches. The beam gas events typically produce charged particle boosted into very forward direction what makes the tracks less likely to be found and leaves high number of unassociated hits in the Pixel detector. Thus the normalization factor is obtained from match of the tails of unassociated hits distributions as it is illustrated in Figure 10.3.

Floating gap distribution for normalized beam background sample and data sample before background subtraction are presented in Figure 10.4. The contamination of beam background events in the data sample was estimated to 0.22% using this method. The beam background contamination with requirement of at least two offline hits is about a factor of 10 smaller compared to the sample selected with at least one offline MBTS hit.

The above procedure does not correct for events in which the physics signal was in coincidence with the beam background that modifies the rapidity gap distribution but does not fire the MBTS. The probability that there will be some activity when beam passes without the MBTS requirement is conservatively smaller than $< 10^{-4}$, hence this background is neglected.

10.3 Reorganization of MC Templates

It is difficult to distinguish DD events at small ξ_Y^1 from SD events because for $\xi_Y \leq 10^{-6}$ the Y system is produced entirely outside the acceptance of the calorimeter $|\eta| > 4.9$. Thus DD mimics

¹The notation $\xi_X > \xi_Y$ introduced in Section 4.2 is used.

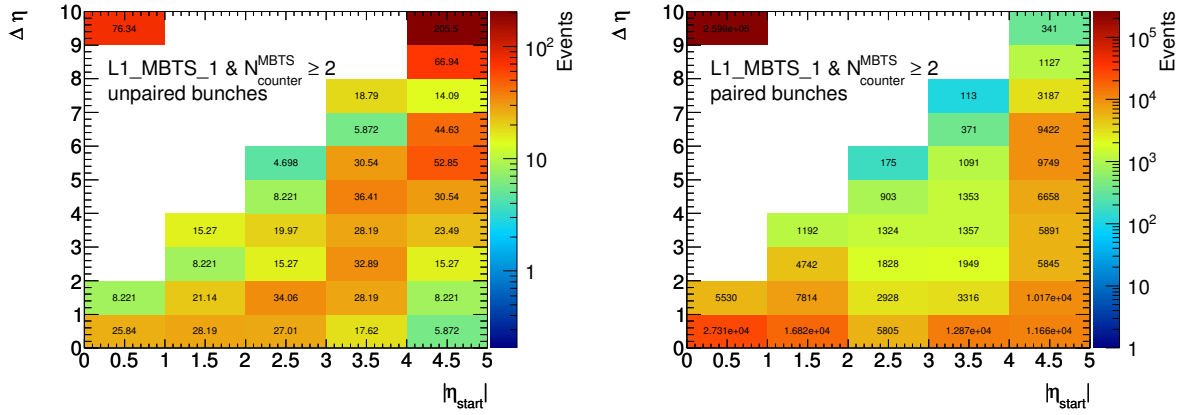


Figure 10.4: Background distributions used for background subtraction (left) and the signal distribution before subtraction (right) as a function of floating gaps $\Delta\eta$ vs. $|\eta_{\text{start}}|$. The background distributions are scaled by a factor of 1.17.

$\sqrt{s} = 7 \text{ TeV}$			
Contribution	PYTHIA 6	PYTHIA 8	PHOJET
SD-Like	28.8%	29.4%	17.0%
DD-Like	3.3%	2.7%	1.9%
ND	67.9%	67.9%	80.8%
SD-Like in DD	74.2%	79.3%	63.4%
DD-Like in DD	25.8%	20.7%	36.6%

Table 10.1: Predicted fractions for PYTHIA6, PYTHIA8 and PHOJET for SD-like defined at hadron level with $\xi_Y < 10^{-6}$ and DD-like fractions defined as $\xi_Y > 10^{-6}$. For convenience, also the SD-like fraction in DD template are given.

the SD topology where the largest gap extends to the limits of the calorimeter acceptance. The fraction of DD events for which both diffractive masses M_X and M_Y are sufficiently large and tend to produce large rapidity gaps in the central region of the detector, bounded by activity at both edges of the acceptance, is predicted by MC generators to be small, about 20-37%. It is therefore convenient to reclassify the DD channel, based on the size of the smaller diffractive system ξ_Y . DD events with both $\xi_X \geq 10^{-6}$ and $\xi_Y \geq 10^{-6}$, which typically leave a central pseudorapidity gap within the detector acceptance are reclassified as 'DD-like'. DD events with $\xi_X \geq 10^{-6}$ and $\xi_Y \leq 10^{-6}$ are reclassified for the purpose of fitting as 'SD-like' and are combined with the SD template. The effect of this reclassification is illustrated in Figure 10.5, which shows the correlation between the size of the two diffractive systems in PYTHIA8 DD events. Numerically, the default fractions of the inelastic cross section in PYTHIA (PHOJET) are 29% (24%) categorized as SD-like and 3% (2%) as DD-like, see Table 10.1.

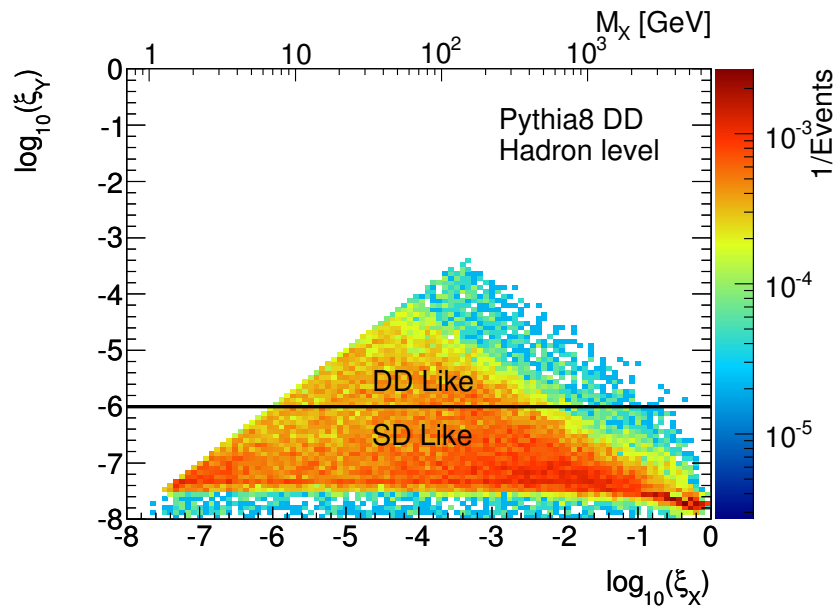


Figure 10.5: Kinematic plane of $\log_{10}(\xi_X)$ vs. $\log_{10}(\xi_Y)$ for double diffractive events according to PYTHIA 8. Events with $\xi_Y < 10^{-6}$ are re-classified as single-diffractive-like events for the fitting procedure.

10.4 Fit Procedure

The three MC templates for ND, SD-like, DD-like processes normalized to unity are illustrated in Figure 10.7. The template for data after statistical subtraction of beam background contribution is presented in the same figure. To determine fractions of ND, SD-Like, DD-Like in inelastic cross section, the MC templates are fitted to data. More exactly, the normalizations f_{ND} , $f_{\text{SD-like}}$, $f_{\text{DD-like}}$ of ND, SD-like, and DD-like templates $T_{\text{ND}}(x_{i,j})$, $T_{\text{SD-like}}(x_{i,j})$, $T_{\text{DD-like}}(x_{i,j})$

$$T_{\text{MC}}(x_{i,j}) = f_{\text{ND}}T_{\text{ND}}(x_{i,j}) + f_{\text{SD-like}}T_{\text{SD-like}}(x_{i,j}) + f_{\text{DD-like}}T_{\text{DD-like}}(x_{i,j}) \quad (10.1)$$

$$1 = f_{\text{ND}} + f_{\text{SD-like}} + f_{\text{DD-like}} \quad (10.2)$$

are obtained from a fit of $T_{\text{MC}}(x_{i,j})$ to data $T_{\text{Data}}(x_{i,j})$. Indices i, j run over $(|\eta_{\text{start}}|, \Delta\eta)$ bins. The MC templates include MBTS offline selection and each of them is normalized by the number of events on the hadron level. Since our statistics in generated MC samples is comparable to data, both MC and data statistical errors need to be taken into account. The fitting procedure proceeds in two steps. First the $\chi^2 = \sum_{i,j} (T_{\text{Data}}(x_{i,j}) - T_{\text{MC}}(x_{i,j}))^2 / \sigma_{i,j}^2$ is minimized to obtain fraction seeds. $\sigma_{i,j}$ denote the statistical error in particular bins for both MC templates and data summed in squares. In the next step, the fractions are obtained using Logarithm-Likelihood (LL) fit. The two step procedure helps the LL to avoid local minima and makes the fit quicker

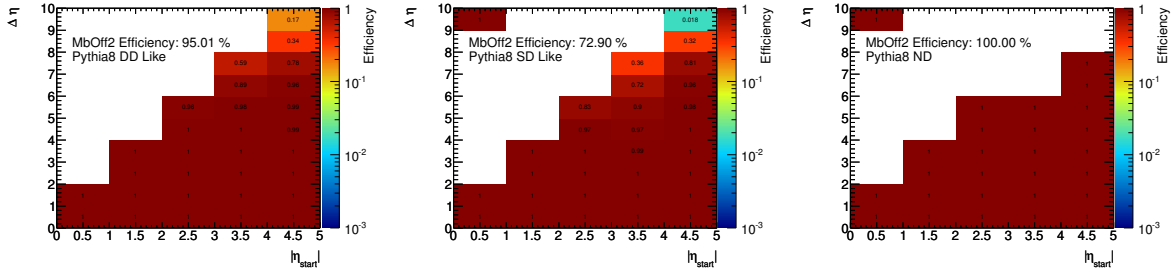


Figure 10.6: MBTS_1 and $N_{\text{counter}}^{\text{MBTS}} > 2$ selection efficiency as a function of gap size $\Delta\eta$ and start of the gap $|\eta_{\text{start}}|$ estimated from PYTHIA8.

as it already starts from a point close to an functional extreme. For the LL, the function

$$\ln L(f_{\text{ND}}, f_{\text{SD-like}}) = \sum_{i,j} T_{\text{Data}}(x_{i,j}) \ln T_{\text{MC}}(x_{i,j}) - T_{\text{MC}}(x_{i,j}) + \sum_{i,j} \sum_{k=1,2} a_{i,j,k} \ln A_{i,j,k} - A_{i,j,k} \quad (10.3)$$

is maximized. The additive term $\sum_{i,j} \sum_{k=1,2} a_{i,j,k} \ln A_{i,j,k} - A_{i,j,k}$ stands for statistical error in MC with predicted $A_{i,j,k}$ and generated $a_{i,j,k}$ number of events in bin (i, j) of template T_k ($k = 2: T_{\text{ND}} - T_{\text{DD-like}}$, and $T_{\text{SD-like}}$). Such method is implemented in the `TFractionFitter` package in `ROOT` which is used here. More detailed information can be found in [119].

For both data and MC, only the gaps satisfying $-|\eta_{\text{start}}| + \Delta\eta \leq 2$ that do not span over the MBTS acceptances are considered in the fit. In principle, larger gaps are in contradiction with the gap definition since MBTS had to fire to register the event implying large corrections in bins which stretch over the MBTS acceptance. Observation of these large gaps can happen as the calorimeter energy thresholds are not zero and MBTS information is not included in the gap searching algorithm. The MBTS selection efficiency as a function of rapidity gap size $\Delta\eta$ and start of the rapidity gap $|\eta_{\text{start}}|$ is presented in Figure 10.6.

	$\sqrt{s} = 7 \text{ TeV}$		
Process	PYTHIA6	PYTHIA8	PHOJET
ND	99.9%	100.0%	100.0%
SD-Like	71.6%	72.9%	77.5%
DD-Like	94.9%	95.0%	96.7%

Table 10.2: MBTS offline selection $L_1_MBTS_1$ & $N_{\text{counter}}^{\text{MBTS}} \geq 2$ efficiency for PYTHIA6, PYTHIA8, and PHOJET.

The fitted fractions are then corrected for the overall MBTS selection efficiency obtained from MC for ND, SD-like, and DD-like contributions in the $(|\eta_{\text{start}}|, \Delta\eta)$ bins used in the fit. They are summarized in Table 10.2 for different MC generators. The overall MBTS selection efficiencies ε_{ND} , $\varepsilon_{\text{SD-Like}}$, $\varepsilon_{\text{DD-Like}}$ for ND, SD-like and DD-like events respectively were applied

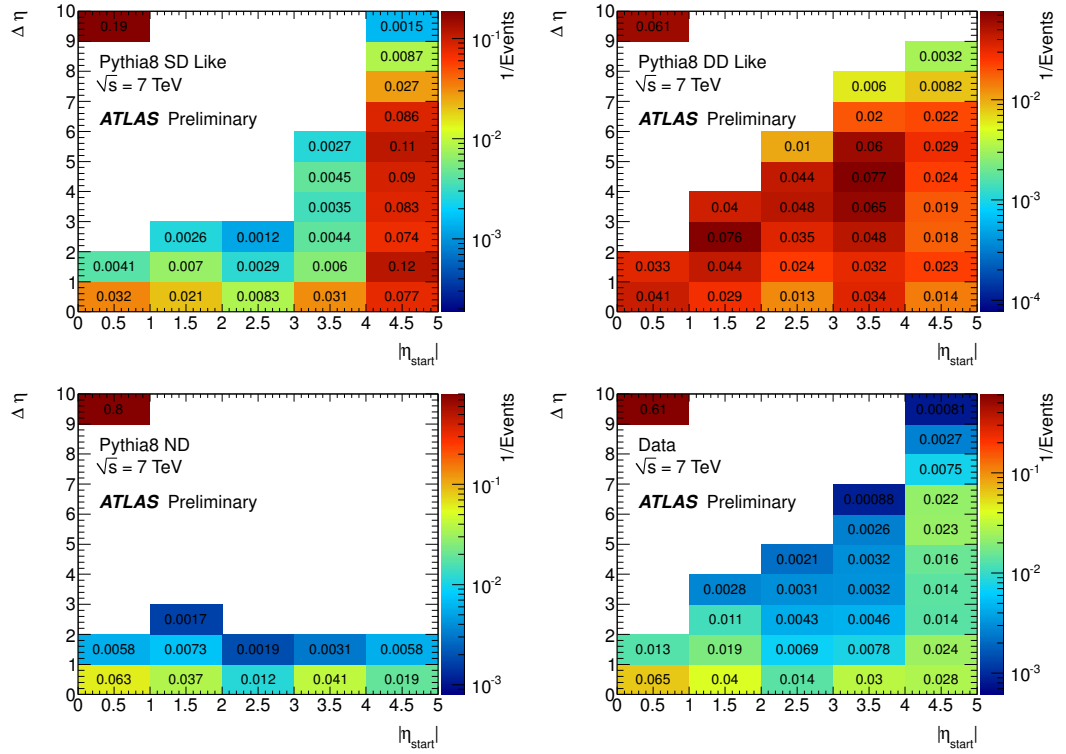


Figure 10.7: Reorganized SD-Like, DD-Like and ND templates predicted in PYTHIAS and the template observed in data. The bin $(|\eta_{\text{start}}|, \Delta\eta)=(0, 10)$ contains events with no gap found.

as the normalization factors:

$$N = f_{\text{ND}}/\varepsilon_{\text{ND}} + f_{\text{SD-like}}/\varepsilon_{\text{SD-like}} + f_{\text{DD-like}}/\varepsilon_{\text{DD-like}}, \quad (10.4)$$

$$f_{\text{ND}}^{\text{CORR}} = f_{\text{ND}}/(N \times \varepsilon_{\text{ND}}), \quad (10.5)$$

$$f_{\text{SD-like}}^{\text{CORR}} = f_{\text{SD-like}}/(N \times \varepsilon_{\text{SD-like}}), \quad (10.6)$$

$$f_{\text{DD-like}}^{\text{CORR}} = f_{\text{DD-like}}/(N \times \varepsilon_{\text{DD-like}}). \quad (10.7)$$

The fitting procedure of the different contributions of the inelastic cross section on MC has been tested on pseudo-data samples. In particular, PYTHIAS has been treated as pseudo-data and fitted using different generators. When PYTHIAS templates are used, the fitted fractions correspond exactly to the default ones in the MC. Using other generators, the obtained ND fractions are consistent with a reasonable accuracy, but the SD-like and DD-like contributions depend largely on the input fractions in the MC generators used in the template. The conclusion from the closure tests is that only the overall fraction of diffractive events f_D is reliably determined and considered as an independent measurement, while the SD-like and DD-like fraction are considered only as Monte Carlo models tunes.

Corrected	Logarithm likelihood		
	PYTHIA6	PYTHIA8	PHOJET
ND (%)	72.0 ± 0.3	69.8 ± 0.3	70.3 ± 0.4
SD-Like (%)	25.2 ± 0.2	21.3 ± 0.2	23.5 ± 0.2
DD-Like (%)	2.9 ± 0.1	8.9 ± 0.2	6.2 ± 0.1
χ^2/NDof	28.9	134.4	74.9

Table 10.3: Fit of PYTHIA6, PYTHIA8 and PHOJET templates to data. The result is corrected for the offline MBTS selection.

10.5 Fit Results

Results of the fit of ND, SD-like and DD-like templates to data for PYTHIA6, PYTHIA8 and PHOJET are summarized in Table 10.3. Measured fractions of non-diffractive component of the inelastic cross sections are $72.0 \pm 0.3\%$ for PYTHIA6, $69.8 \pm 0.3\%$ for PYTHIA8, and $70.3 \pm 0.4\%$ for PHOJET. Fit of the PYTHIA6 templates gives the best agreement with data with $\chi^2/\text{NDof} = 30$ while the fits of PYTHIA8 and PHOJET templates give $\chi^2/\text{NDof} = 135$ and $\chi^2/\text{NDof} = 75$, respectively. Moreover, fitted SD-like and DD-like by PYTHIA6 are in better agreement with its predicted fractions than PYTHIA8 and PHOJET. All generators give similar results for ND fractions within 3% but the ratio of SD-like to DD-like fractions varies from 8.3, obtained by PYTHIA6, to 2.3, obtained by PYTHIA8.

Error included in Table 10.3 contains only statistical contribution. The following systematics uncertainties were included into the final error:

- **Threshold:** The uncertainty reflects the sensitivity of the result on the choice of significance threshold applied on the calorimeter cells. Significance $S_{\text{th}}(\eta)$ was varied by 10% in both data and MC samples. The effect on final result in the diffractive fraction is $< 0.3\%$. This small sensitivity justifies the noise suppression treatment.
- **Energy scale:** A $\pm 25\%$ scale uncertainty is considered for all cell energy measurements. This large value reflects the limited knowledge of the calorimeter response and linearity at small energy values to which the rapidity gap thresholds correspond. Moreover, it contains uncertainty on amount of material budget in front of the calorimeter, especially in the forward region. Uncertainty of $\pm 25\%$ has been estimated as conservative value for the case of preliminary result on diffractive fraction. Better constrain of energy scale uncertainty was estimated by combination of $Z \rightarrow e^+e^-$ data [120] and $\pi^0 \rightarrow \gamma\gamma$ decays measurement [121] which provide estimate of electromagnetic energy scale. The hadronic energy scale was determined from calorimeter tests beams. Obtained values were used for measurement of inelastic differential cross section as a function of rapidity gap size and they

MC	PYTHIA6		PYTHIA8		PHOJET	
	down var.	up var.	down var.	up var.	down var.	up var.
Uncertainty (%)						
Statistical	-0.3	+0.3	-0.3	+0.3	-0.4	+0.4
Threshold $\pm 10\%$	-0.1	+ 0.1	-0.1	+0.1	-0.2	+0.2
Energy scale $\pm 25\%$	-3.8	+ 3.8	-3.8	+3.8	-3.8	+3.8
MC difference	-2.2	+ 0.0	-0.0	+2.2	-0.5	+1.7
Total	-4.5	+3.8	-3.8	+4.5	-3.8	+4.2

Table 10.4: Systematic uncertainty of non-diffractive fraction for different MC models.

will be discussed in the next chapter. Furthermore, the variation of energy scale requires to vary signal from particle energy deposits but leave the cell noise unchanged. This technical complication requires redoing the detector simulation of the MC samples. Thus it was approximated in the preliminary results by the following approach. Both calorimeter noise and cell response on physics was decreased in the offline analysis by 25% and the obtained MC templates were fitted to data. The obtained uncertainty for down variation of energy scale was symmetrized with respect to the nominal value to approximate up variation of energy scale. The symmetrization was done in order to avoid a large overestimation of energy scale due to reaching the noise peak i.e. if the noise is increased by 25% the cut $S_{\text{th}}(\eta)$ is too low to remove the noise this cannot happen in the correct energy scale treatment where the noise remains the same and only the response on the physics is varied. This would completely remove events with large gaps from the rapidity gap spectrum.

The systematic uncertainty is dominated by energy scale uncertainty. All the systematic uncertainties on the measurement of non-diffractive fraction are summarized in Table 10.4.

10.6 Summary

Diffractive to non-diffractive ratio has been obtained by means of a Log-Likelihood fit of ND, SD-like, and DD-like templates to data. The diffractive fraction in the data has been measured $f_{\text{D}} = 1 - f_{\text{ND}} = 30.2 \pm 0.3$ (stat.) ${}_{+4.5}^{-3.8}$ (syst.)% using PYTHIA8. The systematic uncertainty includes all considered systematics added in quadrature. They are summarized in Table 10.4. The obtained diffractive fraction f_{D} is in good agreement with the ATLAS result obtained in the analysis with enhanced diffractive contribution using MBTS veto where the measured central values and corrected using various three models are 28.0% for PYTHIA6, 30.2% for PYTHIA8, and 29.7% for PHOJET [3]. However, the dependency on the MC model was not improved with respect to the MBTS measurement as it was originally expected.

The SD-like/DD-like ratio is poorly constrained due to the limited detector η coverage, MC model and energy scale uncertainty. Even though, the energy scale uncertainty could be reduced,

using the method introduced in Section 11.3.1, the result strongly depends on the MC generator. The determined fractions are therefore tightly linked to the generator and can be considered for tuning of the MC only.

From the above reasons the obtain result was not published by the ATLAS collaboration. It was presented at conferences [117] only as preliminary result. Consequently, the systematic uncertainties are only preliminary and with further work they could be redone according to Section 11.3.

Chapter 11

Forward Rapidity Gap Production

Phenomenological models used for description of inclusive diffraction requires more data, especially from hadron-hadron scattering experiments, in order to be more tightly constrained. Ideally, this could be done by direct measurement of diffractive cross section as a function of ξ and t variables what is possible only with proton taggers. These detectors can measure position of intact diffractive protons in the beam pipe but they were not available during the first years of the LHC run. Moreover, the ξ cannot be reconstructed from the mass of dissociated systems due to small ATLAS detector coverage. As was already discussed in Section 9.2, it is possible to constrain the diffractive models by measurement of $\sum(E + p_z)$ observable which is sensitive to ξ . This was done by CMS collaboration [122, 123].

An alternative is a measurement of inelastic cross section as a function of rapidity gap size which is strongly correlated with the variables ξ_X and ξ_Y . In case of SD, the relation takes form (4.23) and it is valid up to the hadronisation effects as illustrated in Figure 11.1. The figure shows correlation between proton momentum fraction loss ξ_X and the pseudorapidity of the most forward particle, $\eta_{\text{forward particle}}$, in diffractive system X . Furthermore, it is visible that the rapidity gap measurement at the ATLAS detector with coverage $|\eta| < 4.9$ probes the ξ_X from 10^{-6} up to 10^{-2} .

Rapidity gaps can be created also in non-diffractive production due to fluctuations in hadronisation. These rapidity gaps are exponentially suppressed with increasing gap size [111]. The measurement of small rapidity gaps can test the hadronisation and underlying event models.

This chapter presents the ATLAS measurement of inelastic differential cross section as a function of forward rapidity gap size, $\Delta\eta^F$, for particles with $p_T > 200, 400, 600, 800$ MeV defined in Section 8.4. The distributions are corrected for detector effects to level of stable hadrons. The analysis can be found in ATLAS publication [124].

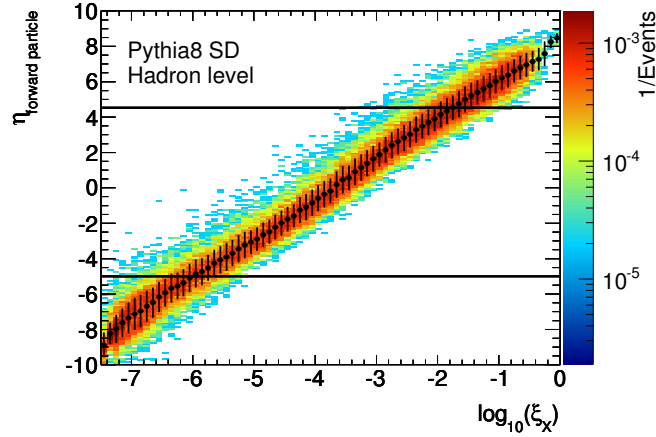


Figure 11.1: Correlation between ξ_X of the diffractive system X in SD reaction $p \rightarrow pX$ and the pseudorapidity of leading particle in the event in PYTHIA8. Events with initial protons coming from negative z are plotted only. Black markers and error bars denote the mean and RMS spread of the generator level gap as a function of the reconstructed gap size.

11.1 Data Selection and Detector Distribution

The measurement of forward rapidity gap distributions were done with the first LHC run 152166 at $\sqrt{s} = 7$ TeV. The data were selected with exactly the same requirements as for the measurement of diffractive fractions thus reader is referred to Section 10.1.

The uncorrected data distribution as a function of forward rapidity gap size, $\Delta\eta^F$, is compared with predictions of the PYTHIA and PHOJET generators in Figure 11.2. All important features of rapidity gap distribution can be read directly from the uncorrected distribution. An exponentially falling spectrum, typical for non-diffractive events, is visible at small gaps, $\Delta\eta^F < 2$. This is followed by a plateau which spans from $\Delta\eta^F = 3$ to $\Delta\eta^F = 8$ which is expected for diffractive production. The decrease in the spectrum for $\Delta\eta^F > 8$ is due to low MBTS selection efficiency. The MC models reasonably describe the data. PYTHIA6 and PYTHIA8 have better agreement at small gaps while PHOJET models better large gaps.

11.2 Corrections for Experimental Effects

The following section presents set of corrections applied to the measured forward rapidity gap distribution in order to obtain the differential cross section as a function of forward rapidity gaps

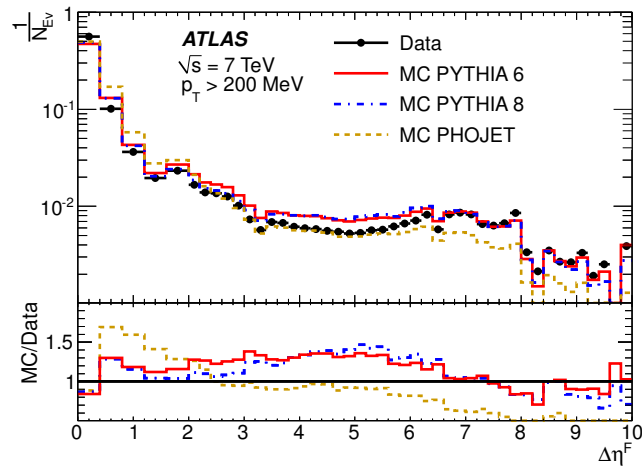


Figure 11.2: Forward rapidity gap distribution for $p_T^{\text{cut}} = 200$ MeV. The final bin at $\Delta\eta^F = 10$ corresponds to cases where no reconstructed particles have $p_T > p_T^{\text{cut}}$.

at the level of stable hadrons. The differential cross section at the detector level¹ is given by

$$\frac{d\sigma(\Delta\eta^F)}{d\Delta\eta^F} = \frac{1}{\text{Bin Size}} \frac{N(\Delta\eta^F) - N_{\text{BG}}(\Delta\eta^F)}{\varepsilon(\Delta\eta^F) \times \mathcal{L}}, \quad (11.1)$$

where $N(\Delta\eta^F)$ is the number of events in the particular *forward gap size* bin $\Delta\eta^F$, $N_{\text{BG}}(\Delta\eta^F)$ is the number of background events, $\varepsilon(\Delta\eta^F)$ is the MBTS offline selection efficiency and \mathcal{L} is the collected luminosity.

The beam background is statistically subtracted from each bin in data. Its distribution is extracted from the unpaired bunches² and appropriately scaled to data using the number of unassociated hits as described in Section 10.2. The $\Delta\eta^F$ distribution of beam background, normalized with respect to data, can be seen in Figure 11.3.

The distribution is then corrected for event selection requiring that MBTS_1 fired and at least 2 offline hits in the MBTS detector, see Section 10.1. Efficiencies of the selection as a function of $\Delta\eta^F$ are taken from the MCs PYTHIA6, PYTHIA8 and PHOJET for cuts $p_T > 200, 400, 600, 800$ MeV. Their distributions are presented in Figure 11.4. For $p_T^{\text{cut}} = 200$ MeV, the efficiency starts to rapidly drop at $\Delta\eta^F = 7$ which corresponds to the end of acceptance of MBTS trigger. Therefore, the results of the measurement are presented only in the range $0 < \Delta\eta^F < 8$ in which the trigger efficiency is greater than 50%.

The luminosity $\mathcal{L} = 7.1 \mu\text{b}^{-1}$ has been measured using the Van-der-Meer beam scanning technique [125].

The detector level distribution is unfolded to hadron level using a Bayesian unfolding proce-

¹Detector level denotes the cross section which is not corrected to level of stable hadrons using the unfolding procedure.

²Unpaired bunches denote events where only a single bunch crossed the interaction point.

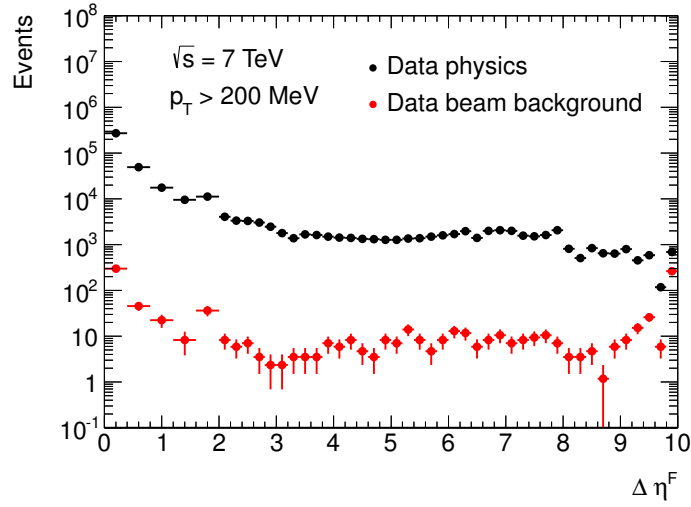


Figure 11.3: Forward gap, $\Delta\eta^F$, distribution for signal before background subtraction and for background normalized with respect to data.

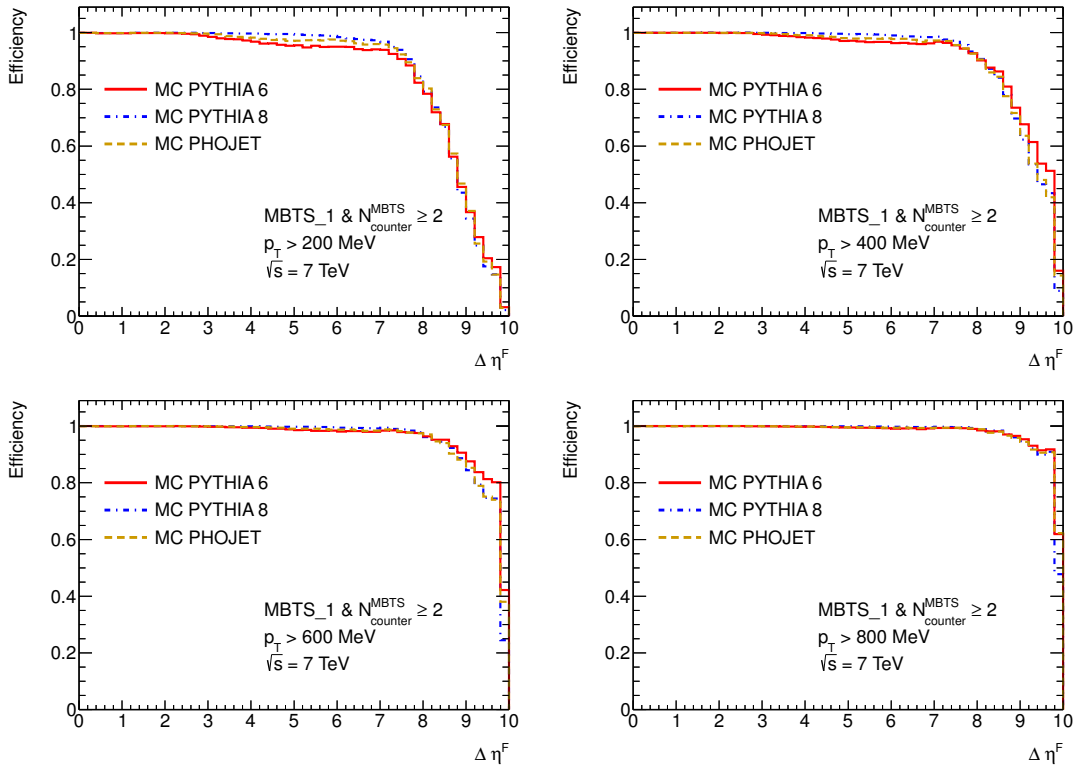


Figure 11.4: MBTS selection efficiencies estimated by PYTHIA6, PYTHIA8 and PHOJET for cuts $p_T > 200, 400, 600, 800$ MeV.

dure [126] to level of stable hadrons with $c\tau < 10$ mm

$$\frac{d\sigma(\Delta\eta^F)}{d\Delta\eta^F} \xrightarrow{\text{unfolding}} \frac{d\sigma(\Delta\eta_{\text{truth}}^F)}{d\Delta\eta_{\text{truth}}^F}. \quad (11.2)$$

The unfolding corrects for the migration in the rapidity gap size between detector and hadron level. The migration matrices used for the unfolding were obtained using MC. PYTHIA8 was chosen as the nominal generator on the bases of the results from Chapter 9 and PYTHIA6 and PHOJET were used for evaluation of the MC model uncertainty. The migration matrices for $p_{\text{T}}^{\text{cut}} = 200, 400, 600, 800$ MeV obtained by PYTHIA8 are shown in Figure 11.5.

In migration matrices with $p_{\text{T}}^{\text{cut}} \geq 600$ MeV anti-diagonal correlations are present. The reason is following, only few particles are usually produced above $p_{\text{T}}^{\text{cut}} = 600$ MeV therefore if some of them are not detected in calorimeter or tracker the side of the detector from which the rapidity gap is reconstructed can be different at the hadron level and truth level. This effect caused unphysical bump around $\Delta\eta^F \sim 5$ in the unfolded cross section. To remove this unphysical behavior, we define the side from which the rapidity gap for $p_{\text{T}}^{\text{cut}} = 400, 600, 800$ MeV is reconstructed to be the same side as for $p_{\text{T}}^{\text{cut}} = 200$ MeV. This definition removes the effect from the final rapidity gap distribution even though the reduced anti-diagonal correlation still persists³ in the unfolding matrices.

In the Bayesian method, several iterations are usually ran to obtain a result independent of the prior i.e. truth spectrum provided by a MC generator. The result from a given iterations is used as a prior in the next iteration. The iterative method should usually quickly converge into a stable result. However in practice, after several iterations results exhibits a fluctuation due to detector effects and further iterations do not provide any improvement. The number of iteration has been determined from the closure tests where different MC was used for the prior and the pseudo-data. It was observed that the agreement between the truth value and the unfolded distribution does not improve after the first iteration. The fluctuations due to detector effects appear already in the second iteration thus only one iteration was used to correct the data.

The results obtained by Bayesian unfolding were compared with Singular Value Decomposition [127] and Bin-by-Bin unfolding. The difference between results obtained by the unfolding methods was below 10%, what is much smaller than the overall error of the measurement as it will be shown. The RooUnfold library [128] implementing all these methods was used for the unfolding. The statistical errors were computed using a covariance matrix from the variation of the results in toy MC tests, this is recommended RooUnfold procedure for the case of Bayesian unfolding. It should be noted that the statistical errors are negligible compared to the total error of the measurement.

³The forward rapidity gap side can differ between detector and truth level also for $p_{\text{T}}^{\text{cut}} = 200$ MeV but usually both gaps are so small that the anti-correlation effect is not present. However, after application of a higher $p_{\text{T}}^{\text{cut}}$ the anti-diagonal correlation can appear, as apparent from Figure 11.5.

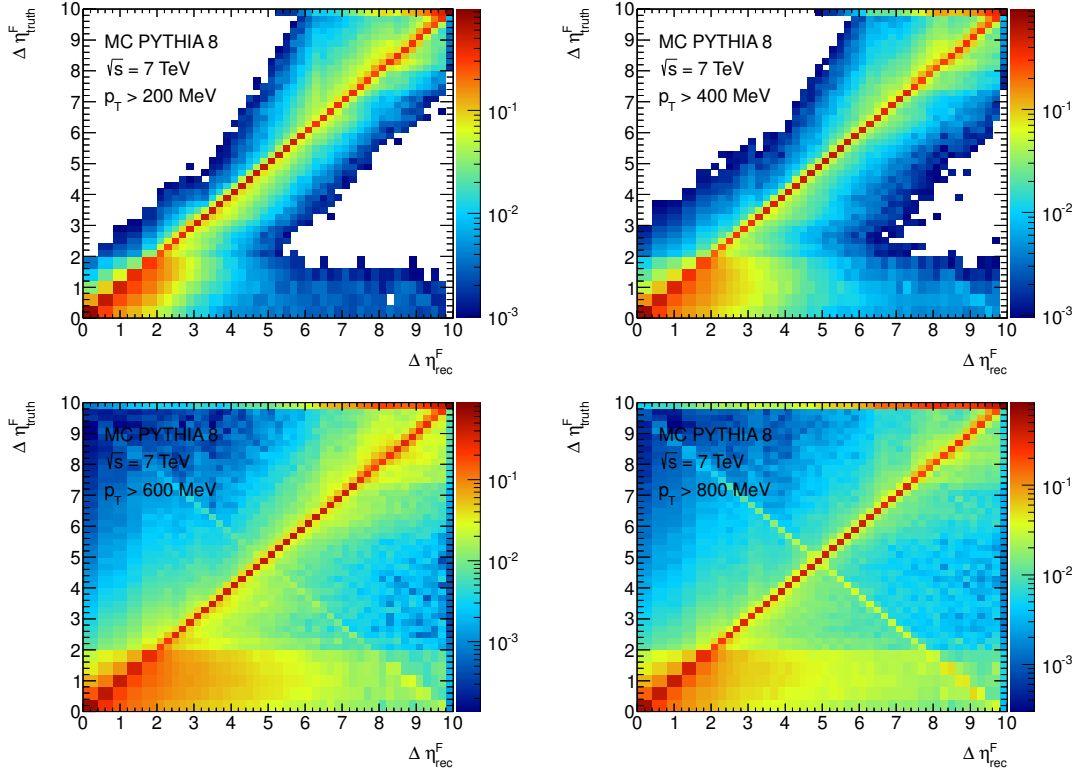


Figure 11.5: Unfolding matrices obtained by PYTHIAS illustrating migrations between detector level, $\Delta\eta_{\text{rec}}^F$, and hadron level $\Delta\eta_{\text{truth}}^F$ for cuts $p_T > 200, 400, 600, 800$ MeV. For $p_T^{\text{cut}} = 400, 600, 800$ MeV the side of the detector from which the rapidity gap is reconstructed is defined as the side for $p_T^{\text{cut}} = 400$ MeV. The definition reduces anti-diagonal correlation in the matrices with $p_T^{\text{cut}} = 600, 800$ MeV and removes unphysical bump from the final unfolded cross sections.

11.3 Systematic Uncertainties

A detailed description of the systematic uncertainties considered in the measurement is presented in this section. The effect of each systematic uncertainty is illustrated in Figure 11.6. Those uncertainties which have large effect on the measurement are shown on the left and the rest is on the right of the figure.

11.3.1 Energy Scale Uncertainty

The electromagnetic scale is derived from studies of $\pi_0 \rightarrow \gamma\gamma$ and is compared to previous studies of $Z \rightarrow ee$ [121]. For the hadronic scale, a combination of $\frac{E}{p}$ studies and test-beam data are evaluated. The uncertainty in the upstream material budget is also included in this systematic through the test-beam analysis. The resulting uncertainties are quoted per region, regions are influenced more by cell density and material budget than individual sub detectors.

- 5% for $|\eta| < 2.3$ (from E/p studies);
- 13% for $2.3 < |\eta| < 3.6$ (12% π_0 ; 4% test-beam hadrons);
- 12% for $3.6 < |\eta| < 4.9$ (9% π_0 ; 8% test-beam hadrons);
- 20% for $1.37 < |\eta| < 1.52$ (Special treatment for Crack region [121]).

A care must be taken when applying the energy scale systematics. The cell/cluster response on the particle deposits is varied but the noise is kept to be the same. Technically this is achieved by changing the energy sampling fraction which converts particle energy deposits into digit counts of the analog-to-digital convertor. The noise digit counts are kept unchanged. The non-diffractive, single diffractive and double diffractive samples of PYTHIA8 have been re-digitized and re-reconstructed, with the nominal energy scale uncertainties described above. The difference between the nominal and varied rapidity gap distribution is used as the energy scale uncertainty. It can be seen from Figure 11.6 that the energy scale uncertainty is one of the dominant errors in the measurement.

11.3.2 Additional Material Uncertainty

Supplementary simulation with an additional 10% extra material in the whole Inner Detector (excluding sensitive detectors) was performed in PYTHIA6. So as to not double-count the PYTHIA6 unfolding uncertainty, the difference of the extra material sample with respect to the nominal PYTHIA6 sample is taken as a source of uncertainty. This amounts to up to around 3.5% across the distribution.

11.3.3 MBTS Efficiency

The description of the MBTS efficiency in the MC models leads to a potential systematic effect on the trigger efficiency and the off-line MBTS requirement. The associated uncertainty is evaluated by increasing the thresholds of all MBTS counters in the simulation to match the maximum variation in the measured response in data according to studies with particles extrapolated from the tracker, HEC or FCal [3]. This systematic error is negligible in the regime where the result is presented, $\Delta\eta^F < 8$.

11.3.4 Tracking Uncertainty

The influence of tracking efficiency on gap reconstruction was studied. The reconstruction was defined in the same way as discussed in [129]. The resulted uncertainty has effect smaller than 0.5% on the cross section and therefore it is not included in our results.

11.3.5 MC Unfolding Uncertainty

The full cross section unfolding procedure is carried out using each of the PYTHIA6, PYTHIA8 and PHOJET models. The deviations of PYTHIA6 and PHOJET from PYTHIA8 define the model dependence which is applied symmetrically for the upward and downward uncertainties. When evaluating this systematic, both the trigger efficiency correction and response matrix are taken from the model. The model dependence uncertainty is dominant, reaching up to 25% for small gaps and up to 10% in the diffractive plateau.

11.3.6 Diffractive Mix Uncertainty

While the fraction of diffractive to non-diffractive events for the tuned MCs used to data correction are taken from the measurement of single sided events in MBTS [3], see tuned fractions in Table 6.1, the relative fraction of single to double dissociation is less well known and harder to constrain.

Especially the double diffractive processes, in which the pseudorapidity of system Y overlap with the detector but it is not detected, are responsible for large migration in the gap spectrum between detector and particle level. To account for the uncertainty of the relative mix of these two processes, the analysis is performed with the diffractive fraction constrained by the Tevatron data [66]. This data were measured in $p\bar{p}$ interactions at 1.8 TeV however similar DD/SD ratio is expected at LHC energies. The DD data refers to events with a rapidity gap which spans central rapidity, $\Delta\eta > 3$ and SD refers to events which satisfy $1.4 \text{ GeV}^2 < M_X^2 < 0.15 \text{ TeV}^2$. These acceptance factors are calculated with generator level MC and used to modify the bound appropriately for each generator. The calculated constraints are listed in Table 11.1 and 11.2, it should be noted that the default cross sections for both PHOJET and PYTHIA lie outside of the

calculated bounds. Also, with PHOJET the fraction of central diffraction is kept at its default value. An uncertainty on the CD is discussed in following section.

For the purposes of trigger efficiency correction and forming of the MC unfolding smearing matrix, MC are combined using the *tuned nominal* values and varied between the *lower bound* and *upper bound* values for systematic evaluation. This results in 1% uncertainty across the diffractive plateau.

PYTHIA Constraint: 29% < DD/SD < 68%				
	Default	Lower Bound	Tuned Nominal	Upper Bound
f_{SD}	59.4%	77.82%	69.06%	62.08%
f_{DD}	40.6%	22.18%	30.94%	37.92%

Table 11.1: Constraint on DD/SD ratio in PYTHIA according to Tevatron data [66].

PHOJET Constraint: 44% < DD/SD < 94%					
	Default	Lower Bound	Tuned Nominal	Upper Bound	CD Bound
f_{SD}	67.1%	63.69%	54.22%	47.21%	56.99%
f_{DD}	24.6%	28.01%	37.48%	44.49%	37.48%
f_{CD}	8.3%	8.3%	8.3%	8.3%	5.59%

Table 11.2: Constraint on DD/SD ratio and CD/SD in PHOJET according to Tevatron data [130].

11.3.7 Central Diffraction Uncertainty

Contribution of central diffraction is another quantity poorly constrained by data. This process is only modeled in the PHOJET generator where it accounts for 8.3% of the diffractive events. Recent results from the Tevatron [130] measure the ratio of $CD/SD = 0.093$.

The fractional rate of central production is considered as a source of uncertainty. The *Tuned Nominal* value f_D and DD fraction in PHOJET are fixed, the CD/SD ratio is set according the Tevatron constrain. This leads to a slight reduction in the amount of CD as can be seen from Table 11.2. The difference with respect to the nominal PHOJET is considered as systematic uncertainty. The effect is approximately a 1% variation across the diffractive plateau.

11.3.8 Luminosity Uncertainty

Following the 2010 van der Meer scan results [60], the uncertainty on the integrated luminosity is 3.4%.

11.3.9 Summary of Systematic Uncertainties

The total systematic error on the cross section is taken as a sum in quadrature of the energy scale, extra material, MBTS, MC unfolding uncertainties, single to double diffractive mixing, double pomeron uncertainty and luminosity uncertainty mentioned above.

MC unfolding uncertainty has contribution dominant over most of the distributions, reaching up to 25% in some regions. The energy scale uncertainty also leads to a significant contribution. It is comparable with the MC unfolding uncertainty for gaps $\Delta\eta^F \sim 2.5$ and for $p_T^{\text{cut}} = 400$ MeV it even exceeds the MC unfolding uncertainty in this region. All other systematic effects are of the scale of the luminosity error (3.5%) or smaller. All systematic bands are presented for all p_T cuts in Figure 11.6. The statistical error is negligible in comparison to overall systematics uncertainty.

11.4 Differential Cross Section for Forward Rapidity Gaps

Results of the measurement of the differential cross section as a function of rapidity gaps are summarized in this section. The differential cross section was measured for particles above the cut $p_T^{\text{cut}} = 200, 400, 600, 800$ MeV. The data cover the range $0 < \Delta\eta^F < 8$. In the large gap region which is populated by diffractive processes, the cross section corresponds to a t -integrated sum of SD events in which either of the colliding protons dissociates and DD events with $\xi_Y \lesssim 10^{-6}$ ($M_Y \lesssim 7$ GeV). The data span the range $\xi_X \gtrsim 10^{-5}$. Diffractive events with smaller ξ_X values are subject to large MBTS trigger inefficiencies and thus lie beyond the kinematic range of the measurement.

The rapidity gaps measurement allows to constrain the pomeron intercept in the triple pomeron based models introduced previously. Furthermore, the hadronisation and underlying event models can be tested using the small rapidity gap regime at small p_T^{cut} or at large p_T^{cut} in which also the non-diffractive events produce large rapidity gaps.

11.4.1 Differential Cross Section for $p_T^{\text{cut}} = 200$ MeV

The results on differential cross section as a function of rapidity gaps for particles with transverse momenta $p_T > 200$ MeV are presented in Figure 11.7. The cut $p_T^{\text{cut}} = 200$ MeV corresponds to the lowest experimentally accessible energy as discussed in Section 8.2. In the top left plot of Figure 11.7 data are compared with overall predictions of PHOJET, PYTHIA6, and PYTHIA8. Remaining plots show relative contributions of ND, SD, DD and CD predicted by the MCs.

All MCs contain the exponential decrease of the cross section with increasing gap size present in the data at small gaps, $\Delta\eta^F \lesssim 2$. This behavior is typical for ND component which has dominant contribution according to all MCs in this regions. Only small fraction of events $\sim 10^{-2}$ is expected to be diffractive. These are SD or DD events with very large $\xi_X \gtrsim 10^{-2}$ or DD events

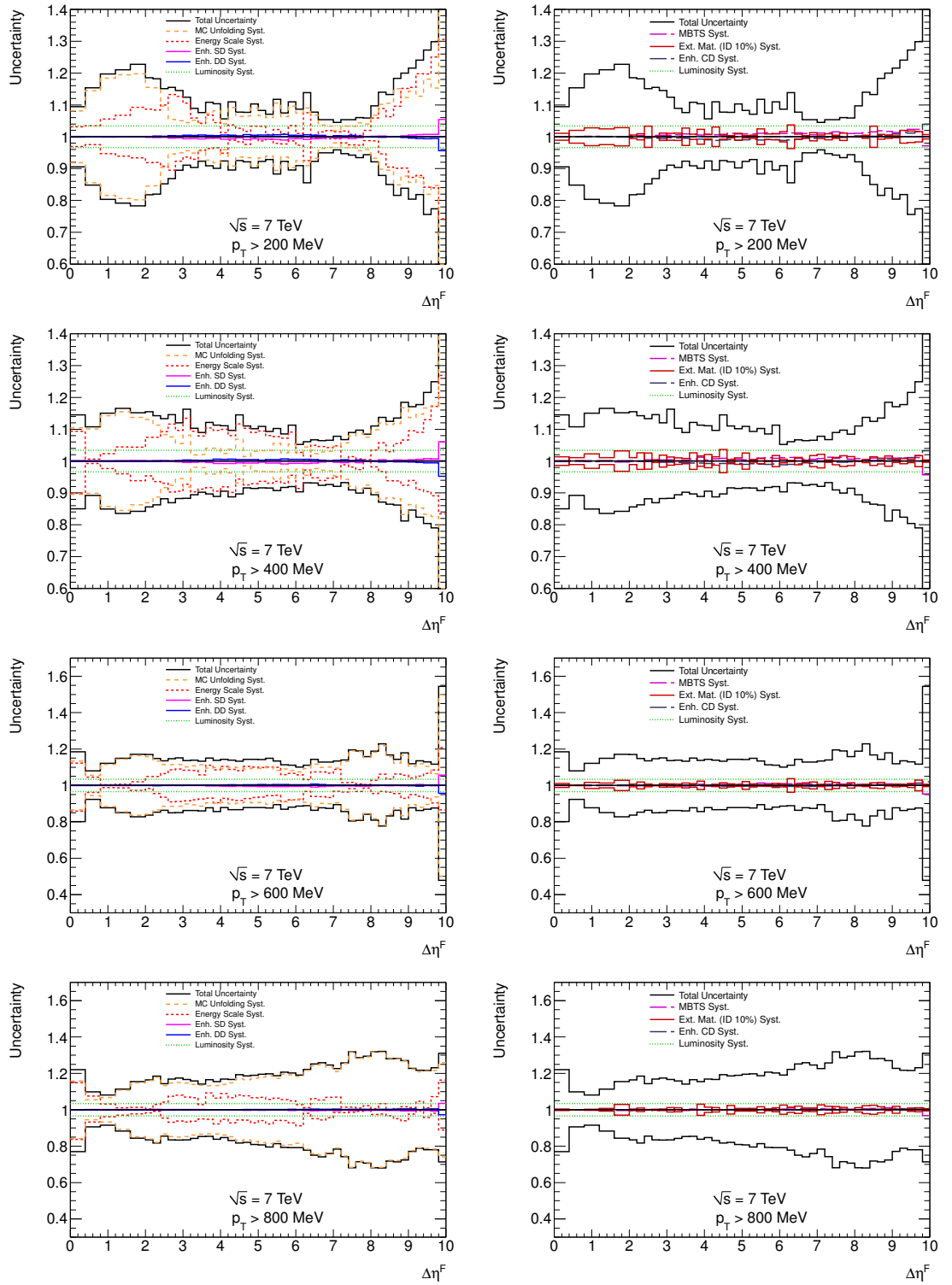


Figure 11.6: Systematics uncertainties presented for four different p_T cuts from 200 MeV to 800 MeV. The left plots show the cluster energy scale, luminosity, unfolding difference between MC models and variation of single to double diffraction ratio. The right plots show the uncertainty from 10% addition support material in the ID, variation of double pomeron exchange and variation of offline MBTS threshold.

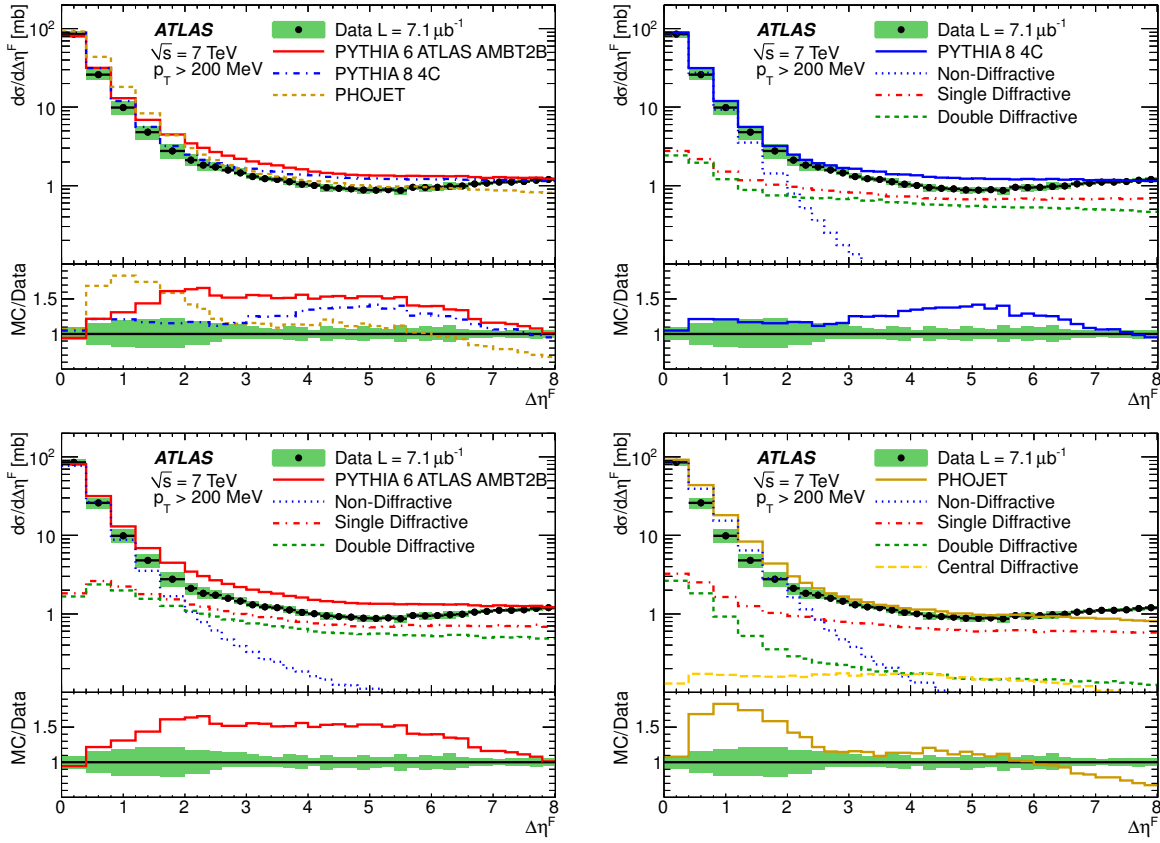


Figure 11.7: Inelastic cross section differential in forward gap size $\Delta\eta^F$ for particles with $p_T > 200$ MeV. The shaded bands represent the total uncertainties. The full lines show the predictions of PHOJET and the default versions of PYTHIA6 and PYTHIA8. The dashed lines illustrate contributions of the ND, SD and DD components according to the models. The CD contribution according to PHOJET is also shown in bottom right.

$\xi_Y \gtrsim 10^{-6}$. PYTHIA8 has the best agreement with the data while PHOJET overestimates the ND contribution by a factor of ~ 1.5 .

At large gaps, $\Delta\eta^F \gtrsim 3$, the differential cross section exhibits a plateau, which is attributed mainly to diffractive processes. The differential cross section remains around 1 mb per unit of rapidity gap size in this regime. Given the close correlation between $\Delta\eta^F$ and $-\ln \xi$, (4.23), this behavior is expected as a consequence of the dominance of soft diffractive processes. The plateau is roughly modeled in the all MCs, as can be seen in detail from Figure 11.8. PYTHIA MCs overshoots the data almost in the whole regime despite of the tuning of f_D according the [3]. This can be associated with large DD contribution in the measured region which exceeds the data from Tevatron [131]. The underestimation of f_D in PHOJET is compensated by excess of the total inelastic cross section, thus it achieves the best agreement with data. In addition, Figure 11.8 shows Donnachie-Landshoff model implemented in PYTHIA8. It should be emphasized that the

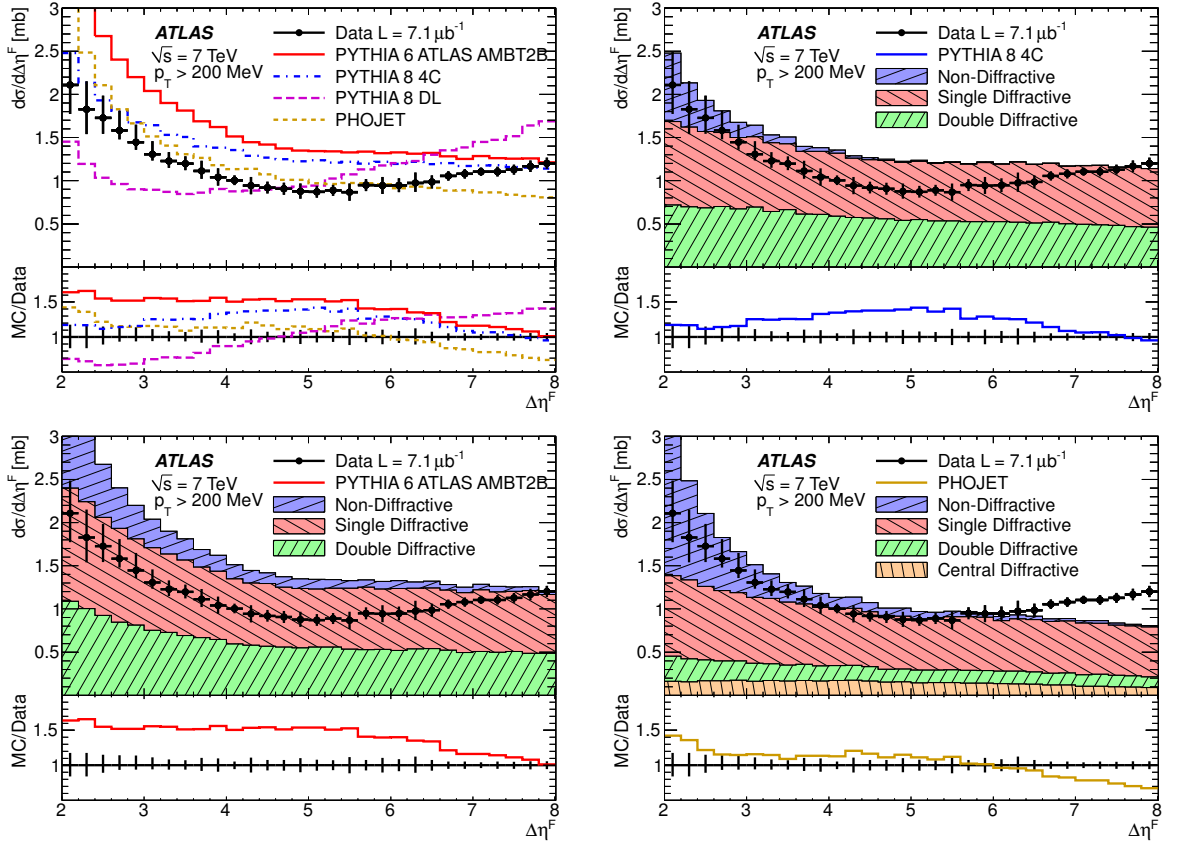


Figure 11.8: Inelastic cross section differential in forward gap size $\Delta\eta^F$ for particles with $p_T > 200$ MeV and $\Delta\eta^F > 2$. The error bars indicate the total uncertainties. In top left plot, the full lines show the predictions of PHOJET, the default versions of PYTHIA6 and PYTHIAS, and PYTHIAS with the Donnachie-Landshoff pomeron flux. The remaining plots show the contributions of the SD, DD and ND components according to each generator. The CD contribution according to PHOJET is also shown in bottom right.

slope of the data is between the slope of the Donnachie-Landshoff and the rest of the models. This is due to different pomeron intercept $\alpha_P(0)$ which is 1.085 for Donnachie-Landshoff and 1.0 for the rest of the models.

11.4.2 Estimation of Pomeron Intercept

The strong correlation between the pomeron intercept, $\alpha_P(0)$, and the slope of the differential cross section at large gap can be used for determination of $\alpha_P(0)$. The data in high purity diffractive region, $\Delta\eta^F > 6$, were used to obtain the best estimate of Pomeron intercept to describe the data. The MC samples with varying pomeron intercept but with the same pomeron slope $\alpha'_P = 0.25 \text{ GeV}^{-2}$ were generated with Donnachie-Landshoff model implemented in PYTHIAS. The SD, DD, and ND contributions were mixed according to the default SD to DD ratio but with

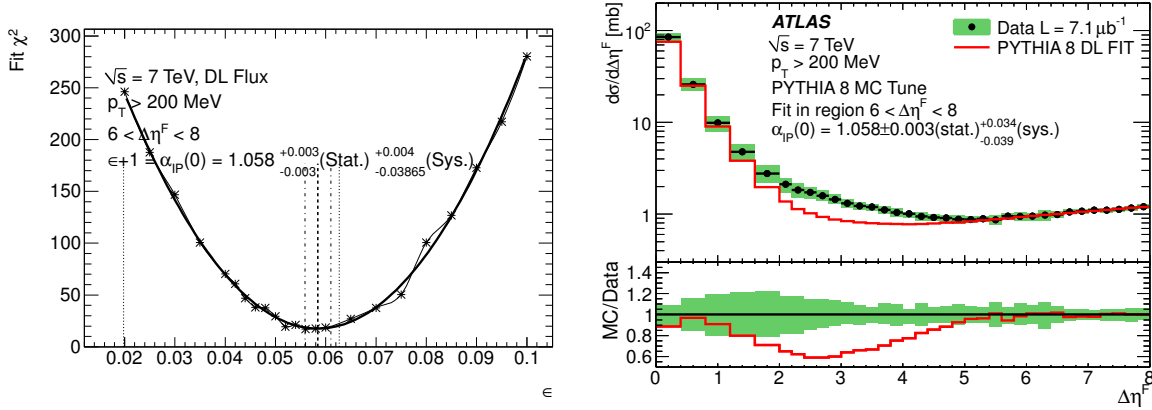


Figure 11.9: (Left) χ^2 minimization of Donnachie-Landshoff (DL) flux model in PYTHIA8 for cross section as a function of $\Delta\eta^F$. The bold dashed line in the middle corresponds to the minimum of $\chi^2(\epsilon)$, the two dashed-dotted lines denote statistical error and the two dotted lines represent overall systematics uncertainty before symetrization of the MC model uncertainty was applied. (Right) Inelastic cross section as a function of forward rapidity gap of the fitted DL model in PYTHIA8 for $p_T^{\text{cut}} = 200$ MeV.

the fitted total diffractive fraction $f_D = 25.6\%$ obtained using the samples with $\alpha_{\text{IP}}(0) = 1.058$.

χ^2 was evaluated for each sample in region $6 < \Delta\eta^F < 8$, with the cross section integrated over the fitted region allowed to float as a free parameter. The χ^2 data points corresponding to individual pomeron intercepts were fitted by the parabola, which can be seen in Figure 11.9. The point where parabola reaches the minimum, χ_{min}^2 , is the optimal $\alpha_{\text{IP}}(0)$. Statistical errors on the fitted value of $\alpha_{\text{IP}}(0)$ were determined by finding the roots of an equation $\chi^2(\alpha_{\text{IP}}(0)) = \chi_{\text{min}}^2 + 1$. This procedure was applied to nominal cross section and to each systematic effect described in Section 11.3.9. The differences between the fit of nominal distribution and each systematics shifts were summed in quadratures to obtain total uncertainty on the $\alpha_{\text{IP}}(0)$. The systematic uncertainty is dominated by the MC model dependence of the data correction procedure, in particular the effect of unfolding using PYTHIA6 in place of PYTHIA8. This leads to a significantly flatter dependence of the data on $\Delta\eta^F$ at large gap sizes. Since both PYTHIA6 and PHOJET cause large downward shifts with respect to nominal value obtained by PYTHIA8, the MC model uncertainty is symmetrized with respect to nominal value. The sensitivity on the shift of diffractive fraction, f_D , was also investigated but its variation has negligible effect on the resulted $\alpha_{\text{IP}}(0)$. The obtained pomeron intercept for the Donnachie-Landshoff model in PYTHIA8 is

$$\alpha_{\text{IP}}(0) = 1.058 \pm 0.003(\text{stat.})_{-0.039}^{+0.034}(\text{syst.}). \quad (11.3)$$

The χ^2/NDof at the nominal minimum is 1.5. The distribution corresponding fitted pomeron intercept can be seen in Figure 11.9. The obtained $\alpha_{\text{IP}}(0)$ value is compatible with the default pomeron intercept $\alpha_{\text{IP}}(0) = 1.085$ in Donnachie-Landshoff model due to large systematic uncer-

tainty. Finally, it should be mentioned that the measurement of rapidity gap distribution with single center-of-mass energy is not sensitive to value of the pomeron slope, $\alpha'_{\mathbb{P}}$.

11.4.3 Higher Transverse Momentum Cuts

Increasing the transverse momentum cut on the final particles leads to a production of larger rapidity gaps. This can be seen from Figure 11.11 showing the differential inelastic cross section as a function of rapidity gap, $\Delta\eta^F$ measured for following transverse momentum cuts $p_T^{\text{cut}} = 200, 400, 600, 800$ MeV. Increasing the p_T^{cut} from 200 MeV to 400 MeV has only small effect. The distribution has similar behavior as for $p_T^{\text{cut}} = 200$ MeV and the ND component is dominant only up to $\Delta\eta^F \sim 3$ according to all MC models. Relatively large difference is visible between distribution with $p_T^{\text{cut}} = 400$ MeV and $p_T^{\text{cut}} = 600$ MeV. Production of particles with such large transverse momentum is rare also in non-diffractive processes and therefore the difference between diffractive and non-diffractive component smears out in the rapidity gap distributions. This behavior is even more significant for distribution with $p_T^{\text{cut}} = 800$ MeV where all MCs predicts that production of very large gaps $\Delta\eta^F \sim 8$ in non-diffractive events is almost the same order of magnitude as in the diffractive case. The agreement between data and both PYTHIA6 and PYTHIA8 is observed to improve at higher p_T cuts. PHOJET retains a good description at large gap sizes but continues to overestimate the cross section for gaps with $\Delta\eta^F < 5$.

11.4.4 Inelastic Distribution in Herwig++

The distribution at small rapidity gaps is sensitive to fluctuations in hadronisation processes thus it is interesting to compare the data with different hadronisation models than Lund String model implemented in PYTHIA and PHOJET⁴, see Section 6.4.2. An alternative is a cluster hadronisation model, described in Section 6.4.3, which is available in HERWIG++. Figure 11.11 shows comparison of HERWIG++ minimum bias tune UE7-2 [132] with data. It should be emphasized that the model of minimum bias production does not contain diffractive processes and thus only exponential fall-off of the rapidity gap distribution is expected. Even though not containing an explicit diffractive component, HERWIG++ produces large gaps with non-exponential behavior and bump around $\Delta\eta^F = 6$ which is presented for all transverse momentum cuts.

Four variants of the default UE7-2 tune can be seen in Figure 11.11. All the HERWIG++ distributions are normalized to inelastic cross section of 81 mb predicted by the default UE7-2 tune. The default UE7-2 model contains colour reconnection (CR) model which leads to successful description of charged particle multiplicities at LHC and Tevatron. Even though switching of the colour reconnection model leads to slight suppression of large gaps, the non-exponential behavior of the distribution persists. As it was discussed in Section 6.5, the model

⁴In fact PHOJET uses the PYTHIA6 hadronisation code.

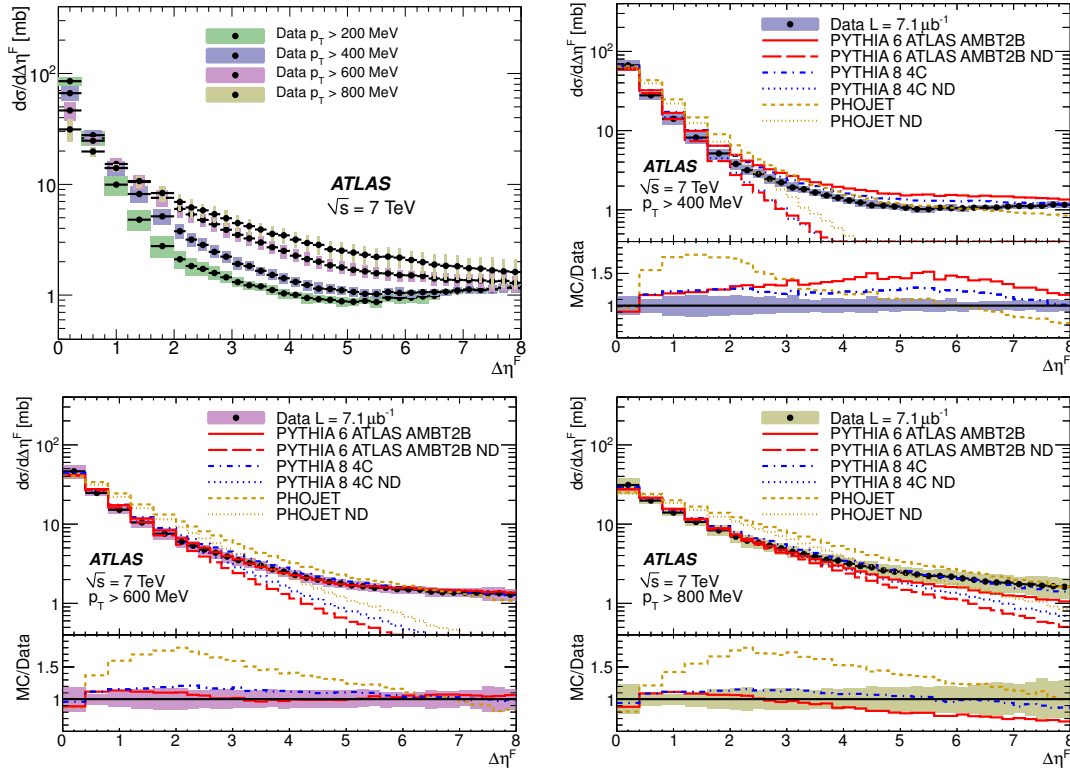


Figure 11.10: Inelastic differential cross section in forward gap size $\Delta\eta^F$ for different p_T^{cut} values. Comparison between the measured cross sections is in the top left. The full uncertainties are shown. They are correlated between the different p_T^{cut} choices. The remaining plots show comparison between the data and the MC models for $p_T^{\text{cut}} = 400, 600$ and 800 MeV. The non-diffractive component in each MC model is also shown.

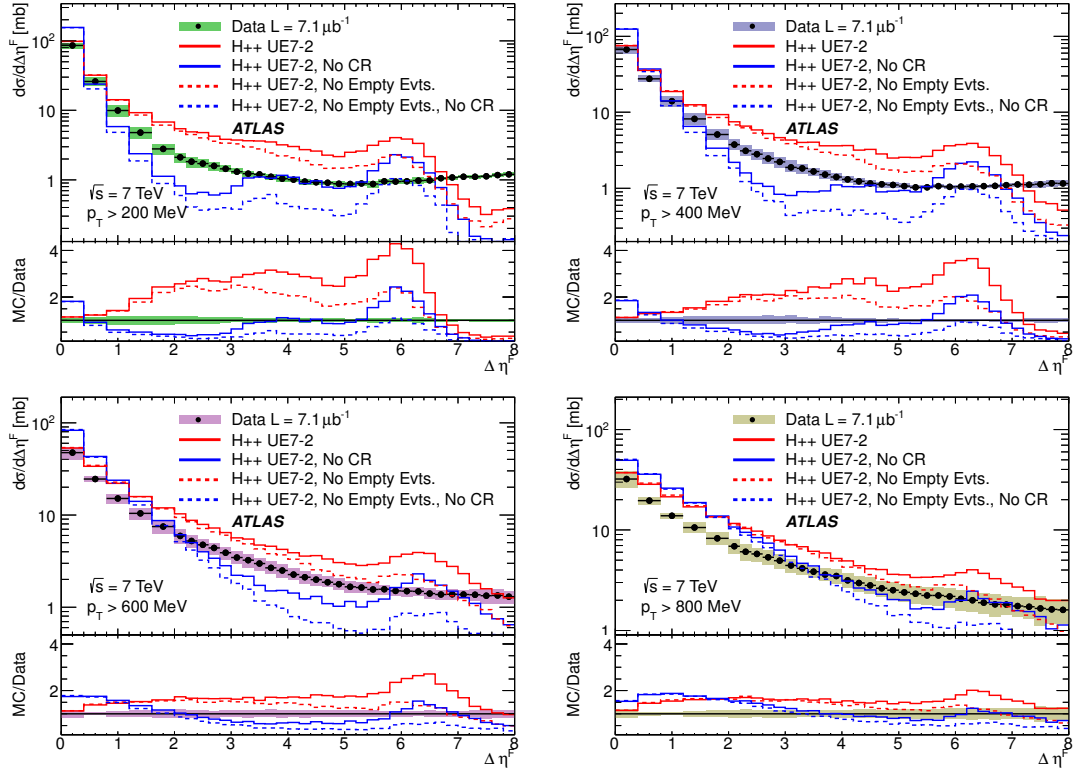


Figure 11.11: Inelastic differential cross section in forward gap size $\Delta\eta^F$ for $p_T^{\text{cut}} = 200, 400, 600, 800$ MeV. The data are compared with the UE7-2 tune of the HERWIG++ model. In addition to the default tune, versions are shown in which the colour reconnection model is switched off and in which events with zero scatters are excluded (see text for further details).

for multiple interactions admits events where no soft or semi-hard scatterings occur. This could eventually lead to production of large gaps between the dissociated protons which would mimic DD topology. The HERWIG++ gap cross section is reduced after removal of these empty semi-hard or soft events (No Empty Evt.) but the non-exponential tail and large $\Delta\eta^F$ enhancement persist. The poor description of the forward rapidity gap distribution has been discussed with the HERWIG++ authors but so far none of the model parameters is able to fix the discrepancy.

11.5 Summary

The novel algorithm for reconstruction of rapidity gaps using the ATLAS detector between particles with momentum transverse $p_T \geq 200$ MeV was introduced. The differential cross section as a function of forward rapidity gap was measured for particles with transverse momenta above $p_T^{\text{cut}} = 200, 400, 600, 800$ MeV. Measurements were corrected to the level of stable hadrons. An exponentially falling non-diffractive distribution was observed at small gaps. The distribution exhibits a plateau at large gap sizes which is expected for diffractive processes. This plateau

amounts to a cross section close to 1 mb per unit of gap size and is reasonably well described in shape by the Monte Carlo models, which are based on a triple Regge approach. PYTHIA8 and PYTHIA6 well model the small rapidity gap region while PHOJET provides good description of large rapidity gaps.

Whilst the data are insensitive to the choice of pomeron slope $\alpha'_{\mathbb{P}}$, there is considerable sensitivity to the value of pomeron intercept $\alpha_{\mathbb{P}}(0)$. The rise of the cross section at large rapidity gaps was fitted by the Donnachie-Landshoff model implemented in PYTHIA8. A pomeron slope parameter $\alpha_{\mathbb{P}}(0) = 1.058 \pm 0.003(\text{stat.})_{-0.039}^{+0.034}(\text{syst.})$ provides the best fit to data.

The minimum bias model UE7-2 tune implemented in HERWIG++ which uses the alternative cluster hadronisation model was compared to data. The HERWIG++ model produces large gaps which are not exponentially suppressed with size of the rapidity gaps even though the minimum bias model does not contain diffractive production explicitly.

Chapter 12

Summary

This thesis is devoted to diffractive physics at Large Hadron Collider. The experimental part of the work was measurement of rapidity gap production in the minimum bias events with the ATLAS detector. Slightly different topic was implementation of forward physics processes into HERWIG++ which can be measured at LHC.

The diffractive models are spread among many MC generators. Some of the generators start to be obsolete and are not further developed or tuned to data. In addition, it is more comfortable for user to have all models available under one unified interface. Due to these reasons one part of the PhD work was implementation of diffractive and exclusive models into the HERWIG++ MC generator. Hard diffraction and QED exclusive production have already been added into HERWIG++ release 2.5 [84]. HERWIG++ with these processes included is already used in measurements of diffractive di-jet or di-muon production in the ATLAS. In future, the implemented models could be used for studies of anomalous coupling between γ and W in two-photon initiated processes planned to be measured by AFP [97]. Exclusive QCD production of Higgs, di-jet and di-photon final states is prepared to be submitted into the next release. The outlook is implementation of three final states processes which are important background for searches in the exclusive channels. These processes have not been implemented in any MC generator yet due to complicated phase-space which requires high performance algorithm for automatic sampling.

The experimental section discusses the measurement of the rapidity gap production at $\sqrt{s} = 7$ TeV. The rapidity gaps are reconstructed using the ATLAS calorimeter system in combination with Inner Detector. The crucial issue to define rapidity gaps in the calorimeter is separation of the electronic noise from the physics signal. The noise is suppressed to acceptable level by a requirement on the most significant cell in the topological cluster or in given calorimeter region. Two different definitions of rapidity gaps were introduced:

- **Floating rapidity gap** $\Delta\eta$: is the largest empty pseudorapidity region between two nearest particles in η , inside the detector acceptance.

- **Forward rapidity gap** $\Delta\eta^F$: is the larger of the two empty pseudorapidity regions expanding between the edges of the detector of the acceptance $\eta = 4.9$ or $\eta = -4.9$ and the nearest particle.

Floating rapidity gap is used to measure diffractive fraction of the total inelastic cross section in Chapter 10. This 2-dimensional algorithm provides information about size and position of the gap what improves separation of single diffractive and double diffractive events. The obtained result for diffractive fraction $f_D = 30.2 \pm 0.3(\text{stat.})_{+4.5}^{-3.8}(\text{syst.})\%$ is in good agreement with previous measurement [3] performed using the MBTS detector. However, the MC model uncertainty of our measurement is not improved with respect to the one obtained with MBTS as it was originally expected.

Due to small rapidity coverage of the ATLAS detector large amounts of double diffractive events mimics the single diffraction. In order to obtain a stable fit result, the SD and DD templates were redefined into new SD-like and DD-like templates according to mass of the smaller dissociated system M_Y . Even though, the redefined templates improves stability of the fit, the SD-like to DD-like ratio strongly depends on the MC model. The determined fractions are therefore tightly linked to the generator and can be considered for tuning of the MC only. The analysis can be found in the ATLAS public document [117] which was presented at the conferences as preliminary result only. Due to the above issues, further improvements are not considered.

Chapter 11 is devoted to the measurement of the inelastic differential cross section as a function of forward rapidity gap size. The measurement was published in [124]. The differential cross section was measured for different cuts on the transverse momenta of final particles $p_T^{\text{cut}} = 200, 400, 600, 800$ MeV, where the lowest cut $p_T^{\text{cut}} = 200$ MeV was estimated as the lowest accessible energy with a good calorimeter acceptance. The measurement is directly sensitive to variable ξ and thus it allows to constrain diffractive models. In addition, the differential cross section at small rapidity gaps tests hadronisation and underlying event models in the MC generators. The exponential decrease at small rapidity gaps which is typical for fluctuation in hadronisation in non-diffractive processes is reflected by PYTHIA6, PYTHIA8 and PHOJET. At large gaps the expected diffractive plateau was observed and reasonably modeled by the MCs.

Whilst the data are insensitive to the choice of the pomeron slope α'_P , the pomeron intercept $\alpha_P(0)$ is strongly correlated with the slope of the rapidity gap distribution at large gaps. The increase in the differential cross section at large rapidity gaps was fitted by the Donnachie-Landshoff model implemented in the PYTHIA8. The obtained result $\alpha_P(0) = 1.058 \pm 0.003(\text{stat.})_{-0.039}^{+0.034}(\text{syst.})$ is compatible with default Donnachie-Landshoff value $\alpha_P(0) = 1.085$ due to systematic uncertainty which is dominated by MC model selection for unfolding.

By increasing the p_T^{cut} to higher values the larger rapidity gaps are produced also in the non-diffractive component. The effect is relatively small for transition from 200 MeV to 400 MeV. However, at $p_T^{\text{cut}} = 600$ MeV very large gaps are produced in the ND events according to all MCs

thus the difference between diffraction and non-diffraction disappears. In general, modeling of rapidity gap distribution improves with increasing p_T^{cut} values.

The minimum bias model UE7-2 tune implemented in HERWIG++ which uses the alternative cluster hadronisation model was compared to data. The HERWIG++ model exhibits large gap production without exponential suppression at large gap sizes even though the minimum bias model does not contain diffractive production. The exact reason for this behavior is still to be investigated by HERWIG++ authors.

The measurement of the cross section as a function of forward rapidity gap has already had an impact on the community developing models for description of soft interactions and diffraction physics in pp collisions. One of them is KMR model [133] combining phenomenological Regge inspired model and QCD BFKL description described in Section 4.2 which is recently implemented into SHERPA [134]. An alternative model proposed by Gotsman, Levin, Maor [135] was also tested by our data.

Acknowledgment

This thesis could not be done without the help of many people, and in this section I would like to express many thanks to them. First, I would like to thank to my supervisor Václav Vrba who provided me with background and a great support during my PhD research. I am grateful to him for helping me with the choice of my PhD topic and with several decisions I had to make during my studies.

I would like to express especially great thanks to my colleagues and friends Oldřich Kepka and Alexander Kupčo who spend many hours of discussions about particle physics and who gave me many advises necessary for finishing this work. I enjoyed my work on rapidity gap analysis together with Oldřich Kepka and our colleagues Tim Martin and Paul Newman. I have obtained many valuable experience thanks to this collaboration.

Thanks to Marie Curie fellowship I could spend four months at Institute of Particle Physics Phenomenology in Durham under the supervision of Peter Richardson. Peter Richardson and David Grellscheid provide me great introduction to Monte Carlo problematics and thanks to their help the implementation of diffractive and exclusive processes into HERWIG++ could be accomplished.

Finally, I am grateful to my family and Lucia Bátková for their support and patience during my PhD work.

Bibliography

- [1] The ATLAS Collaboration. Charged-particle multiplicities in pp interactions measured with the ATLAS detector at the LHC. *New J. Phys.*, 13:053033, 2011. [arXiv:1012.5104](#).
- [2] Z Ajaltouni et al. Proceedings of the workshop: HERA and the LHC workshop series on the implications of HERA for LHC physics, chapter 5. 2009. [arXiv:0903.3861](#).
- [3] The ATLAS Collaboration. Measurement of the Inelastic pp Cross Section at $\sqrt{s} = 7$ TeV. *Nature Comm.*, 2:463, 2011. [arXiv:1104.0326](#).
- [4] J. Horejsi. *Fundamentals of Electroweak Theory*. Karolinum Press, 2002.
- [5] H. Georgi. *Lie Algebras in Particle Physics*. Westview Press, 1999.
- [6] W. J. Stirling R.K. Ellis and B.R. Webber. *QCD and Collider Physics*. Cambridge University Press, 1996.
- [7] I. Knowles G. Dissertori and M. Schmelling. *Quantum Chromodynamics, High Energy Experiments and Theory*. Oxford University Press, 2003.
- [8] M. Ciafaloni. Coherence effects in initial jets at small Q^2/s . *Nucl. Phys.*, B296:49, 1988.
- [9] G. Marchesini S. Catani, F. Fiorani. QCD coherence in initial state radiation. *Phys. Lett.*, B234:339, 1990.
- [10] E. Predazzi V. Barone. *High-Energy Particle Diffraction*. Springer, 2002.
- [11] P. V. Landshoff A. Donnachie. Total cross section. *Phys. Lett.*, B 296:227, 1992. [arXiv:9209205](#).
- [12] U. Maor E. Gotsman, E. M. Levin. Diffractive dissociation and eikonalization in high energy pp and $p\bar{p}$ collisions. *Phys. Rev. Lett.*, D49:4321, 1994.
- [13] K. Goulianos R.J.M. Covolan, J. Montanha. A new determination of the soft pomeron intercept. *Phys. Lett.*, B389:176, 1996.

- [14] M. G. Ryskin, A. D. Martin, and V. A. Khoze. High-energy strong interactions: from ‘hard’ to ‘soft’. *Eur. Phys. J.*, C71:1617, 2011. [arXiv:1102.2844](#), [doi:10.1140/epjc/s10052-011-1617-2](#).
- [15] M. L. Good and W. D. Walker. Diffraction dissociation of beam particles. *Phys. Rev.*, 120:1857–1860, 1960. [doi:10.1103/PhysRev.120.1857](#).
- [16] K. Goulianos. Renormalization of hadronic diffraction and the structure of the pomeron. *Phys. Lett.*, B358:379, 1995.
- [17] K. Goulianos and J. Montanha. Factorization and scaling in hadronic diffraction. *Phys. Rev. Lett.*, D 59:114017, 1999.
- [18] R. Bonino et. all. Evidence for transverse jets in high-mass diffraction: UA8 Experiment. *Phys. Lett.*, B 211:239, 1988.
- [19] J. C. Collins. Proof of factorization for diffractive hard scattering. *Phys. Rev.*, D57:3051, 1998. [arXiv:9709499](#).
- [20] P. E. Schlein G. Ingelman. Jet structure in high mass diffractive scattering. *Phys. Lett.*, B 152:256, 1985.
- [21] A. Aktas et al. Dijet Cross Sections and Parton Densities in Diffractive DIS at HERA. *JHEP*, 0710:042, 2007. [arXiv:0708.3217](#).
- [22] J. D. Bjorken. Rapidity gaps and jets as a new-physics signature in very-high-energy hadron-hadron collisions. *Phys. Rev.*, D47:101, 1993.
- [23] E. Gotsman et. al. Survival Probability of Large Rapidity Gaps, 2005. [arXiv:0511060](#).
- [24] The CMS Collaboration. Evidence for hard-diffractive dijet production in pp collisions at $\sqrt{s} = 7$ TeV, 2012. URL: <http://cdsweb.cern.ch/record/1421606/>.
- [25] T. Affolder et al. Diffractive Dijets with a Leading Antiproton in $\bar{p}p$ Collisions at $\sqrt{s} = 1800$ GeV. *Phys. Rev. Lett.*, 84:5043, 2000.
- [26] K. Goulianos. Hadronic Diffraction: Where do we Stand? [arXiv:0407035](#).
- [27] T. Affolder et al. Dijet Production by Double Pomeron Exchange at the Fermilab Tevatron. *Phys. Rev. Lett.*, 85:4215, 2000.
- [28] T. Aaltonen et al. Diffractive W and Z Production at the Fermilab Tevatron. *Phys. Rev. Lett.*, D82:12004, 2010. [arXiv:1007.5048](#).
- [29] T. Affolder et al. Observation of Diffractive Beauty Production at the Fermilab Tevatron. *Phys. Rev. Lett.*, 84:232, 2000.

- [30] M. G. Ryskin V. A. Khoze, A. D. Martin. Prospects for New Physics observations in diffractive processes at the LHC and Tevatron. *Eur. Phys. J.*, C23:311, 2002. [arXiv:0111078](#).
- [31] S. Heinemeyer et al. Central Exclusive Diffractive MSSM Higgs-Boson Production at the LHC. *J. Phys. Conf. Ser.*, 110:072016, 2008. [arXiv:0801.1974](#).
- [32] P.V. Landshoff A. Bialas. Higgs production in pp collisions by double-pomeron exchange. *Phys. Lett*, B256:540, 1991.
- [33] J.R. Cudell et al. Central exclusive production of dijets at hadronic colliders. *Eur. Phys. J.*, C61:369, 2009. [arXiv:0807.0600](#).
- [34] N. Timneanu R. Enberg, G. Ingelman. Soft Color Interactions and Diffractive Hard Scattering at the Fermilab Tevatron. *Phys. Rev.*, D64:114015, 2001. [arXiv:0106246](#).
- [35] T. Aaltonen et al. Observation of Exclusive Dijet Production at the Fermilab Tevatron p anti-p Collider. *Phys. Rev.*, D7:052004, 2008.
- [36] A. Pilkington J. Monk. ExHuME 1.3: A Monte Carlo event generator for exclusive diffraction. *Comput. Phys. Comm.*, 175:232, 2006. [arXiv:0502077](#), [doi:10.1016/j.cpc.2006.04.005](#).
- [37] T. Kúcs M. Boonekamp. Dpemc: A monte carlo for double diffraction. *Comput. Phys. Comm.*, 167:217, 2005. [arXiv:0312273](#), [doi:10.1016/j.cpc.2005.01.002](#).
- [38] T. Aaltonen et al. Observation of Exclusive Charmonium Production and $\gamma\gamma \rightarrow \mu^+\mu^-$ in p anti-p Collisions at $\sqrt{s} = 1.96$ TeV. *Phys. Rev. Lett.*, 102:242001, 2009. [arXiv:0811.2820](#).
- [39] T. Aaltonen et al. Observation of Exclusive Photon Pair Production in p anti-p Collisions at $\sqrt{s} = 1.96$ TeV. *Phys. Rev. Lett.*, 108:081801, 2012. [arXiv:1112.0858](#).
- [40] The LHCb Collaboration. Central Exclusive Dimuon Production at $\sqrt{s} = 7$ TeV, 2011. URL: <http://cdsweb.cern.ch/record/1349022>.
- [41] V. M. Budnev et al. The two-photon particle production mechanism. Physical problems. Applications. Equivalent photon approximation. *Physics Reports*, 15:181, 1975.
- [42] A. Abulencia et al. Observation of Exclusive Electron-Positron Production in Hadron-Hadron Collisions. *Phys. Rev. Lett.*, 98:112001, 2007.
- [43] The CMS Collaboration. Search for central exclusive gamma pair production and observation of central exclusive electron pair production in pp collisions at $\sqrt{s} = 7$ TeV, 2012. URL: <http://cdsweb.cern.ch/record/1427001>.

- [44] P. Bryant L. Evans. LHC Machine. *JINST*, 3:S08001, 2008.
- [45] W. Herr H. Grote. Nominal and ultimate luminosity performance of the LHC. Technical Report LHC-PROJECT-NOTE-275, 2001. URL: <http://cdsweb.cern.ch/record/691915>.
- [46] The ATLAS Collaboration. ATLAS Experiment at the CERN Large Hadron Collider. *JINST*, 3:S08003, 2008.
- [47] The CMS Collaboration. The CMS experiment at the CERN LHC. *JINST*, 3:S08004, 2008.
- [48] The ALICE Collaboration. The ALICE experiment at the CERN LHC. *JINST*, 3:S08002, 2008.
- [49] The LHCb Collaboration. The LHCb Detector at the LHC. *JINST*, 3:S08005, 2008.
- [50] The TOTEM Collaboration. The TOTEM Experiment at the CERN Large Hadron Collider. *JINST*, 3:S08007, 2008.
- [51] The LHCf Collaboration. The LHCf detector at the CERN Large Hadron Collider. *JINST*, 3:S08006, 2008.
- [52] The ATLAS Collaborattion. Annual Charts of Luminosity, 2012. URL: <https://twiki.cern.ch/twiki/bin/view/AtlasPublic/LuminosityPublicResults>.
- [53] J. Pequeno. Computer generated image of the whole ATLAS detector, 1999. URL: <http://cdsweb.cern.ch/record/1095924>.
- [54] J. Pequeno. Computer generated image of the whole ATLAS inner detector, 1999. URL: <https://cdsweb.cern.ch/record/1095926>.
- [55] J. Pequeno. Computer generated image of the whole ATLAS calorimeter, 1999. URL: <https://cdsweb.cern.ch/record/1095927>.
- [56] Liquid Argon Calorimeter TDR, 1996. URL: <https://cdsweb.cern.ch/record/331061>, [arXiv:CERN/LHCC96-41](https://arxiv.org/abs/CERN/LHCC96-41).
- [57] ATLAS Tile Calorimeter TDR, 1996. URL: <https://cdsweb.cern.ch/record/331062>, [arXiv:CERN/LHCC96-42](https://arxiv.org/abs/CERN/LHCC96-42).
- [58] ATLAS: Detector and physics performance technical design report. Volume 1, 1999. URL: http://www.cern.ch/Atlas/GROUPS/PHYSICS/TDR/physics_tdr/printout/Volume_I.pdf, [arXiv:CERN/LHCC99-014](https://arxiv.org/abs/CERN/LHCC99-014).

- [59] The ATLAS Collaboration. Luminosity determination in pp collisions at $\sqrt{s} = 7$ tev using the atlas detector at the lhc. *Eur. Phys. J. C*, 71:1–37, 2011. 10.1140/epjc/s10052-011-1630-5. URL: <http://dx.doi.org/10.1140/epjc/s10052-011-1630-5>.
- [60] Updated luminosity determination in pp collisions at root(s)=7 tev using the atlas detector. (ATLAS-CONF-2011-011), Mar 2011. URL: <http://cdsweb.cern.ch/record/1334563>.
- [61] S. Agostinelli et al. GEANT4: A simulation toolkit. *Nucl. Instr. Meth.*, A506:250, 2003.
- [62] Torbjorn Sjostrand, Stephen Mrenna, and Peter Skands. PYTHIA 6.4 Physics and Manual. *JHEP*, 0605:026, 2006.
- [63] G. Corcella. HERWIG 6.5: an event generator for Hadron Emission Reactions With Interfering Gluons (including supersymmetric processes). *JHEP*, 0101:0101, 2001. [arXiv:0011363](https://arxiv.org/abs/0011363).
- [64] T. Gleisberg. Event generation with Sherpa 1.1. *JHEP*, 02:007, 2009. [arXiv:0811.4622](https://arxiv.org/abs/0811.4622).
- [65] R. Engel. Photoproduction within the two component dual parton model. 1. Amplitudes and cross-sections. *Z. Phys.*, C66:203, 1995. [doi:10.1007/BF01496594](https://doi.org/10.1007/BF01496594).
- [66] Fritz W. Bopp, R. Engel, and J. Ranft. Rapidity gaps and the PHOJET Monte Carlo. 1998. [arXiv:9803437](https://arxiv.org/abs/9803437).
- [67] T Sjöstrand, S Mrenna, and P Skands. Brief introduction to pythia 8.1. *Comput. Phys. Comm.*, 178:852, 2008.
- [68] G. Ingelman P. Bruni, A. Edin. POMPYT version 2.6 - A Monte Carlo to Simulate Diffractive Hard Scattering Processes. URL: <http://www3.tsl.uu.se/theppompyp/>.
- [69] J. R. Forshaw B. E. Cox. POMWIG: HERWIG for diffractive interactions. *Comp. Phys. Comm.*, 144:104, 2002. [arXiv:0010303](https://arxiv.org/abs/0010303).
- [70] J.A.M. Vermaseren. Two-photon processes at very high energies. *Nucl. Phys*, B229:347, 1983.
- [71] M. Boonekamp et al. FPMC: a generator for forward physics. [arXiv:1102.2531](https://arxiv.org/abs/1102.2531).
- [72] M. Bahr et al. Herwig++ Physics and Manual. *Eur. Phys. J.*, C58:639–707, 2008. [arXiv:0803.0883](https://arxiv.org/abs/0803.0883), [doi:10.1140/epjc/s10052-008-0798-9](https://doi.org/10.1140/epjc/s10052-008-0798-9).
- [73] F. James. A review of pseudorandom number generators. *Comput. Phys. Comm.*, 60:329, 1990.
- [74] G. P. Lepage. A review of pseudorandom number generators. *J. of Comp. Phys.*, 27:192, 1978.

- [75] E. W. N. Glover W. T. Giele. Higher-order corrections to jet cross sections in e^+e^- annihilation. *Phys. Rev.*, D 46:1980, 1992.
- [76] M. H. Seymour S. Catani. A general algorithm for calculating jet cross sections in NLO QCD. *Nucl. Phys.*, B 485:291, 1997.
- [77] L. Lönnblad. Ariadne version 4 — A program for simulation of QDC cascades implementing the colour dipole model. *Com. Phys. Comm.*, 71:15–31, 1992.
- [78] R.P. Feynman R.D. Field. A parametrization of the properties of quark jets. *Nucl. Phys.*, B 136:1, 1978.
- [79] G. D. Lafferty I. G. Knowles. Hadronization in Z^0 decay. *J. Phys.*, G 23:731–791, 1997.
- [80] G. Veneziano D. Amati. Preconfinement as a property of perturbative QCD. *Phys. Lett.*, B 83:87, 1979.
- [81] S. Gieseke et al. Herwig++ 1.0: An Event Generator for e^+e^- Annihilation. *JHEP*, 0402:005, 2004. [arXiv:0311208v2](https://arxiv.org/abs/0311208v2).
- [82] B.R. Webber. A QCD model for jet fragmentation including soft gluon interference. *Nucl. Phys.*, B 238:492, 1984.
- [83] A. Kupco. Cluster hadronization in HERWIG 5.9, 1999. [arXiv:9906412](https://arxiv.org/abs/9906412).
- [84] S. Gieseke et al. Herwig++ 2.5 Release Note. 2011. [arXiv:1102.1672](https://arxiv.org/abs/1102.1672).
- [85] The ATLAS Collaboration. Charged-particle multiplicities in pp interactions at $\sqrt{s} = 900$ GeV measured with the ATLAS detector at the LHC. *Phys. Lett.*, B688:21–42, 2010. [arXiv:1003.3124](https://arxiv.org/abs/1003.3124).
- [86] M. Bahr et al. The Underlying Event and the Total Cross Section from Tevatron to the LHC. *JHEP*, 01:065, 2009. [arXiv:0806.2949](https://arxiv.org/abs/0806.2949).
- [87] M. H. Seymour J. M. Butterworth, J. R. Forshaw. Multi-Parton Interactions in Photoproduction at HERA. *Z. Phys.*, C72:637–646, 1996. [arXiv:9601371](https://arxiv.org/abs/9601371).
- [88] P. Bruni and G. Ingelman. Diffractive W and Z production at p anti-p colliders and the pomeron parton content. *Phys. Lett.*, B311:317–323, 1993. [doi:10.1016/0370-2693\(93\)90576-4](https://doi.org/10.1016/0370-2693(93)90576-4).
- [89] Gerhard A. Schuler and Torbjorn Sjostrand. Hadronic diffractive cross-sections and the rise of the total cross-section. *Phys. Rev.*, D49:2257–2267, 1994. [doi:10.1103/PhysRevD.49.2257](https://doi.org/10.1103/PhysRevD.49.2257).

- [90] Edmond L. Berger, John C. Collins, Davison E. Soper, and George F. Sterman. Diffractive Hard Scattering. *Nucl. Phys.*, B286:704, 1987. doi:10.1016/0550-3213(87)90460-3.
- [91] K. H. Streng. Hard QCD scatterings in diffractive reactions at HERA. CERN-TH-4949.
- [92] A. Donnachie and P. V. Landshoff. Elastic Scattering and Diffraction Dissociation. *Nucl. Phys.*, B244:322, 1984. doi:10.1016/0550-3213(84)90315-8.
- [93] A. Capella, U. Sukhatme, C-I Tan, and J. Tran Thanh Van. Dual parton model. *Phys. Rept.*, 236:225, 1994. doi:10.1016/0370-1573(94)90064-7.
- [94] V. A. Abramovsky, V. N. Gribov, and O. V. Kancheli. Character of inclusive spectra and fluctuations produced in inelastic processes by multi - pomeron exchange. *Yad. Fiz.*, 18:595–616, 1973.
- [95] A. Capella, A. Kaidalov, C. Merino, and J. Tran Thanh Van. Diffractive dissociation in deep inelastic scattering at HERA. *Phys. Lett.*, B343:403–409, 1995. arXiv:9407372, doi:10.1016/0370-2693(94)01430-K.
- [96] A. Capella, A. Kaidalov, C. Merino, D. Pertermann, and J. Tran Thanh Van. Hard diffraction at HERA and the gluonic content of the pomeron. *Phys. Rev.*, D53:2309–2316, 1996. arXiv:9506454, doi:10.1103/PhysRevD.53.2309.
- [97] The ATLAS Collaboration. Letter of Intent for the Phase-I Upgrade of the ATLAS Experiment, 2011. URL: <https://cdsweb.cern.ch/record/1402470/>.
- [98] L. Lönnblad. ThePEG, Pythia7, Herwig++ and Ariadne. *Nucl. Instr. Meth.*, A559:246, 2006.
- [99] C. F. v. Weizsäcker. Ausstrahlung bei Stößen sehr schneller Elektronen. *Z. Phys.*, 88:612–625, 1934.
- [100] E. J. Williams. *Kgl. Danske Vidensk. Selskab. Mat.-Fiz. Medd.*, 13:N4, 1935.
- [101] O. Kepka. *QCD and Diffraction in the ATLAS*. PhD thesis, Charles University in Prague, 2009. URL: <http://cdsweb.cern.ch/record/1255854/files/CERN-THESIS-2010-045.pdf>.
- [102] A. Aktas et al. Measurement and QCD analysis of the diffractive deep-inelastic scattering cross-section at HERA. *Eur.Phys.J.*, C48:715–748, 2006. arXiv:0606004.
- [103] *The Les Houches accord PDFs (LHAPDF) and LHAGLUE.*, 2005. arXiv:9407372.
- [104] P. Nason. A New Method for Combining NLO QCD with Shower Monte Carlo Algorithms. *JHEP*, 0411:040, 2004. arXiv:0409146v1, doi:10.1088/1126-6708/2004/11/040.

- [105] J. Forshaw. Central Exclusive Production at the LHC, 2009. [arXiv:0901.3040](#).
- [106] J. Forshaw T. Coughlin. Probing the theoretical description of central exclusive production. *PoS, DIS 2010:064*, 2010. [arXiv:1006.4494](#).
- [107] J. Monk. *A Study of Central Exclusive Production*. PhD thesis, University of Manchester, 2006. URL: <http://www.hep.man.ac.uk/u/forshaw/monk.pdf>.
- [108] M. H. Seymour. The higgs boson lineshape and perturbative unitarity. *Phys. Lett.*, B345:409–414, 1995. [arXiv:9505211](#).
- [109] J. F. Gunion et. all. *The Higgs Hunter's Guide*. Perseus Publishing, 2000.
- [110] Z. Bern et all. QCD and QED corrections to light-by-light scattering. *JHEP*, 11:031, 2001. [arXiv:0109079](#).
- [111] J Bjorken, S Brodsky, and Hung Jung Lu. Rapidity gap events in e^+e^- annihilation. *Phys. Lett.*, B286:153, 1992. [doi:10.1016/0370-2693\(92\)90173-2](#).
- [112] W Lampl et al. Calorimeter Clustering Algorithms: Description and Performance. (ATL-LARG-PUB-2008-002. ATL-COM-LARG-2008-003), Apr 2008.
- [113] O Kepka, A Kupco, and P Ruzicka. Rapidity gap distributions in pp interactions at $\sqrt{s} = 7$ TeV measured using calorimeter. Technical Report ATL-COM-PHYS-2011-143, CERN, Geneva, Feb 2011.
- [114] The ATLAS Collaboration. The Expected Performance of the ATLAS Inner Detector. Technical Report ATL-PHYS-PUB-2009-002, CERN, Geneva, 2008.
- [115] O et all Kepka. Rapidity Gap Cross Sections in pp Interactions at $\sqrt{s}=7$ TeV. Technical Report ATL-COM-PHYS-2011-965, CERN, Geneva, Jul 2011.
- [116] et all. Kepka, O. Rapidity Gaps Conf Note – additional supporting material. Technical Report ATL-COM-PHYS-2011-342, CERN, Geneva, March 2011.
- [117] The ATLAS Collaboration. Rapidity gap cross sections in pp interactions at $\sqrt{s} = 7$ tev, 2011.
- [118] W. Bell et al. Offline performance of the atlas minimum bias trigger scintillator detector at $\sqrt{s} = 7$ tev. Technical Report ATL-COM-LUM-2010-033, CERN, Geneva, Nov 2010.
- [119] R. Barlow and C. Beeston. Fits MC fractions to data histogram. *Comp. Phys. Comm.*, 77:219–228, 1993.

- [120] The ATLAS Collaboration. Measurement of the $W \rightarrow l\nu$ and $Z/\gamma^* \rightarrow ll$ production cross sections in proton-proton collisions at $\sqrt{s} = 7$ TeV with the ATLAS detector. *JHEP*, 1012:160, 2010. [arXiv:1010.2130](#).
- [121] F Colecchia, E Nurse, R Prabhu, and P Wijeratne. Validation of the calorimeter energy response from $\pi^0 \rightarrow \gamma\gamma$ candidates. Technical Report ATL-COM-CAL-2011-003, CERN, Geneva, Aug 2011.
- [122] The CMS Collaboration. Observation of diffraction in proton-proton collisions at 900 and 2360 GeV centre-of-mass energies at the LHC, 2010. URL: <https://cdsweb.cern.ch/record/1271073/>.
- [123] The CMS Collaboration. Observation of diffraction in proton-proton collisions at 7 TeV centre-of-mass energies at the LHC, 2011.
- [124] The ATLAS Collaboration. Rapidity Gap Cross Sections Measured with the ATLAS Detector in pp Collisions at $\sqrt{s} = 7$ TeV. *Eur. Phys. J., C* 72:1926, 2012. [arXiv:1201.2808](#).
- [125] S van der Meer. Calibration of the effective beam height in the ISR. Technical Report CERN-ISR-PO-68-31. ISR-PO-68-31, CERN, Geneva, 1968.
- [126] G. D'Agostini. A Multidimensional unfolding method based on Bayes' theorem. *Nucl. Instr. Meth.*, A362:487–498, 1995. [doi:10.1016/0168-9002\(95\)00274-X](#).
- [127] Andreas Hocker and Vakhtang Kartvelishvili. SVD Approach to Data Unfolding. *Nucl. Instrum. Meth.*, A372:469–481, 1996. [arXiv:9509307](#), [doi:10.1016/0168-9002\(95\)01478-0](#).
- [128] T. Auye. Unfolding algorithms and tests using RooUnfold, 2011. [arXiv:1105.1160](#).
- [129] The ATLAS Collaboration. Track Reconstruction Efficiency in $\sqrt{s} = 7$ TeV Data for Tracks with $p_T > 100$ MeV. Technical Report ATL-PHYS-INT-2011-001, CERN, Geneva, Jan 2011.
- [130] D. Acosta et al. Inclusive double-pomeron exchange at the fermilab tevatron $p\bar{p}$ collider. *Phys. Rev. Lett.*, 93(14):141601, Sep 2004. [doi:10.1103/PhysRevLett.93.141601](#).
- [131] T. Affolder et al. Double diffraction dissociation at the Fermilab Tevatron collider. *Phys. Rev. Lett.*, 87:141802, 2001. [arXiv:0107070](#), [doi:10.1103/PhysRevLett.87.141802](#).
- [132] S. Gieseke, C.A. Rohr, and A. Siodmok. Multiple Partonic Interaction Developments in Herwig++. 2011. [arXiv:1110.2675](#).

- [133] V.A. Khoze M. G. Ryskin, A.D. Martin. Proton opacity in the light of LHC diffractive data. *Eur. Phys. J.*, C72:1937, 2012. [arXiv:1201.6298](#), [doi:10.1140/epjc/s10052-012-1937-x](#).
- [134] A. D. Martinl et al. Diffractive Physics, 2012. [arXiv:1206.2124](#).
- [135] U. Maor E. Gotsman, E. Levin. Soft interaction model and the LHC data, 2012. [arXiv:1203.2419](#).